Surface characterization of indium compounds as functional layers for (opto)electronic and sensoric applications

Dissertation

zur Erlangung des akademischen Grades
doctor rerum naturalium (Dr. rer. nat.)

vorgelegt dem Rat der
Fakultät für Mathematik und Naturwissenschaften
der Technischen Universität Ilmenau

von Dipl.-Ing.
Marcel Himmerlich
aus Waltershausen

Gutachter:
Priv.-Doz. Dr. S. Krischok, Institut für Physik, Technische Universität Ilmenau
Prof. Dr. O. Ambacher, Fraunhofer-Institut für Angewandte Festkörperphysik, Freiburg
Prof. Dr. T. A. Klar, Institut für Physik, Technische Universität Ilmenau

Tag der Einreichung: 26.06.2008
Tag der öffentlichen Aussprache: 05.11.2008

urn:nbn:de:gbv:ilm1-2008000246

Contents

1 Introduction and motivation **1**

2 Experimental: setup, methods and physical principles **3**
2.1 Thin film growth . . . 3
2.2 Reflection high-energy electron diffraction (RHEED) . . . 5
2.3 Photoelectron spectroscopy (PES) . . . 7
2.3.1 Theory of photoelectron emission . . . 9
2.3.2 X-ray photoelectron spectroscopy (XPS) . . . 11
2.3.3 Ultra-violet photoelectron spectroscopy (UPS) . . . 11
2.3.4 Secondary electron emission (SEE) . . . 12
2.4 Electron energy loss spectroscopy (EELS) . . . 13
2.5 Excitation sources and electron detection . . . 14
2.5.1 X-ray source for XPS . . . 14
2.5.2 HIS13 VUV light source for UPS . . . 15
2.5.3 EKF 1000 electron source for EELS . . . 16
2.5.4 Hemispherical electron analyzer . . . 17
2.6 Atomic force microscopy (AFM) . . . 18
2.7 Growth and surface analysis system . . . 21
2.7.1 MBE growth and surface preparation chamber . . . 21
2.7.2 Surface analysis chamber . . . 22
2.7.3 Load lock chamber . . . 23
2.7.4 Experimental details and specifications of the electron spectroscopy measurements . . . 24

3 Chemical and electronic properties of InN(0001) surfaces **25**
3.1 InN - a promising narrow band gap material . . . 25
3.2 Electron accumulation at InN surfaces . . . 26
3.3 Examination of InN surfaces which have been exposed to ambient conditions 27
3.4 Influence of In/N flux ratio on the surface properties of InN grown by PAMBE 29
3.5 Bulk properties of InN(0001) samples grown under optimized conditions . . 37
3.5.1 X-ray diffraction (XRD) . . . 37
3.5.2 Spectroscopic ellipsometry (SE) . . . 38
3.5.3 High-resolution electron energy loss spectroscopy (HREELS) . . . 38
3.6 Electronic properties of clean InN(0001) surfaces probed by electron spectroscopy . . . 40

3.6.1 Occupied and unoccupied electronic states 40
3.6.2 InN(0001)-(2×2) and -($\sqrt{3} \times \sqrt{3}$)R30° surface states 44
3.6.3 Interaction of InN(0001) with oxygen 48

4 Surface properties and ozone interaction of indium oxide films grown by MOCVD 51
4.1 Indium oxide - an ozone sensitive material at room temperature 51
4.2 Valence band structure and electronic properties of different In_2O_3 polymorphs 53
4.3 Non-stoichiometry and defect states in In_2O_3 films grown by MOCVD at low temperatures 58
4.4 UV photoreduction and oxidation of LT-InOx sensor surfaces 64

5 Surface composition and electronic properties of indium tin oxide and oxynitride films 73
5.1 Indium tin oxynitride - transparent conductive oxide with improved optical properties 73
5.2 ITO(N) sample preparation and morphology 74
5.3 Analysis of the incorporated nitrogen in ITON 76
5.4 Origin of the thermally induced changes in ITON films 80
5.5 Surface electronic properties of ITON 82

6 Summary and Outlook 87

Bibliography 92

A Abbreviations and Symbols 103

B List of publications 105

List of Figures

2.1 Principle setup of the used MBE chamber 4
2.2 Schematic of the Ewald construction and generation of the RHEED pattern 6
2.3 Surface structure of the uppermost bilayer of wurtzite nitride surfaces with (0001) orientation 7
2.4 Principle of photoelectron emission 8
2.5 Energy dependence of the electron inelastic mean free path for elements . . 10
2.6 Principle components of the monochromated X-ray source 14
2.7 Functional parts of the HIS13 VUV lamp 15
2.8 Functional parts of the EKF 1000 electron source 16
2.9 Principle setup of a concentric hemispherical electron analyzer 17
2.10 Principle of image acquisition in contact mode atomic force microscopy . . 19
2.11 Interatomic force vs. distance curve between tip and sample in atomic force microscopy 20
2.12 Photographs of the growth and surface analysis system 21

3.1 Contact mode AFM scans and line profiles of an InN surface in the stage of island coalescence at low thickness 28
3.2 Surface band bending and bulk Fermi level of nominally undoped and Mg-doped InN 29
3.3 Variation of the RHEED patterns of InN films deposited with different In/N flux ratio during PAMBE growth at 440°C 30
3.4 Dependence of the topography of InN films on the In/N flux ratio during PAMBE growth at 440°C measured by non-contact atomic force microscopy 31
3.5 $In3d_{5/2}$ and N1s core level spectra of *in-situ* prepared InN films 33
3.6 XRD ω-2Θ scans of the InN(0004) reflex comparing InN samples with and without excess nitrogen 34
3.7 Photoemission spectra of the InN valence band and In4d semi-core level measured using monochromated AlKα radiation 35
3.8 Photoemission spectra of the InN valence band and In4d semi-core level measured using He II radiation 36
3.9 Results of the HREELS measurements on InN(0001) and the corresponding variation of the carrier plasmon induced energy loss in dependence on the used primary electron energy 39
3.10 k-dependence of the detected electron states in PES for different analyzer acceptance angles 41

3.11 Schematic of the different energy regions in a He I spectrum of InN that contain information about occupied states below the Fermi level E_F as well as unoccupied states above the vacuum level E_{Vac} 42
3.12 Comparison of the InN density of occupied and unoccupied states between available DFT calculations and the results of photoemission spectroscopy . 43
3.13 RHEED patterns and geometric atom arrangement of InN(0001) surfaces with (2×2) and $(\sqrt{3} \times \sqrt{3})$R30° reconstruction 45
3.14 Valence band photoemission spectra of InN samples with (2×2) and $(\sqrt{3} \times \sqrt{3})$R30° surface reconstruction as well as indium-rich grown InN 46
3.15 Bulk and surface density of states for InN(0001) with an indium-induced $(2{\times}2)$ reconstruction and in In-bilayer configuration calculated using DFT . 47
3.16 Changes in the valence band spectra of InN(0001) upon interaction with O_2 49

4.1 Room temperature ozone detectors based on polycrystalline indium oxide. . 52
4.2 Morphology of the bcc-In_2O_3(001), bcc-In_2O_3(111) and rh-In_2O_3(0001) samples measured using contact mode atomic force microscopy 54
4.3 In3$d_{5/2}$ and O1s core level spectra of bcc-In_2O_3(001), bcc-In_2O_3(111) and rh-In_2O_3(0001) 55
4.4 Valence band photoelectron spectra of bcc-In_2O_3(001), bcc-In_2O_3(111) and rh-In_2O_3(0001) 56
4.5 Model of the band alignment at In_2O_3 surface depending on different band gap energies. 57
4.6 Crystal structure and surface topography of nanocrystalline indium oxide grown by MOCVD at 200°C 58
4.7 Comparison of the In3d and O1s core level spectra between crystalline In_2O_3 grown above 400°C and nanocrystalline LT-InOx deposited at 200°C 59
4.8 Carbon impurities at In_2O_3 surfaces depending on preparation conditions . 60
4.9 Valence band photoelectron spectra of In_2O_3 and LT-InOx films 62
4.10 UV-induced changes of the valence band states of LT-InOx films 63
4.11 Changes of the In3$d_{5/2}$ and O1s photoelectron spectra of LT-InOx films upon UV illumination and ozone oxidation 64
4.12 Changes of the valence states of LT-InOx films upon ozone oxidation and subsequent UV illumination 65
4.13 Temperature dependent desorption of ozone-induced adsorbates from LT-InOx surfaces 66
4.14 Schematic of a possible band distribution at indium oxide nanoparticles after ozone oxidation and UV-induced photoreduction 68
4.15 In4d semi-core level and valence band spectra of LT-InOx films after interaction with O_3, O_2 and H_2O 70

5.1 Influence of rapid thermal annealing on the optical transmittance of ITO and ITON films 74
5.2 Influence of deposition power and annealing temperature on the electron concentration of rf-sputtered ITON samples 75

5.3 Atomic force micrographs of ITO and ITON films deposited by rf-sputtering at 350 W . . . 76
5.4 Amount of incorporated nitrogen in ITON films deposited at 350 W depending on subsequent rapid thermal annealing . . . 77
5.5 N1s core level spectra of ITON films deposited at 350 W prior to and after rapid thermal annealing at 400°C and 600°C . . . 79
5.6 Dependence of the In(MNN), Sn(MNN) and O(KLL) X-ray induced Auger-electron emission as well as the Sn/In intensity ratio depth profile on annealing temperature of ITON thin films . . . 81
5.7 Comparison of the In3$d_{5/2}$ peak shape of a ITON sample prior to and after rapid thermal annealing . . . 83
5.8 Electron energy loss spectra of a ITON film annealed at 600°C . . . 84
5.9 Comparison of the valence band photoemission of ITO and ITON films . . 86

List of Tables

2.1 Photon energy and intensity of the spectral lines generated by a He discharge 16

3.1 Lattice constants of InN epilayer and GaN template as determined from XRD reciprocal space maps 37

4.1 Variation of the work function and the valence band maximum of different indium oxide samples 67

Chapter 1

Introduction and motivation

This thesis is based on investigations performed in different research projects that have been carried out in an interdisciplinary atmosphere comprising of physicists, electrical engineers and material scientists in the Center for Micro- and Nanotechnologies at Technical University Ilmenau during the last three and a half years. The aim and goal of these studies is linked on the one hand to improve material and device properties based on indium compounds for sensoric and (opto)electronic applications and on the other hand to acquire a fundamental knowledge concerning the underlying processes of device operation. Within this context, this dissertation is devoted to the investigation of fundamental surface properties of different indium containing materials as a function of film growth parameters and post-deposition treatments as well as to the study of adsorption and desorption processes of oxidizing gases at these surfaces.

Among the variety of different indium compounds, tin-doped indium oxide, also called indium tin oxide (ITO), is well established in applications where transparent and conductive films are required, e.g. in display devices, solar cells, organic light emitting diodes and touch screens. Nevertheless, the improvement of any type of device property in order to increase the efficiency is an ongoing process. This is also true for ITO thin films. One approach is to incorporate nitrogen into the material (ITON) in order to increase the window of optical transmission as well as to improve the electron transport properties. Other indium containing materials, such as indium nitride (InN) and polycrystalline indium oxide (In_2O_3) films have attracted increased attention in the last years due to their specific material properties that have a promising potential in specific applications enabling better performance of semiconductor devices or even new products. Due to the high electron mobility in InN, ultrafast field effect transistors are proposed to be realized as well as emitters of high intensity terahertz radiation. Since the band gaps of group-III nitrides bridge the optical spectrum from the infrared to the near UV region, many applications in light generating, absorbing or detecting devices are possible or already existing. In this context, InN covers the low energy region, since it has a band gap in the IR region below 0.7 eV. On the other hand, polycrystalline indium oxide films were found to be specifically sensitive to ozone at room temperature. This gives hope to realize cheap and integrated gas sensors that can be used in a wide range of possible applications, even in portable devices.

However, many of the basic properties of InN and In_2O_3 are still being debated, e.g. even the value and the type of the band gap of In_2O_3 is not clarified yet. As a second example,

the origin of the high electron concentration at InN surfaces is a matter of ongoing discussion. Many open questions are in parts related to the surface properties of the materials and their interaction with adsorbates. Therefore, this work focuses on the investigation of the chemical composition as well as the structural and electronic properties of indium compound surfaces and interfaces, their interaction with oxygen containing molecules (O_2, O_3 and H_2O) and, in the case of ITON, on the material changes upon thermal treatment using surface sensitive techniques.
Since for a comprehensive knowledge, the extent of the different material aspects that have to be considered is very large and structural, chemical, electrical, optical and surface properties are strongly linked to each other, it is indispensable to compare the results of surface analysis to the information gained by other characterization methods that have been performed by colleagues working in these joint projects. As a result, a close cooperation and exchange was developed and maintained with Dr. Vadim Lebedev, Chunyu Wang and Dr. Volker Cimalla, all former members of the Nanotechnology group at TU Ilmenau who are now working at the Fraunhofer Institute for Applied Solid-State Physics (IAF) in Freiburg. In particular the supply with InN films grown by molecular beam epitaxy (MBE) and indium oxide films prepared by metalorganic chemical vapor deposition (MOCVD), constitutes a fundamental basis of the performed experiments. The same is valid for the cooperation with Dr. Elias Aperathitis and Maria Koufaki from the Microelectronics Research Group at the Foundation for Research and Technology-HELLAS in Heraklion (Crete), concerning the supply with ITO and ITON thin films produced by magnetron sputtering.
The scientific and technological aspects as well as open questions of the examined indium based materials that have been produced by different deposition techniques are discussed in the following chapters. First, the experimental methods and the used setup are described. This forms the basics for understanding of the subsequently presented results. The investigation of the properties of clean InN(0001) surfaces that have been analyzed in ultra-high vacuum directly after MBE growth for the first time, the properties of nanocrystalline indium oxide layers and their variation under UV irradiation and ozone exposure as well as the surface chemical and electronic properties of ITO(N) thin films are presented and discussed in separate chapters with regard to the different open scientific and technological questions.

Chapter 2

Experimental: setup, methods and physical principles

This chapter describes the details of the used experimental setup and introduces the physical principles of the main experimental methods applied for the studies of the surface properties of the indium nitride, indium oxide and indium-tin-oxide thin films. The physical principles and important experimental aspects of the used methods are described in Sects. 2.1 - 2.6, followed by details about the equipment, important parameters and resolution aspects of the experimental setup in Sect. 2.7.

2.1 Thin film growth

Out of many available techniques for heteroepitaxial growth, molecular beam epitaxy (MBE) and metalorganic vapor phase epitaxy (MOVPE) have emerged as important tools for research and industrial production of epitaxial films. Both techniques allow excellent control over the growth of thin films and multilayered structures resulting in well defined properties of the films and interfaces. For MOVPE growth, typically metalorganic precursors in combination with hydrides are used that react at the surface to form the desired compound material. This is relevant for the indium oxide samples that have been studied in this work (see chapter 4), where trimethylindium ($In(CH_3)_3$) and water were used as reactants in a N_2 atmosphere. Since MOVPE is carried out at atmospheric or reduced pressure, it restricts *in-situ* analysis of growth processes to optical characterization methods, e.g. ellipsometry [1]. Due to the complexity of MOVPE growth, time consuming efforts for the optimization of growth parameters are necessary in order to tailor the properties of In_2O_3. This has been carried out by Chunyu Wang in the joint project "Kostengünstige Indium- und Zinkoxid basierende, integrierbare Detektoren zum Nachweis von Ozon (INOZON)" at TU Ilmenau which aimed the investigation of low-cost, oxide based ozone detectors. After growth, these samples were taken out of the reactor and analyzed by surface sensitive techniques in UHV.
In molecular beam epitaxy the reactants are delivered by beams of atoms or molecules. Hence, ultra high vacuum (UHV) conditions are required to ensure sufficient mean free

paths of the reactants. In group III-nitride growth the metallic component is evaporated from Knudsen-type crucibles. Commonly nitrogen atoms as well as metastable activated molecules are generated with the use of a nitrogen plasma. This type of growth method is named plasma-assisted molecular beam epitaxy (PAMBE) or sometimes plasma-induced molecular beam epitaxy (PIMBE). Due to the lower growth rates and the necessity of UHV, molecular beam epitaxy is not commonly used in industrial production. Nevertheless, the UHV conditions lead to several advantages that make MBE the method of choice for many research studies. In contrast to MOVPE, MBE thin film growth enables the *in-situ* characterization of thin film growth by methods based on electron or ion beams. This provides immediate feedback and improved control of the growth process. Additionally, the application of MBE in UHV allows the implementation of surface sensitive experimental methods to study the properties of thin films without any exposure of the materials to undesired adsorbates.

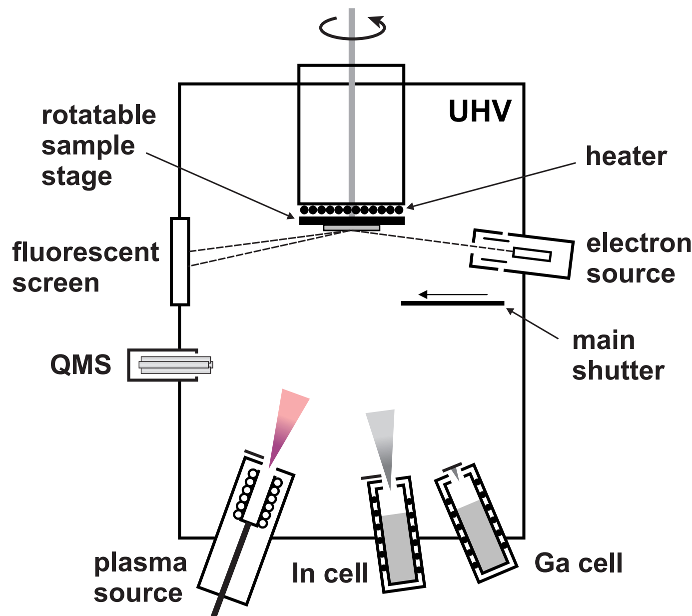

Fig. 2.1: Principle setup of the used MBE chamber.

Consequently, *in-situ* studies of MBE grown nitride surfaces can be employed in the growth and surface analytic system in Ilmenau which consists of two interconnected UHV chambers, one for sample preparation and the other one for surface characterization (see Sect. 2.7 for details). A schematic of the MBE growth and surface preparation chamber is presented in Fig. 2.1. The MBE setup consists of thermal evaporators for the supply of In and Ga and a N_2 plasma source for the supply of activated nitrogen. Additionally, e-beam evaporators for the deposition of thin metal films are also mounted on the system. In-situ growth monitoring is performed using surface characterization by reflection high-energy electron diffraction (RHEED). Specifications of the devices are summarized in Sect. 2.7.1.
For investigating the influence of the growth parameters on the chemical composition and the surface electronic structure, InN thin films were grown on Si-doped GaN templates. Important growth parameters that had to be optimized for adequate film quality are the

substrate temperature during growth as well as the flux of impinging indium atoms at the surface, defined by the temperature of the Knudsen cell [1]. Since the small MBE chamber is equipped with a turbo molecular pump that has a relatively low pumping speed (300 l/s), the growth rate is mainly restricted by the flow of reactive nitrogen, since the plasma discharge breaks down at too high nitrogen pressures. Therefore, the N_2 partial pressure was kept constant at high, but stable pressure conditions and was not regarded as an adjustable parameter for MBE growth.

2.2 Reflection high-energy electron diffraction (RHEED)

Electron diffraction methods, such as low-energy electron diffraction (LEED) and reflection high-energy electron diffraction (RHEED), are powerful techniques to study the periodic arrangement of atoms at surfaces of crystalline materials. Diffraction patterns are formed by constructive interference of single electron scattering effects at periodic surface structures. The principle is based on the scattering of an incoming electron with wavevector $\vec{k}_0$ at the periodic crystal surface structure. For elastic scattering processes, which are typically investigated to study the crystal structure, the following two conditions have to be fulfilled:

$$\left|\vec{k}_0\right| = \left|\vec{k}'\right| \tag{2.1}$$

$$\vec{k}_0 - \vec{k}' = \vec{G}_{hk} \tag{2.2}$$

Here $\vec{k}'$ is the wave vector of the scattered electron and $\vec{G}_{hk}$ is a vector of the reciprocal lattice, which can be understood as Fourier transform of the 2-dimensional surface lattice in real space. An illustrative description of these conditions and the generation of a diffraction pattern is given by the Ewald construction. For elastic processes, the electrons are scattered without loss of energy. The tips of all allowed wavevectors $\vec{k}_i'$ form a spherical surface called the Ewald sphere. Constructive interference of all scattering effects takes place at the intersection points between the Ewald sphere and the reciprocal lattice.
The reciprocal lattice of three-dimensional crystals is made up of single lattice points. For a two dimensional lattice, the crystal periodicity normal to the surface is lacking. Hence, the reciprocal lattice consists of lattice rods, perpendicular to the surface. Constructive interference, resulting in the formation of diffraction spots, occurs where the Ewald sphere is intersected by these lattice rods as illustrated in Fig. 2.2.
For the application of RHEED, an electron beam accelerated to an energy in the range of 5 - 30 keV is incident onto the surface under grazing angle of about 1 - 5°. Electrons in the applied energy range are strongly scattered in solids leading to a limited inelastic mean free path in the range of 100 Å (see Sect. 2.3 for details). Due to the application of grazing incidence, only the uppermost atomic layers, i.e. a few Å, contribute to the diffraction pattern as long as scattering takes place on smooth surfaces [2]. In this geometry, the diffraction pattern can be projected onto a fluorescent screen.

Reflection high-energy electron diffraction is a very powerful analytic tool to monitor MBE thin film growth *in-situ* and in real time [3, 4]. It allows the investigation of the surface of crystals at any stage of preparation and offers the possibility to characterize the surface

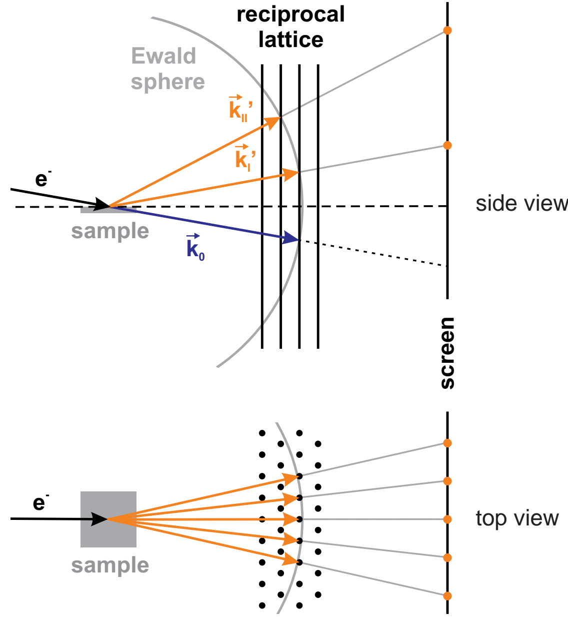

Fig. 2.2: Schematic of the Ewald construction and generation of the RHEED pattern.

qualitatively with respect to crystallinity, morphology, surface reconstructions and lattice parameters. On real surfaces, terraces and atomic steps occur which limit the long-range order of the surface. This non-ideality leads to broadening of the reciprocal rods whose width ΔS is proportional to the inverse length L of the ordered region over which there is coherent scattering. The broadened rods form streaks in the RHEED pattern as they intersect the Ewald sphere. To a first approximation, the width w of the streaks on the RHEED screen is proportional to the width of the rods in reciprocal space as long as the divergence of the incident electron beam can be neglected [3]:

$$w \propto \Delta S = \frac{2\pi}{L} \tag{2.3}$$

If the domain size, i.e. the typical distance between surface steps or other imperfections, is smaller than the natural coherence length of the electron beam (about 1000 Å), the RHEED pattern will be significantly broadened. Therefore, analyzing the width of the streaks provides information about the surface order.

As already indicated above, RHEED is not strictly limited to the uppermost atomic layers. Rough surfaces can exhibit islands which are small enough to be penetrated by the scattered electrons. In this case, diffraction represents the whole three-dimensional periodicity of the crystal, leading to the formation of transmission spots within the streaks in the diffraction pattern [3]. This can be used as an indicator for 3-dimensional growth (island formation) during MBE.

For the evaluation of the lattice constant, the distance d of the streaks on the RHEED screen has to be monitored. To a first approximation, it is proportional to the spacing of the rods in the two-dimensional reciprocal space, i.e. the length of the basic reciprocal in-plane lattice vectors $\vec{G}_{hk}$. As a consequence, changes in the lattice constants during film growth can be measured and the relaxation of incorporated strain during heteroepitaxy due

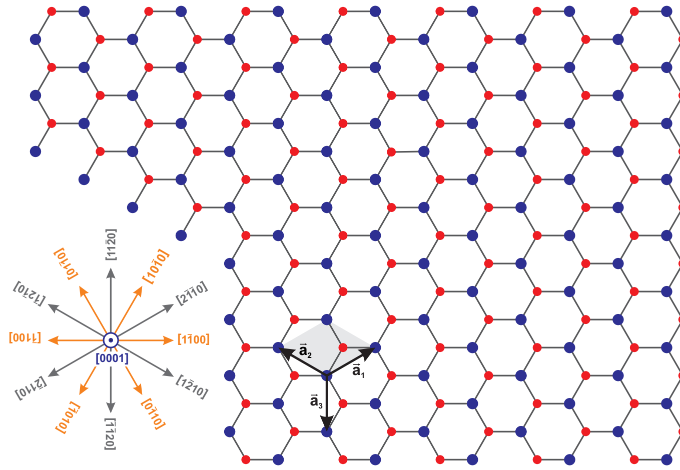

Fig. 2.3: Surface structure of the uppermost bilayer of wurtzite nitride surfaces with (0001) orientation. The surface unit cell, the unit vectors and the highly symmetrical crystal directions are indicated. Blue circles represent the metal atoms in the outermost surface plane, while the red circles represent the nitrogen atoms $\frac{1}{8}$ c underneath.

to different lattice constants of substrate and epilayer can be investigated. Since the reciprocal lattice reflects the periodicity of the lattice in real space, changes in periodicity can easily be observed in RHEED. Periodic rearrangement of surface atoms and the formation of ordered surface reconstructions with different unit mesh lead to the occurrence of new streaks in the RHEED pattern.
In contrast to the geometry of LEED, where the electron diffraction pattern is measured perpendicular to the surface and hence contains information of the whole reciprocal space, the grazing incidence of electrons in RHEED allows only measurements along one crystallographic direction. However, rotation of the samples allows the characterization of all highly symmetrical crystal directions. For nitride surfaces with wurtzite crystal structure, a hexagonal symmetry is found at the surface of a c-plane oriented crystal with two highly symmetrical sixfold directions rotated by 30° with respect to each other. The crystal orientations of hexagonal (0001) nitride surface are shown in Fig. 2.3. For the notation of the two sixfold crystal orientations, the $[11\bar{2}0]$ and $[1\bar{1}00]$ directions are used within this document, which enclose an angle of 90°. Hence, important information about possible surface reconstructions can be obtained by measuring the RHEED patterns along these two crystal directions.

2.3 Photoelectron spectroscopy (PES)

The electronic structure of solids consists of strongly bound core electrons and electrons in the valence band formed due to the periodic atomic potential in a solid crystal. The distribution of the number of electrons in a certain interval of energy is the electron density of states (DOS). A photon can excite an electron to leave a substrate surface if the transferred energy $\hbar\omega$ is large enough to overcome the energetic gap between the binding energy E_{Bin} of the electron and the vacuum energy level E_{Vac} of the material.

This process is visualized in Fig. 2.4. If the absorption of a photon takes place, the resulting photoelectron leaves the surface with a kinetic energy of

$$E_{Kin} = \hbar\omega - \phi - E_{Bin} \tag{2.4}$$

While the electron energy distribution is measured with respect to E_{Vac}, the binding energy scale of a solid is normally referred to the Fermi Energy ($E_{Bin} = 0$ at E_F). Electrons from different electronic states are emitted in all directions when a material is illuminated with a proper light source. The photoelectron current j depends on several experimental parameters [5] such as

- the electron spin $\vec{\sigma}$
- the angles between incoming photon, leaving electron, and surface normal $(\delta, \gamma, \Theta, \Phi)$
- the photon energy and polarization $(\hbar\omega, \vec{e}_p)$
- the binding energy of the electron (E_{Bin})
- the probability of photon-electron interaction (described by the cross section σ)

The notation of the geometric parameters $\delta, \gamma, \Theta, \Phi$ follows the formalism of Briggs and Seah [6] for X-ray Photoelectron Spectroscopy and is schematically shown in Fig. 2.4. The broad spectrum of electrons that can be emitted from materials resulted in a variety of different experimental techniques, all based on the photoelectric effect. If the energy distribution of the outcoming electrons is measured, their spectrum supplies information about the electron energy distribution in the material. For this analysis, special electron energy

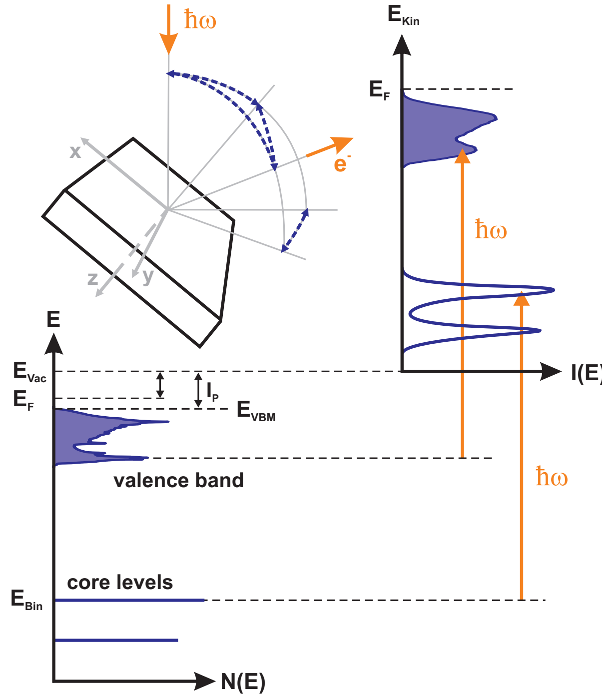

Fig. 2.4: Principle of photoelectron emission [6, 7].

analyzers are used which are based on the deflection of electrons in an electric field. Among the variety of different setups, the most common used are the Cylindrical Mirror Analyzer (CMA) and the Concentric Hemispherical Analyzer (CHA) or also named Spherical Deflection Analyzer (SDA). In this work photoelectron spectra have been measured with analyzers of the hemispherical type. The principle and parts of the electron energy analyzer (EA 125) are described in Sect. 2.5.4.

2.3.1 Theory of photoelectron emission

From an atomic view, photoelectron spectra can be described by an isotropic three-step model [5, 7]. The processes involved in the emission of a photoelectron are typically considered separately in the following sequence:

1. local absorption of a photon combined with excitation of an electron
2. transport of the electron to the surface with the possibility of inelastic scattering
3. escape of the electron through the surface

The measured spectrum consists of a superposition of primary electrons $I_p(E, \hbar\omega)$ which have not suffered an inelastic collision and a background of secondary electrons $I_s(E, \hbar\omega)$ which have lost energy during one or more scattering events.

$$I(E, \hbar\omega) = I_p(E, \hbar\omega) + I_s(E, \hbar\omega) \tag{2.5}$$

According to the three-step model the primary electron distribution is described by

$$I_p(E, \hbar\omega) = P(E, \hbar\omega) \times T(E) \times D(E) \tag{2.6}$$

Proposed models for the transmission function $T(E)$ and the escape function $D(E)$ have been reviewed in [5].

To derive the photoelectron generation rate, which is represented by the function $P(E, \hbar\omega)$, one has to consider all possible combinations that an electron is excited by a photon from its initial occupied state $|i\rangle$ into a final unoccupied electron state $|f\rangle$. Assuming that the crystal momentum $\vec{k}$ is conserved, the absorption process can be described by Fermi's Golden Rule:

$$P(E, \hbar\omega) \propto \sum_{i,f} \int |M_{i,f}|^2 \cdot \delta\Big(E_f(\vec{k}) - E_i(\vec{k}) - \hbar\omega\Big) \times \delta\Big(E_f(\vec{k}) - E\Big)\, d^3k \tag{2.7}$$

Here $M_{i,f} = \langle f|\vec{A} \cdot \vec{p} + \vec{p} \cdot \vec{A}|i\rangle$ is the dipole matrix element, $\vec{A}$ is the electromagnetic vector potential and $\vec{p}$ is the momentum operator of the emitted electron. On the basis of this formula a comparison of the photoelectron spectra with theoretical band structure calculations is possible. For the practical application in an experiment the number of emitted primary electrons can be described in approximation by [8]

$$I_p(\vec{e}_e, E_f, \hbar\omega) \propto \int |M_{i,f}|^2 \cdot D_i(E_i) D_f(E_i + \hbar\omega)\, dE_i \tag{2.8}$$

The vector $\vec{e}_e$ defines the direction of the detected electrons and D_i and D_f are the local density of states (DOS) of the initial and final states. Normally PES measurements are implemented using sources that emit light with a constant photon energy (UV or X-ray) and the emitted photoelectrons are analyzed by the measurement of an "Energy Distribution Curve" (EDC). Measured EDC's are always a convolution of the DOS of the initial and final states which can be described in terms of a "Joint Density of States" (JDOS).

Photoelectron spectroscopy is widely being used for investigation of the surface chemical composition and electronic structure. The high surface sensitivity is caused by the small escape depth of primary electrons that have not lost energy due to scattering effects. The depth of information is dependent on scattering and absorption effects and can be derived from the law of LAMBERT and BEER. When particles or photons propagate through a material their intensity decreases exponentially

$$I(z) = I_0 \cdot exp\left(-\frac{z}{\lambda}\right) \tag{2.9}$$

The value λ is the attenuation length and depends strongly on the material as well as on the interaction process in the material. The average length before an electron is inelastically scattered is named Inelastic Mean Free Path (IMFP) and here denoted by λ_M. Most formulas for the calculation of the energy dependence of $\lambda_M(E)$ are based on generalized empirical data. For elements, inorganic and organic compounds different values were found [9]. The data and the resulting model fit for the energy dependence of λ_M for elements are shown in Fig. 2.5. Nowadays, different predictive formulas are used for the calcula-

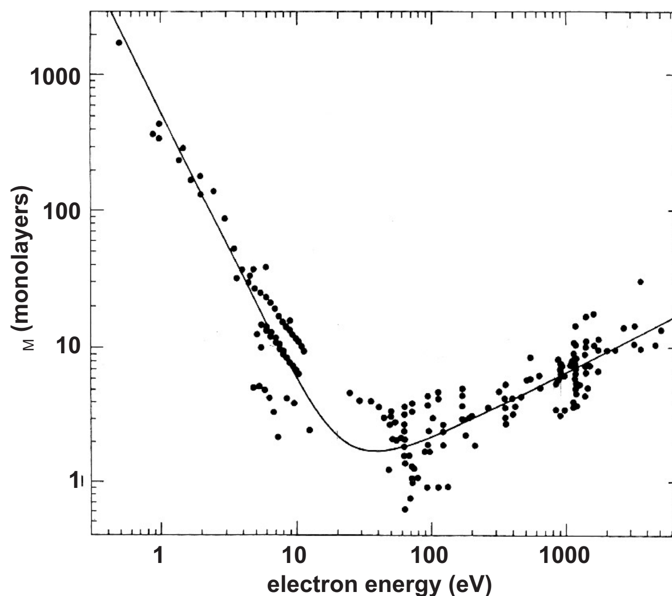

Fig. 2.5: Energy dependence of the electron inelastic mean free path for elements [9].

tion of $\lambda_M(E)$ for compounds [10]. One can generally say that λ_M is in the range of a few nanometers and the minimum of the curve and therefore highest surface sensitivity is achieved when E_{Kin} is in the range of 20 - 50 eV.

2.3.2 X-ray photoelectron spectroscopy (XPS)

Two main PES methods have been developed with the aim to determine the electronic structure of materials. This is historically related to the available laboratory excitation sources. For X-ray photoelectron spectroscopy (XPS), MgKα or AlKα radiation is normally used. With XPS, the chemical composition of a surface can be determined by measuring the emission from core levels. By a careful analysis of the core level binding energy and the emission intensity, information on the chemical environment of the atoms as well as the stoichiometry of the material can be obtained. Therefore, it is also named Electron Spectroscopy for Chemical Analysis (ESCA).
Quantitative analysis is normally based on the comparison of the measured peak area to theoretical predictions of the photoelectron signal. Under the assumption that the reflection of X-rays on the investigated surface or interface is negligible and the X-ray intensity in the investigated material is constant (this is normally the case because the attenuation length of X-rays in matter is much greater than the information depth of PES), the XPS core level intensity of an element i can be described by [6]

$$I_i(\Theta) = J_0 \sec(\delta)\sigma_i(\hbar\omega)L_i(\gamma,\hbar\omega)T(E_i)D(E_i) \cdot \int N_i(z) \times exp\left(-\frac{z}{\lambda_m(E_i)\cos(\Theta)}\right) dz \tag{2.10}$$

where J_0 is the flux of X-rays per unit area onto the sample, $\sigma_i(\hbar\omega)$ is the radiation dependent cross-section which describes the probability for the generation of a photoelectron. $T(E_i)$ is the analyzer transmission function and $D(E_i)$ the detection efficiency for electrons of a certain kinetic energy. The last value is normally assumed to be constant for the measured values of E_{Kin}. Furthermore $L_i(\gamma, \hbar\omega)$ describes the angular dependence of the photoemission from a single atom and relies on the angle between the incoming photons and the emitted electrons as well as the used photon energy [11]. The density of the atom species i is assumed to be only varying in the direction perpendicular to the surface plane and $\lambda_M(E_i)$ is the previously described inelastic mean free path of an electron with the kinetic energy E_i. From this formula models can be derived, for example to determine the stoichiometry of the material or to calculate the thickness d of a thin and uniform overlayer. With the aid of a monochromated X-ray source or synchrotron radiation, it is furthermore possible to analyze the valence band structure of materials.

2.3.3 Ultra-violet photoelectron spectroscopy (UPS)

Ultra-violet photoelectron spectroscopy is employed using photon energies below 100 eV which are not suitable for probing deep core levels. However, the photoelectric cross-sections for valence band electrons are very high in this energy range. Consequently, occupied states of the valence band of semiconductors and insulators as well as of the conduction band of metals can be investigated to analyze, for example, the energy of the valence band maximum with respect to the Fermi level. Under the assumption of a known band gap, the electron affinity χ of a material as well as the conduction band offset of thin films can also be determined.
The interpretation of structures in UPS is far more complicated than in XPS. All elements

exhibit various states in the valence band which are not separated from each other as it is the case for the core states. Furthermore, these states participate strongly in chemical bonding, building up energy bands which result in rather broad features. As a result, support by theoretical calculations of chemical bonds and their respective density of states is in most cases required. For UPS, the photon energy is in a range where resonant transitions into final electron states according to the dipole matrix element $M_{i,f} = \langle i|\vec{A} \cdot \vec{p} + \vec{p} \cdot \vec{A}|f\rangle$ can play an important role in the photoemission process and have to be considered as well.
The break of periodicity at the surfaces leads to energy states different from those in the bulk. These surface states are localized at the surface and decay exponentially both into the bulk and vacuum. As can be seen in Fig. 2.5, the inelastic mean free path for kinetic energies around 50 eV is in the range of single atomic layers leading to a very high surface sensitivity. Therefore, UPS allows the investigation of surfaces with respect to surface states and adsorbates, such as atoms and small molecules. Surface states often reside in the bulk band gap resulting in band bending and Fermi level pinning at the surface [12] and are very sensitive to surface treatment which eases their identification using UPS.

2.3.4 Secondary electron emission (SEE)

For the investigation of occupied states in the valence band as well as chemical analysis using core level photoemission, in many cases, electrons are analyzed that have not suffered any loss of energy due to scattering during their transport to the surface. However any generated photoelectron can be subject of manifold interactions with other electrons or quasiparticles inside the material leading to characteristic losses of energy. An important example is the excitation of plasmons, which results in characteristic structures in XPS spectra at higher binding energies close to the parent line. [7, 5]
Besides these characteristic single scattering effects, many electrons are subject of multiple interactions resulting in a broad and featureless electron background and an intense cascade peak at the low energy end of the photoemission spectrum. Hence, the measured photoemission spectrum is a superposition of the signal coming from the primary photoelectrons and the contribution of all secondary electrons (see Eq. 2.5). The majority of these so called secondary electrons are most commonly accepted to be produced via direct transfer of energy from the primary photoelectron to electrons in bound states or filled valence band states, thereby promoting them to empty conduction states (interband transitions). Other important mechanisms are excitation of phonons, electron-hole pair creation as well as decay processes of excited electrons. This also involves a cascade process in which higher energy secondary electrons produce more secondaries thereby degrading in energy as they migrate to the surface [13]. From the low energy cut-off of this cascade structure one can determine the work function of the material, after having performed calibration measurements on reference samples (e.g. Au or Ag). For that purpose, in some cases it is necessary to apply a negative voltage of a few volts to the sample in order to overcome the work function of the electron analyzer and to avoid disturbing signals from tertiary electrons which are generated by interaction of electrons with the analyzer material.
As already mentioned, the secondary electrons roll down through the states in the conduction band due to inelastic scattering and pile up at the high density of conduction

states. These electrons can also be emitted into the vacuum leading to structures inside the otherwise featureless distribution of the cascade peak. This aspect has been used for studies of empty states of metals as well as oxide surfaces using electron-induced angle-resolved secondary-electron spectroscopy (ARSES) [14, 13]. For photon-induced electron spectroscopy measurements, the processes of secondary electron generation are qualitatively the same, enabling the study of unoccupied states above the vacuum level E_{Vac} using angle-resolved ultra-violet photoemission measurements [15].

2.4 Electron energy loss spectroscopy (EELS)

The measurement of the energy distribution of electrons that have been scattered from or through a material is named electron energy loss spectroscopy (EELS). For the study of surface properties, an electron beam with a primary energy E_0 and a narrow energetic bandwidth ΔE_0 is focused onto a sample and the reflected electrons are analyzed with respect to their spectral distribution. For impinging electrons the same is valid as for photoelectrons, they can be involved in scattering processes resulting in characteristic energy losses. For conventional EELS experiments, electrons with E_0 ranging from 100 eV to a few keV can partly penetrate into the solid. The scattering cross section in this case is proportional to the bulk loss function [16]

$$\Im\left(\frac{1}{\epsilon(\omega)}\right) \tag{2.11}$$

and is therefore directly linked to the dielectric properties $\epsilon(\omega)$ of a material. For conventional EELS, the standard equipment for Auger and photoelectron spectroscopy can be used, such as hemispherical electron analyzer and a standard electron source. With this method, excitation of electrons from occupied states in the valence band to empty states (interband transitions) can be investigated, which give insight into the band structure of a material. Furthermore, the energy of collective excitations of valence electrons (bulk and surface plasmons) can be determined.
Low energy losses of 10^{-3} to 1 eV correspond to the excitation of phonons and vibrational modes of adsorbate molecules and are usually subject of high resolution electron energy loss spectroscopy (HREELS) using slow electrons. In the case of a specular geometry, dipole scattering at the surface has to be regarded, resulting in a cross section proportional to the surface loss function [16]

$$\Im\left(\frac{1}{\epsilon(\omega)+1}\right) \tag{2.12}$$

In addition to the vibrational structure of surfaces, carrier plasmon excitations of semiconductors that have an energy depending on the carrier concentration n, the effective electron mass m^* and the high frequency dielectric constant ϵ_∞ of a material

$$\omega_p^2 = \left(\frac{ne^2}{\epsilon_\infty \epsilon_0 m^*}\right) \tag{2.13}$$

can be studied. By implementation of measurements with varying primary electron energy in combination with sophisticated modeling of the loss function, by solving the Schrödinger-

Poission equation self-consistently, it is possible to derive the carrier density and band profile at semiconductor surfaces and interfaces [17, 18].

2.5 Excitation sources and electron detection

2.5.1 X-ray source for XPS

All presented core level measurements have been performed using a special X-ray source that is combined with a monochromator (XM1000). This system consists of an AlKα X-ray tube with a small spot filament and a quartz Bragg crystal installed in a geometry of a 500 mm diameter Rowland circle. X-rays from the source are reflected by the quartz crystal Bragg mirror and focused onto the sample in a 1:1 projection. The principle components of the monochromator setup are shown in Fig. 2.6. The removal of the Kα_2 line by the

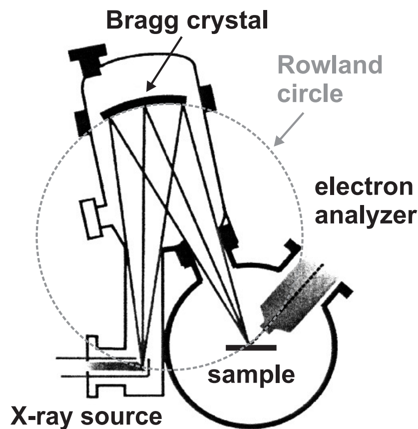

Fig. 2.6: Principle components of the monochromated X-ray source [19].

Bragg monochromator is one important advantage of this type of X-ray source, resulting in a slightly shifted photon energy ($\hbar\omega = 1486.7\,\text{eV}$). As a consequence, the line width of the generated photon is strongly reduced (FWHM $= 0.25\,\text{eV}$) compared to standard X-ray sources (FWHM $= 0.7\,\text{eV}$ for MgKα and $0.85\,\text{eV}$ for AlKα). This effect results in an improved energy resolution, which is important for the detection of small shifts in the core level binding energy. Another benefit from the use of a monochromator is the absence of any disturbing satellite lines (e.g. K$\alpha_{3,4}$). Furthermore, the sample is exposed to less heat radiation and the Bremsstrahlung background is removed, which improves the signal to noise ratio. Additionally, due to the special geometry, fast electrons that are generated inside the X-ray tube have no influence on the spectra. Altogether, these improvements are important and allow the measurement of the valence electrons using X-ray radiation. In that way, the bulk-like valence band density of states can be precisely measured.
Due to the use of a small spot filament, the irradiated sample area is reduced to a size of less than 1 mm in diameter which allows the selective analysis of small samples excluding the appearance of photoelectrons from the surrounding material. The source is typically operated at $U_{HV} = 14\,\text{kV}$ and $I_E = 21\,\text{mA}$.

2.5.2 HIS13 VUV light source for UPS

The UPS UV light source (HIS13) is a water cooled high intensity discharge lamp (see Fig. 2.7) that is directly adapted to the UHV system and allows the windowless illumination of the sample surface. The gas inlet is controlled by a double differential pumping system consisting of a rotary pump on the first stage and a combination of rotary and turbo molecular pump on the second pumping stage. This setup provides the possibility of accurate setting of the gas pressure inside the discharge capillary and restricts the undesirable pressure rise in the UHV chamber. Among the several discharge gases that can be used for generation of UV light (Ar, H_2, He, Kr, Ne, Xe), helium is used in this work to investigate the valence band structure of InN, In_2O_3 and ITO. The operation principle of the HIS13

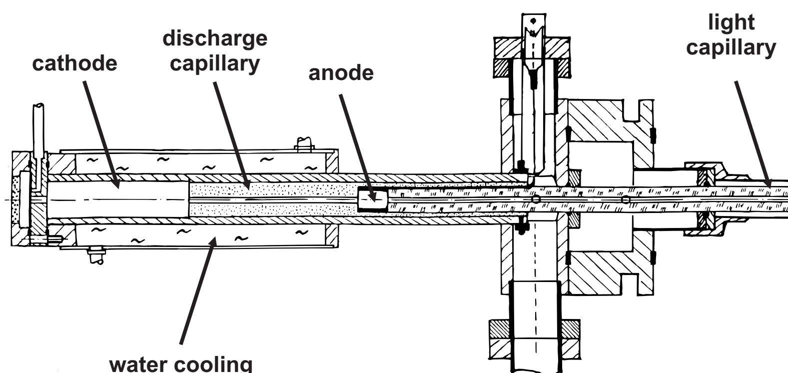

Fig. 2.7: Functional parts of the HIS13 VUV lamp [20].

is based on a cold cathode capillary discharge that can be influenced by adjusting the gas partial pressure as well as the current flow of the discharge. Normally, two modes of light emission are possible:

1. *Light emission from neutral atoms* - He I radiation ($\hbar\omega = 21.22\,\text{eV}$)
   In this case, the VUV light is generated in the positive column of the discharge. The operation mode is normally achieved at higher partial pressures.

2. *Light emission from singly charged ions* - He II radiation ($\hbar\omega = 40.81\,\text{eV}$)
   This radiation type is essentially produced from the cathode fall which is normally located very close to the cathode surface. To achieve this behavior, the discharge must be operated at a very low pressure together with higher discharge currents.

The discharge lamp is operated using a 300 mA power supply with a stability of $< 10^{-4}$. This provides intensity fluctuations of less than 1% if the gas pressure is stabilized. It has to be pointed out that the HIS13 operation parameters can be set to achieve almost pure He I generation which results in the absence of disturbing contributions from He II in the measured spectrum (pressure of $p_{He} \sim 4{\times}10^{-2}$ mbar at first pumping stage and I = 100 mA). However, if the lamp is operated in the second mode, the generation of He I radiation can only by reduced to a certain limit. For the given setup, the achievable intensity ratio $I_{He\,II}\,/\,I_{He\,I}$ is $\sim 10\%$ at $p_{He} = 5{\times}10^{-3}$ mbar and I = 300 mA.
Besides the main lines at 21.22 eV and 40.81 eV, satellite lines are also generated in the gas discharge and have to be taken into consideration for the interpretation of UPS spectra.

For the helium discharge, details of the energies and intensities of the different generated photons are given in Tab. 2.1.

VUV source		$\hbar\omega$ (eV)	rel. intensity (%)	λ (nm)	satellite shift (eV)
He I	α	21.22	100.0	58.43	-
	β	23.09	1.2...1.8	53.70	1.87
	γ	23.74	0.5	52.22	2.52
He II	α	40.81	100.0	30.38	-
	β	48.37	$<$10.0	25.63	7.56
	γ	51.02	n.a.	24.30	10.20

Tab. 2.1: Photon energy and intensity of the spectral lines generated in the VUV discharge lamp HIS13 when operated with helium [20]. The FWHM of the He I and He II main spectral lines is below 10 meV.

For the investigation of the valence electrons in indium compounds, the emission from the shallow In4d semi-core level excited using He II radiation is a very sensitive indicator for changes at the surface. On the other hand, however, this signal interferes with the emission of electrons close to the Fermi edge excited by He I radiation. Additionally, the generated satellite lines of the In4d level disturb the analysis of the valence band distribution of He II spectra. These two factors have to be kept in mind for the analysis of the measurements in the following chapters.

2.5.3 EKF 1000 electron source for EELS

The EKF 1000 is an electron source for the application in AES and EELS experiments. The functional parts of this device are shown in Fig. 2.8. Electrons are generated by a heated LaB_6 filament and are accelerated to an energy of 100 eV to 5 keV by a Wehnelt grid assembly, pass through an electrostatic lens system (condenser lens, aperture and focus lens) that allows to vary the current flow and to set the focal distance of the source in order to adjust the beam diameter at the sample (minimum diameter $< 2\,\mu m$). A deflection system, consisting of quadrupole x/y-deflectors are employed for static and dynamic beam deflection, and can be used in combination with a scanning unit for SAM and SEM imaging. The emission-regulated LaB_6 filament provides reliably and stable emission conditions and

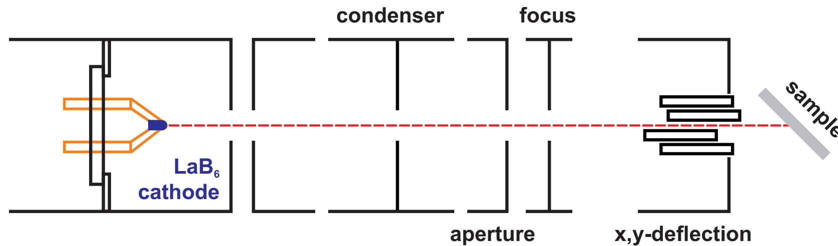

Fig. 2.8: Functional parts of the EKF 1000 electron source.

a high beam current necessary for quantitative analysis of electron spectra (the source is normally operated at an emission current of 40 μA).

2.5.4 Hemispherical electron analyzer

To analyze the distribution I(E) of emitted electrons, a concentric hemispherical analyzer (CHA) is used. A schematic of the setup is shown in Fig. 2.9. It consists of an electrostatic lens system, a hemispherical deflection unit and an electron detection unit. The electrons

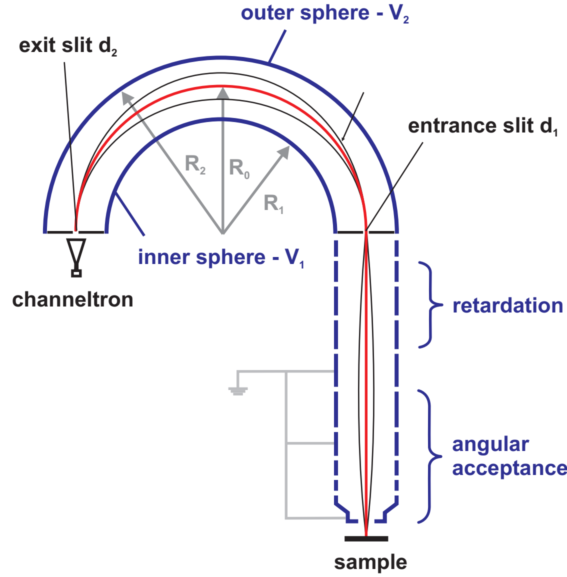

Fig. 2.9: Principle setup of a concentric hemispherical electron analyzer.

emitted from the sample are collected by the lens system and focused onto the entrance aperture of the analyzer. The setting of the first lens defines the analysed area and angular acceptance from where electrons are collected. The second lens retards or accelerates the electrons to match the pass energy of the analyzer. The analyzer itself consists of two hemispherical electrodes with the radii R_1 and R_2 and an applied voltage of V_1 and V_2, respectively. Electrons with an energy E_p that pass the lens system and enter the analyzer tangentially to the median surface at R_0, can only pass the analyzer in a circular orbit, if the electron energy matches the following condition

$$E_p = \frac{e \cdot (V_2 - V_1)}{\frac{R_2}{R_1} - \frac{R_1}{R_2}} \tag{2.14}$$

Due to the finite size d of the analyzer entrance and exit apertures, electrons with a different energy as E_p can pass the analyzer if they have a slightly different entrance angle. Consequently, a bundle of different electron trajectories for electrons with an energy $E_p \pm \Delta E$ are possible. This defines the resulting analyzer energy resolution

$$\Delta E = E_p \cdot (\frac{d}{2R_0} + \alpha^2) \tag{2.15}$$

The parameter α is called angular acceptance of the analyzer and depends on the settings of the electrostatic lens system in front of the sample surface. The electrons that pass the analyzer and leave through the exit aperture are amplified by an electron multiplier (channeltron). The measured current is proportional to the number of electrons if the signal intensity is not such high that saturation effects occur. The used EA125 is a multi-channel analyzer system with 7 channel electron multipliers, placed across the exit plane of the analyzer to improve statistics. The dispersion offset according to this setup is proportional to the used pass energy and is normally calibrated with a reference sample.
The analyzer can be operated in constant pass energy mode (CPE or CAE) with $E_p = const.$ or in constant retardation mode (CRR) where $E_p/E = const.$ The chosen mode defines the analyzer transfer function which is ideally $T(E) \propto 1/E$ for CAE and $T(E) \propto E$ for CRR, respectively.

2.6 Atomic force microscopy (AFM)

The investigation of morphological properties on a nanoscopic scale can be employed using high resolution scanning probe methods. In contrast to scanning tunneling microscopy (STM), where a limitation is given to the investigation of conductive samples, atomic force microscopy (AFM) enables imaging of the surface structure of all kinds of materials, e.g. metals, semiconductors, insulators, biological objects. In addition, measurements in liquid environment are possible. The principle is based on the serial scanning of a sharp tip with a radius of a few ten nm across a sample and the simultaneous measurements of the existing forces between tip and surface. Different variations of atomic probe microscopy have been developed whose application depends on the material that has to be investigated as well as on the physical properties of interest [21, 22].
For a simple analysis of the surface morphology, the most commonly used technique is contact mode AFM. The principle of operation is schematically demonstrated in Fig. 2.10. In this case, the tip is brought into direct contact with the specimen. In order to detect the motion of the tip while scanning across the surface, it is directly connected to a flexible cantilever which serves as signal transducer. Bending and torsion of the cantilever due to morphological changes is related to height differences at the surface and friction forces between tip and surface during scanning, respectively. Typically, bending and torsion are detected by measuring the deflection of a laser beam focused onto the reflective cantilever backside. The deflection is analyzed with a 4-quadrant photodiode acting as position sensitive device (PSD). The continuous movement across the surface is almost always achieved by a piezoelectric actuator. In this well-established configuration, the specimen is mounted onto a tubular piezo scanner that is constantly moving inside a defined area in the x-y-plane. Optimal sensitivity of the PSD is achieved if the laser beam is kept constant in the center of the photodiode. Therefore, the piezo scanner extension (in z-direction) is coupled via a feedback mechanism to the signal from the PSD. When the cantilever is bent, the beam drifts out of the center of the photodiode resulting in different photocurrents for all four quadrants. The signal generated in the photodiode is proportional to the normal force F_N and lateral friction force F_L applied to the tip. The F_N signal can be calibrated

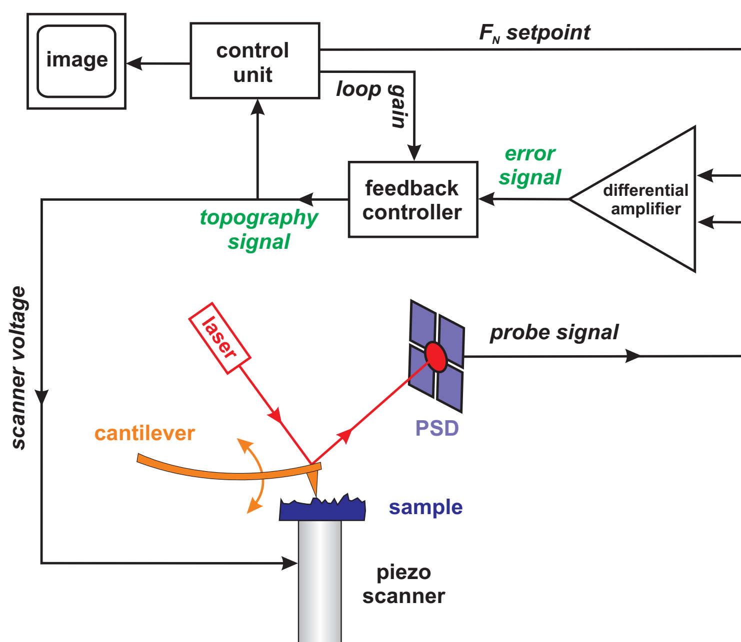

Fig. 2.10: Principle of image acquisition in contact mode atomic force microscopy.

by measuring a force-distance curve under the assumption that the spring constant of the cantilever is known. The probe signal generated during scanning is compared to the set-point F_N^0 value and an error signal is generated. This error signal is sent to the feedback controller which controls the voltage for the z actuation of the piezo scanner causing it to retract or extend. The sample is moved towards or away from the tip and the setpoint value for F_N is maintained. In that way the surface topography can be measured with a resolution of a few nm in lateral direction, depending on the tip radius, and sub-angstrom vertical resolution. A crucial parameter is the loop gain setpoint on the feedback controller. It determines how fast the system reacts to abrupt changes in morphology. Higher loop gain values lead to a better sensitivity on changes in cantilever deflection, but the loop gain is limited to values below the point where the feedback signal starts to excite the system and causing it to oscillate. The real topographic signal is the sum of scanner expansion and cantilever deflection. For a better visualization of abrupt changes in morphology, such as surface steps or facets on islands, it is better to plot the normal force (F_N) signal. It has to be kept in mind, however, that these images do not reflect the real topography of the surface.

Atomic force microscopy in contact mode was used to characterize the surface morphology and crystallite structure of externally grown InN, In_2O_3 and ITO(N) films, that had been exposed to ambient air. Unfortunately, for as-deposited InN films, that have been directly prepared and analyzed in the UHV analytic system, this technique could not be employed. Due to strong attractive forces between tip and freshly grown InN samples, a continuous scanning across the surface in direct contact leads to irregularly appearing stick and slip effects resulting in a severe deterioration of scan quality. In that case it was indispensable to measure the topography in non-contact mode AFM. The typical van-der-Waals curve showing the interatomic force in dependence on tip-sample distance is shown in Fig. 2.11.

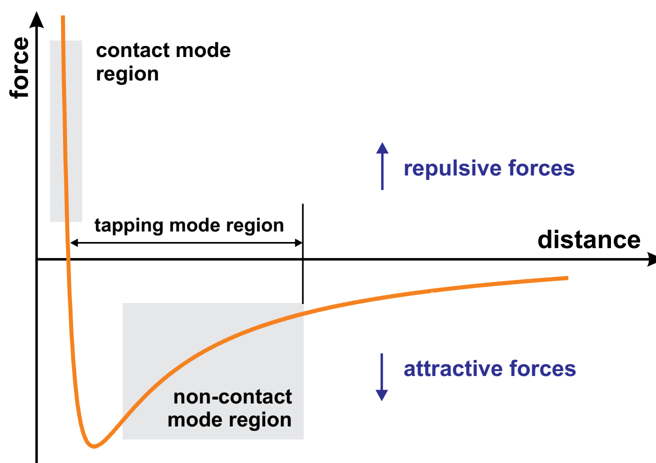

Fig. 2.11: Interatomic force vs. distance curve between tip and sample in atomic force microscopy. Contact mode uses repulsive forces, while in non-contact mode the cantilever oscillates in the attractive force region. (after OURA et al. [2])

At relatively large distances the tip is weakly attracted by the sample due to van-der-Waals forces. With decreasing distance the attraction increases until repulsion occurs. This corresponds to electrostatic forces as the electron clouds of the sample and tip atoms overlap and repel each other. While in contact mode the repulsive forces lead to a bending of the cantilever, non-contact AFM is established by setting a stiff cantilever into vibration close to its resonance frequency (typically 100 to 400 kHz) at an amplitude of a few tens of angstroms while scanning above the surface at a distance of the order of tens to hundreds of angstroms. During scanning in x-y direction as the tip comes closer to the surface, the force gradient, which is the derivative of the force versus distance, changes with tip-to-sample separation, resulting in slight deviations of the cantilever resonance frequency. In non-contact AFM, the variation of the cantilever resonance frequency Δf is used as probe signal which is again compared to a setpoint value Δf^0 by a feedback controller. This signal is used to move the piezo scanner up and down in the z-direction in order to keep the spacing between tip and sample constant and, in this manner, obtain information about the surface topography. The small force values in the non-contact regime and the greater stiffness of the cantilevers used for non-contact AFM are factors that make the signal small, and therefore difficult to measure. Nevertheless, the sensitivity of this detection scheme provides sub-angstrom vertical resolution in the image, as with contact AFM.

2.7 Growth and surface analysis system

The experiments described in this work were carried out in a multi-technique ultra high vacuum (UHV) system located in the Center for Micro- and Nanotechnologies at the Technical University Ilmenau. The complete system is a custom-made apparatus from Omicron NanoTechnology GmbH, Taunusstein. It consists of two interconnected UHV chambers: a) the *surface analytic chamber* and b) the *preparation and MBE growth chamber*, both with base pressures below 2×10^{-10} mbar, and a small sample introduction (load lock) chamber. The vacuum conditions are realized by a combination of turbo molecular and rotary pumps as well as by ion getter and a titanium sublimation pump (TSP) on each of the two main chambers. Photographs of the UHV system are shown in Fig. 2.12.

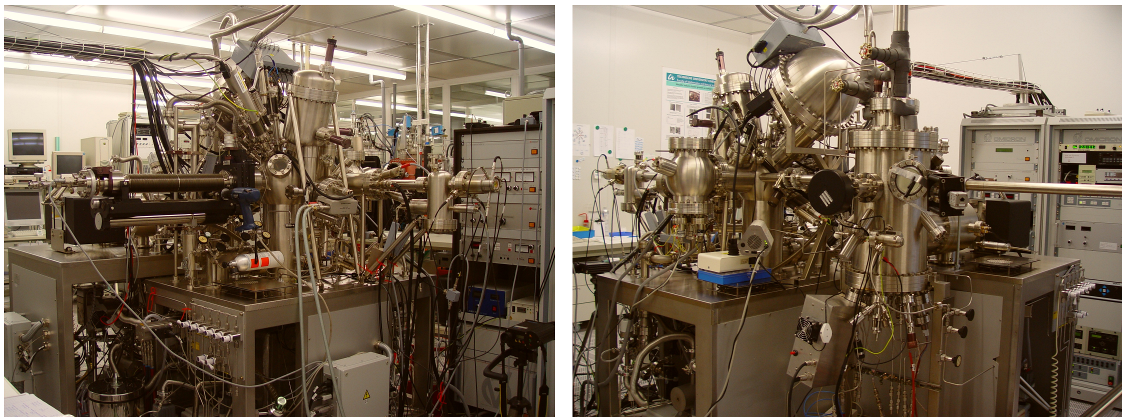

Fig. 2.12: Photographs of the growth and surface analysis system (left: surface analysis chamber, right: preparation and MBE growth chamber).

2.7.1 MBE growth and surface preparation chamber

The preparation and MBE growth chamber is a system designed for surface preparation and thin film growth. For the deposition of various materials it is equipped with electron beam evaporators (EFM 3), e.g. used for the evaporation of gold and silver, and two effusion cells (WEZ 40) with pyrolytic boron nitride (PBN) crucibles and Ta filaments. These Knudsen cells are filled with indium and gallium, respectively, for InN and GaN growth. The active nitrogen is supplied by a SVT Associates RF 4.5 plasma source which can be operated up to 500 W. The different stages of nitride thin film growth as well as surface reconstructions can be monitored by reflection high-energy electron diffraction (RHEED) using an EK-20-RS electron source from Staib Instruments. This electron gun produces an electron beam with kinetic energies up to 20 keV. The electron beam has an adjustable grazing angle of incidence (1 - 5°) and can be focused onto the surface with a spot size of less than 100 μm. The diffraction pattern is visualized with a phosphorus screen and digitalized using a CCD camera (PCO pixelfly).
The sample stage consists of a rotatable manipulator stage with the capability of radiative heating of the sample backside up to temperatures of 1200°C. The sample temperature can

be referenced by a thermocouple mounted on the manipulator sample stage after careful temperature calibration with a pyrometer. A quadrupole mass spectrometer (QMS) with Faraday cup and electron multiplier provides the possibility of residual gas analysis (RGA) in the MBE chamber during sample preparation in a scan range from 1 to 200 atomic mass units.

For surface cleaning and preparation the chamber is further equipped with a cold cathode sputter gun (ISE 5) for Ar^+ ion bombardment. It is mounted at an angle of $\sim 45°$ with respect to the surface normal and can be operated in an energy range from 250 eV to 5 keV allowing a wide range of sputtering conditions.

In order to further reduce contamination effects due to desorption of species from the reactor walls during growth at higher temperatures, the chamber has a cryo-shield for liquid nitrogen cooling which was always operated during thin film growth in this work. In that way the base pressure of the growth chamber could be further reduced by one order of magnitude.

2.7.2 Surface analysis chamber

The chamber is designed to combine the advantages of electron spectroscopy methods such as X-ray photoelectron spectroscopy (XPS), ultra-violet photoelectron spectroscopy (UPS), Auger-electron spectroscopy (AES) and electron energy loss spectroscopy (EELS) with the possibility of investigating the morphology and the structural characteristics of sample surfaces by atomic force microscopy (AFM), scanning tunneling microscopy (STM), photoelectron emission microscopy (PEEM) and scanning electron microscopy (SEM). As a result, the chemical composition, electronic properties and morphology of surfaces can be probed without removing the sample from UHV. For sample transfer and angle-resolved electron spectroscopy measurements the analytic chamber is equipped with a precision manipulator that allows sample positioning in all three directions and rotations along the analyzer plane in order to vary the emission angle in electron spectroscopy. The sample stage on the analytic chamber manipulator enables specimen annealing via radiative heating from the backside (up to ~ 700 K) or cooling down to ~ 120 K via liquid nitrogen (LN_2) cooling.

The different electron spectroscopy techniques are facilitated by several excitation sources mounted on the system. For AES and EELS measurements, the surface can be irradiated by electrons from an EKF 1000 electron gun which uses a LaB_6 cathode and provides electrons of variable energy between 100 eV and 5 keV. The electron beam can further be focused to a spot size down to $< 2\,\mu m$ and scanned across the sample surface in order to perform SEM by secondary electron detection. XPS measurements can be performed using two different X-ray sources. The first is a twin anode X-ray tube (DAR 400) that allows the generation of either MgKα ($\hbar\omega = 1253.6$ eV) or AlKα ($\hbar\omega = 1486.6$ eV) radiation. For obtaining a better energy resolution in the XPS measurements, monochromated X-rays can be generated by a system consisting of a X-ray source (Phi 10-610E) combined with a quartz crystal monochromator (XM 1000). To investigate the valence electrons by means of UPS, a UV light source (HIS 13) is also mounted onto the chamber. The energy distribution of the emitted electrons are detected by a hemispherical electron analyzer (EA 125) with an electron mean path radius of 125 mm. The slit size at the entrance and exit of the analyzer

can be varied by external rotary feedthroughs. Electrons are detected by seven electron multipliers (channeltrons) placed across the exit plane of the analyzer. In case of necessary electron spectroscopy measurements on insulating samples, possible charging effects can be adequately compensated using a charge neutralizer (CN 10).
The scanning probe microscopy (SPM) unit is a combined UHV – AFM/STM system which works at room temperature. For high resolution measurements, vibration decoupling is provided by the AFM/STM base plate being suspended by four soft springs. The resonance frequency of the spring suspension is about 1 Hz. Vibrations of the system are prevented by an arrangement of permanent magnets which float the whole SPM base plate. For AFM the light beam produced by a special bakeable infrared LED ($\lambda = 820$ nm) is reflected from the cantilever backside onto the 4-section position sensitive detector (PSD) via two mirrors which are magnetically mounted to piezo-driven actuators for beam alignment. The scanner unit itself consists of a tube piezo crystal with a maximum scan area of $5 \times 5\,\mu m$ and a maximum extension of $\sim 1\,\mu m$. Measurements can be performed in contact and non-contact AFM mode as well as in STM mode with the further capability of performing scanning tunneling spectroscopy (STS).
In addition to these conventional surface analysis techniques, a Focus IS-PEEM with μ-ESCA electron energy analyzer is attached to the analytic chamber. It enables measurements of the spatial distribution of emitted photoelectrons that are excited either by a mercury lamp (HBO 103W/2) or a deuterium lamp (Heraeus D200F) with a specified step-edge resolution of 20 nm. This system further allows ultra-violet photoelectron microspectroscopy measurements in the micrometer range using a second VUV HIS 13 light source directly connected to the PEEM. More details, information and properties of the PEEM setup can be found in a previous work [23].

2.7.3 Load lock chamber

The load lock is equipped with a turbo pump (Varian) in combination with a rotary pump (Pfeiffer) to achieve a minimum pressure of $\sim 5\times10^{-8}$ mbar. It facilitates the simultaneous loading of two samples. A removable transport box is mounted onto the load lock for transportation of samples to other systems without exposing them to ambient conditions, e.g. for electrical characterization of oxygen sensitive films in a glove box. This transport system has also been successfully used to transfer freshly grown nitride samples to a high resolution electron energy loss spectroscopy (HREELS) system for further characterization of the vibrational signatures and the electronic properties of the surfaces. It allows the transfer of samples without exceeding of the pressure above 1×10^{-5} mbar for ~ 1 hour.
For the deposition of organic molecules such as pentacene or C_{60}, the load lock chamber can be further equipped with a self-made crucible evaporator to avoid any contamination related to evaporation of carbon-based species in the main MBE chamber. The load lock system is additionally connected to the gas inlet system in order to perform clean adsorption experiments at higher pressures than possible in the UHV system. Reactive gases with up to 1 bar pressure can be offered to realize higher doses. After exposure, the system can quickly pumped down and the sample can be transferred and analyzed without being exposed to air.

2.7.4 Experimental details and specifications of the electron spectroscopy measurements

This section summarizes the used experimental settings and parameters for the performed electron spectroscopy studies. Most important aspects are *i)* a correct energy calibration of the system in order to exactly determine important material parameters, like electron binding energy, distance between valence band maximum (VBM) and Fermi level as well as the work function, and *ii)* determination of the energy resolution of the measurements. The calibration of the electron analyzer is regularly performed by measurement of the $Ag3d_{5/2}$ core level emission and an exact determination of the position of the Fermi edge of a polycrystalline silver reference sample that has been prepared by Ar^+ ion bombardment prior to analysis.
The experimental energy resolution is dependent on the initial line width of the excitation source as well as the settings of the analyzer (pass energy, slit size). For XPS measurements, the experimental conditions are chosen to have a FWHM of the $Ag3d_{5/2}$ peak that is below 600 meV ($E_p = 15$ eV). Due to the higher photon flux of the HIS13, smaller slits and a lower pass energy are necessary to obtain optimized signal intensity. This aspect, as well as the fact that the initial line width of He I and He II radiation is narrower, results in much better resolution of the UPS measurements. The exact analysis of the width of the Fermi edge as indicator for resolution is described in [23]. For all presented UPS measurements, the energy resolution is < 100 meV and < 150 meV for the He I and He II spectra, respectively. The line width of the electron beam generated by the EKF source depends on the desired primary electron energy E_0. For the presented EELS measurements where E_0 was varied from 200 eV to 1000 eV, the FWHM of the peak, originating from elastically reflected electrons, increases from initially 600 meV to 800 meV.

Final Remarks

Physical properties of materials are manifold and rely to a certain amount on each other. For a better understanding of the several aspects and processes influencing important material parameters, several additional experimental methods have been applied, partly with the help of co-workers and colleagues. This includes characterization of structural and optical properties of InN using X-ray diffraction (XRD) and spectroscopic ellipsometry as well as the characterization of the surface electron concentration profile using high resolution electron energy loss spectroscopy (HREELS). Obtained properties from these methods enable a correct interpretation and analysis of the surface electronic properties as well. This includes the structural and electrical characterization of In_2O_3 and ITO(N) thin films. However, since these measurements are of supporting nature, the principles and details of these experimental methods will not be discussed here. However, important results that are correlated to the analysis of surface properties of this work will be taken into account where appropriate.

Chapter 3

Chemical and electronic properties of InN(0001) surfaces

3.1 InN - a promising narrow band gap material

In recent years, the research efforts on the material properties and device processing of group III-nitrides have experienced a strong rise. Heterostructure devices can profit from the extraordinary electronic properties of group III-nitrides, in particular the binary compounds AlN, GaN and InN and their alloys. They are distinguished by a high electron mobility, high drift velocity and the possibility to tune the band gap between 6.2 eV (AlN) and $\sim$ 0.7 eV (InN). Most investigations have concentrated on GaN, AlGaN/GaN heterostructures and Ga-rich InGaN alloys which led to a tremendous progress in InGaN/GaN based light emitting diodes and lasers as well as AlGaN/GaN transistors for high-frequency and high power devices [24].
Compared to the extensive knowledge about the binary III-nitride compounds GaN and AlN, InN is far less investigated and understood. This is mainly related to past problems in epitaxial growth, film quality and the possibility of doping the material. However, calculations on the carrier transport characteristics predict InN to exhibit the highest achievable drift velocity of all known semiconductor materials as well as an extremely high electron mobility [25, 26]. These characteristics promise the realization of ultrafast field effect transistors (FETs) based on InN, if still existing technological problems could be overcome.
Up to the late 90's most properties of InN where determined from magnetron sputtered samples which exhibited a high electron concentration and low mobility. For example the band-gap was determined by Tansley and Foley to be 1.89 eV [27]. Progress in epitaxial growth of InN could be achieved by the adaption of metalorganic vapor phase epitaxy (MOVPE) and molecular beam epitaxy (MBE), which were first demonstrated in the early 90's [28, 29]. Since then a tremendous improvement in the materials properties has been achieved. Most of the research was focused on improvement of epitaxial growth and film quality by optimization of growth process and compensation of the lattice mismatch-induced strain using AlN, GaN or LT-InN buffer layers [30, 31, 32, 33, 34]. Simultaneously, the basic characterization of the material, such as the optical and electrical properties, was expedited. For example, the band-gap of InN was a matter of debate in recent years [35, 36, 37]. Since

experimental [38, 39, 40] and theoretical [41, 42] studies strongly suggested a correction of the old band-gap value, it is now commonly accepted to lie below 0.7 eV. Concerning the electrical properties, an electron concentration in the range between 10^{17} cm^{-3} and 10^{18} cm^{-3} could be achieved and electron mobilities up to 3500 cm^2/Vs have been reported [33, 43]. These values were already sufficient for the realization of the first InN-based transistor [44]. The unique electronic and optical properties of InN are of further interest for optoelectronic applications, solar cells and sensor applications [45, 46]. Particularly, the possibility of producing high efficiency InN-based terahertz emitters facilitates a wide variety of applications [47, 48].

3.2 Electron accumulation at InN surfaces

To establish understanding of the material, a detailed knowledge of the electron density of states (DOS) is helpful to predict electrical and optical properties of InN. Photoelectron spectroscopy (UPS and XPS) and high-resolution electron energy loss spectroscopy (HREELS) are suitable methods to investigate the electron valence band DOS and the electron density profile in the near surface region. However, information on the surface properties of InN is limited to a few experimental studies. This is mainly related to the difficulty of preparing contamination-free and well-ordered surfaces with stoichiometric composition. For example conventional ion bombardment leads to preferential sputtering of nitrogen and therefore to an indium enrichment at the surface [49, 50]. It was shown that a combination of atomic hydrogen cleaning (AHC) and annealing is a suitable method to remove surface contamination from InN without affecting the surface quality [51], but the existence of In-adlayers on surfaces prepared by optimized AHC was discovered recently [52]. For non-ideal conditions, even the formation of metallic droplets could be observed [53, 54].
By measuring the carrier plasmon energy on AHC-cleaned InN(0001) samples using HREELS and subsequent simulation of the spectra by semi-classical dielectric theory, a strong accumulation of electrons at InN surfaces as well as at InN/GaN and InN/AlN interfaces was discovered [55, 56]. The electron concentration in this accumulation layer is as high as 10^{20} cm^{-3} resulting in a sheet carrier concentration up to 10^{14} cm^{-2} [57]. Intensive studies led to the conclusion that this characteristic is due to the unique band structure of InN. It exhibits an unusually low conduction band minimum at the Γ-point and a very high electron affinity. As a result, the branch point energy E_B or the charge neutrality level, which is the crossover point from donor-type to acceptor-type surface states, is located well above the conduction band minimum. This allows donor-type surface states to emit their electrons into the conduction band. Hence, the surface Fermi level tends towards E_B, giving rise to electron accumulation at the surface [58, 59, 60].
A microscopic description of the origin of Fermi level pinning can be found in possible surface states [61, 62]. For InN(0001) films produced at moderate In/N ratios, an indium-induced (2×2) reconstruction has been predicted by theoretical calculations resulting in the existence of occupied In-In bonds above the CBM which pin the Fermi level. The same is true under In-rich conditions where the In-polar (0001) surface is covered by a laterally

contracted In bilayer. At this high coverage, the In-In bonds and dangling-bond states strongly interact, leading to a large energy dispersion within the band gap. A similar behavior is found for nonpolar InN surfaces prepared at In-rich conditions. In contrast, for moderate In/N ratio an absence of occupied states inside the conduction band is predicted on m- and a-plane InN and hence, no electron accumulation would exist when the samples are prepared under these specific conditions [61, 62]. However, electron accumulation has been found experimentally on m-plane and a-plane as well as cubic InN surfaces [63, 64]. The surface electron layer influences the electrical properties of InN films and the complex consequences of this aspect on the performance of InN-based devices are the topic of ongoing research. Crucial will be the open question whether there is a possibility to control the carrier density in the accumulation layer, which will have strong impact on the switching behavior in InN transistors and is also an important parameter for chemical and biological sensors applications.

3.3 Examination of InN surfaces which have been exposed to ambient conditions

The evaluation of surface properties of InN samples that have been transported through ambient conditions is only possible if suitable preparation routines can be employed. Since a device for atomic hydrogen cleaning was not available at the used surface analysis system, a different approach was chosen. Samples that have been grown by V. Lebedev in the Nitride-MBE system of the Nanotechnology group at ZMN, were, after growth, transferred as quickly as possible through air into the UHV system in order to minimize the exposure time to contaminants. Other InN samples as for example from H. Lu and W. J. Schaff (Cornell University) had been stored for longer time in ambient conditions. The subsequent annealing at temperatures below 250°C was relatively successful to reduce the amount of oxygen at the surface. However carbon related contaminants could not be affected by this treatment. The results of these examinations are published in [34, 65, 66].
For samples with a thickness of ~ 800 nm, where the coalescence of the initially formed islands has not been finalized during growth, surface steps could be measured using contact-mode AFM measurements. Fig. 3.1 shows AFM scans performed on one of these samples. The surface consists of an arrangement of homogeneously distributed islands with an average diameter of ~ 50 nm which has been formed during the intermediate growth state. The islands are not well separated but seem to be connected due to coalescence as can be deduced from the high resolution normal force scan on the right-hand side. The formation of this well-arranged geometry with directly visible surface steps, which are confined within the islands, leads to the conclusion that the growth process is strongly influenced by the fact that the adatom surface migration is sufficiently high to allow the formation of regular stepped structures. The measured step height of ~ 6 Å corresponds well with the crystal structure of InN. This distance is in good agreement with the c lattice parameter of 5.7 Å within the accuracy of the AFM measurement.
A number of different information on the surface chemistry and valence band structure has been obtained by XPS and UPS measurements on these InN samples [34, 65, 66]. This

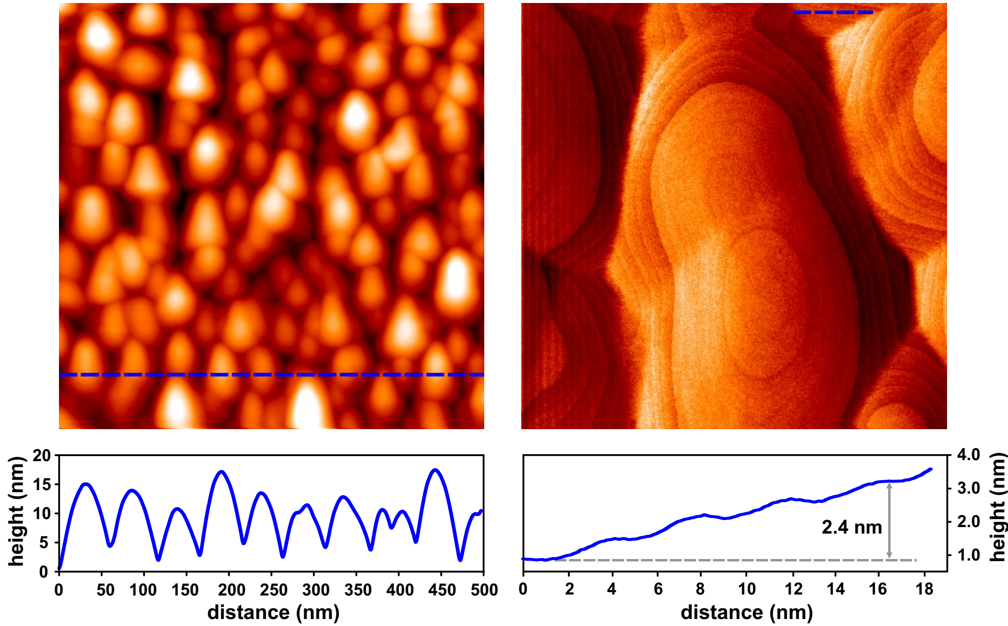

Fig. 3.1: Contact mode AFM scans and line profiles of an InN surface in the stage of island coalescence at low thickness. Left image: $500 \times 500\,\mathrm{nm}^2$ scan of the sample topography. Right image: $100 \times 100\,\mathrm{nm}^2$ normal force scan showing the existing steps with a height of $\sim 6\,\mathrm{Å}$. The lines indicate the locations where the line profiles (bottom) were measured.

includes the determination of the core level binding energies and chemical states at InN as well as the examination of the valence band characteristics. Non intentionally doped and Mg-doped InN layers were analyzed by AES sputter depth profiling combined with PES measurements. On the surface of both types of layers a high concentration of oxygen and a strong accumulation of electrons was observed. However, in contrast to the undoped layers the conductivity profile of Mg doped InN shows a strong discontinuity close to the surface. From the shift of the In(MNN) peak in AES and the determination of the valence band maximum with respect to the Fermi level by UPS, differences in the surface band alignment between both InN types could be evaluated. By the combination of AES and UPS, a model for the band bending is proposed, which is displayed in Fig. 3.2. In the bulk of the Mg-doped InN the In(MNN) peak shift of about 0.15 eV demonstrates the influence of the Mg on the Fermi level, while the surface is clearly n-type. This characteristic demonstrates that Mg doping indeed can compensate the n-type conductivity in the bulk and is therefore a prospective candidate to achieve p-type doping in InN [66, 67].
The gained experience and the identified problems of surface preparation of externally produced InN films initiated the idea to perform investigations on samples that have been directly prepared by MBE in the growth and surface analytic system in order to exclude any effects related to surface impurities from transport in air. The realization of these investigations and the consequential results are described in the next sections. In the first step, the growth parameters were optimized and their influence was analyzed. Subsequently the properties of InN(0001) films with a stoichiometric surface composition were examined using electron spectroscopy and electron diffraction methods.

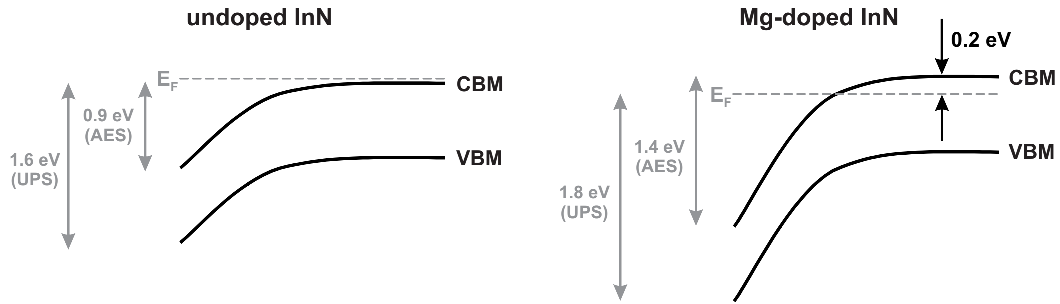

Fig. 3.2: Surface band bending and bulk Fermi level of nominally undoped (left) and Mg-doped (right) InN.

3.4 Influence of In/N flux ratio on the surface properties of InN grown by PAMBE

With the aim to study clean InN surfaces, the realization of epitaxial growth of InN films using MBE had to be established first. This was supported by a accompanying Diplom thesis by A. Eisenhardt [68]. Within this period, important growth parameters, e.g. the settings of the indium and nitrogen sources as well as the substrate growth temperature have been optimized in order to produce crystalline and stoichiometric InN films. Taking into account the required substrate conductivity for electron spectroscopy measurements, Si-doped GaN(0001)/Al_2O_3(0001) templates from TDI, Inc. were chosen as substrates in order to avoid disturbances resulting from charging effects which are typical for high quality undoped GaN templates. The used template consists of a MOCVD grown 5 μm thick GaN:Si film with a specified carrier concentration of $n \sim 6 \times 10^{18}$cm^{-3}.
The parameters for the growth of In-polar InN films were adjusted following the available phase diagrams of InN(0001) growth published by Dimakis et al. [69, 70] and Gallinat et al. [71]. The In film quality is mainly restricted by the extremely low decomposition temperature of InN as well as the strongly enhanced desorption rate of nitrogen at temperatures above 450°C. These properties indeed contradict the aim of a sufficient mobility of indium and nitrogen atoms at the surface, which is enhanced at higher temperatures, and restrict the growth temperature to 470 - 480°C for In-polarity InN. Of further importance is the fact that smooth InN surfaces formed by step-flow growth behavior due to higher adatom mobility, were only achieved at fairly high In-flux resulting in the simultaneous accumulation of metallic indium at the surface. Metallic droplets are typically removed by etching of the sample surface in HCl vapor after growth. However, for the implementation of electron spectroscopy for *in-situ* surface analysis, excess indium on the surface has to be avoided. On the other hand, N-rich conditions lead to three-dimensional growth of the InN films. Consequently, the basis premise of the optimization of growth parameters in this work was to achieve stable growth conditions where a stoichiometric InN surface composition could be realized. Aspects of surface morphology, were also important, but only as a secondary parameter. The influence of growth conditions on the surface composition is presented in

this section while the subsequent analysis of the surface electronic structure will mainly focus on the results for optimized, stoichiometric InN surfaces. Effects of indium accumulation on the surface properties of InN films grown at high In/N flux ratio are discussed in [68].
The substrate temperature was estimated by linear extrapolation of a pyrometer calibration curve measured at temperatures above 600°C. All numbers are given with respect to this reference. It has to be stated, that this procedure for the specification of temperatures in the lower region (300 - 500°C) leads to a non-negligible error of ± 30 K for the absolute values. However, the stability and reproducibility of the performed experiments is complied and the error in relative temperature values is below 5 K. Since the flux of reactive nitrogen species to the surface is the limiting factor for the growth rate in the "mini-MBE" system, the settings of the N_2 plasma source were chosen to allow stable operation conditions but remained unchanged if not otherwise indicated (the nitrogen partial pressure was 3×10^{-5} mbar and the plasma source was operated at 350 W). The main parameters for growth optimization were therefore the temperature of the In cell to regulate the metal flux as well as the substrate temperature which influences the adsorption/desorption balance of In and N as well as the mobility of atoms at the surface [71].

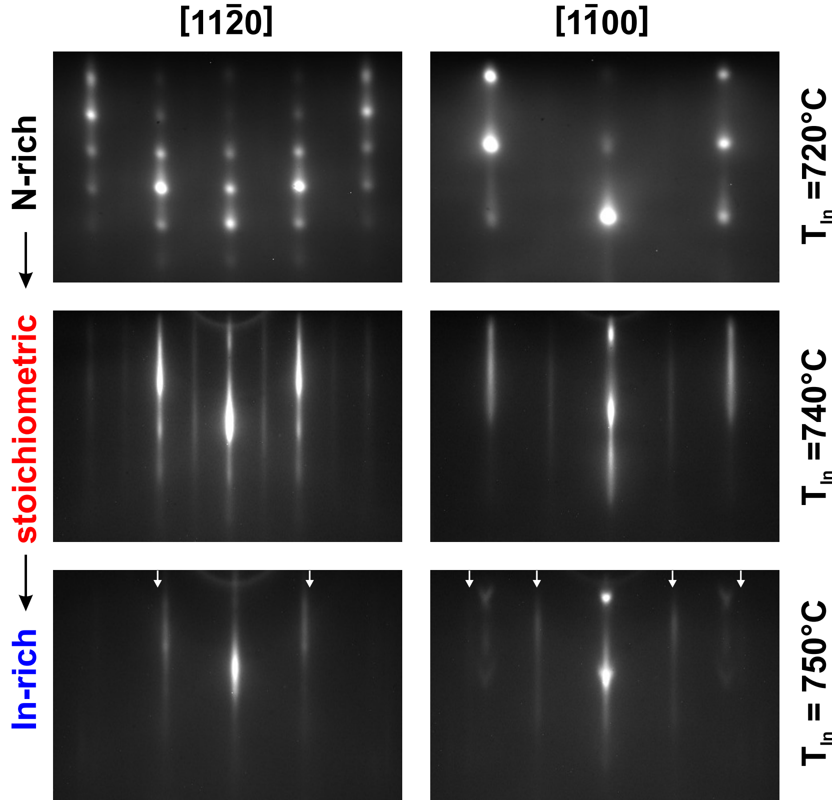

Fig. 3.3: Variation of the RHEED patterns of InN films deposited with different In/N flux ratio during PAMBE growth at 440°C. Shown are the diffraction patterns along the [11$\bar{2}$0] and [1$\bar{1}$00] direction.

Before InN deposition, the GaN templates were heated up to 720°C in a nitrogen plasma to remove contaminations from the wafer surface. Special care was taken to avoid roughening

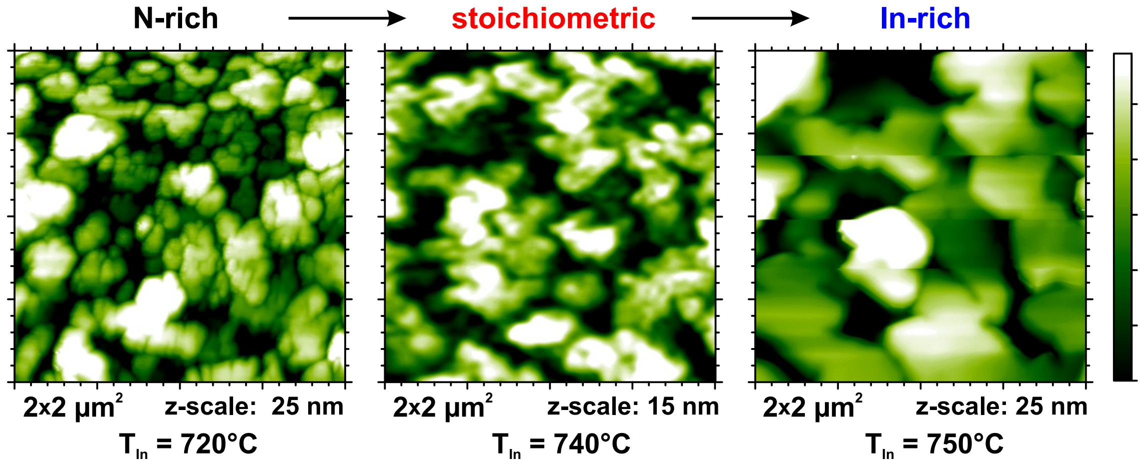

Fig. 3.4: Dependence of the topography of InN films on the In/N flux ratio during PAMBE growth at 440°C measured by non-contact atomic force microscopy.

of the surface which occurs when annealing is performed at slightly higher temperatures. This procedure results in the formation of a sharp (1x1) RHEED pattern and a strong reduction of residual oxygen and carbon impurities at the surface (< 0.2 ML) as determined by XPS. Afterwards, the samples were cooled down to the desired growth temperature, where the InN growth was initiated by opening the shutter of the indium Knudsen cell. The growth was monitored *in-situ* by RHEED. All produced samples had a relatively low thickness between 100 and 300 nm, which is related to the relatively low growth rate of 20 - 40 nm/h.

For a growth temperature of 440°C, the influence of the In/N flux ratio on the RHEED pattern after growth is presented in Fig. 3.3 in a series varying the In evaporator temperature as parameter between 720°C and 750°C. In the following three different stages of sample stoichiometry resulting from different In-flux settings are compared, denoted "N-rich", "stoichiometric" and "In-rich" conditions. As expected for the lowest used In flux, the RHEED pattern exhibits a strong contribution from 3-dimensional diffraction spots, a clear indicator for island formation at the surface. The results of the RHEED analysis stands in direct correlation to the sample topography, measured by AFM after growth (see Fig. 3.4). For $T_{In} = 720$°C, the topography of the sample is relatively rough and characterized by the existence of small crystallites with a diameter below 100 nm that are partly converged to larger agglomerates. This behavior is typically found for N-rich growth conditions [69, 70, 71]. The increase of the indium flux results in an improvement of the RHEED pattern. The intensity of the transmission spots is strongly reduced and a streaky RHEED pattern is formed during growth.

The pictures in Fig. 3.3 represent the status after growth and subsequent cooling down of the samples in the nitrogen plasma. It has to be mentioned that during growth a (1×1) surface structure was always observed. Any additional structures in the RHEED patterns, indicative for the formation of possible surface reconstructions have only been observed after closing the In-shutter and reducing the sample temperature while the plasma source was still in operation. The nitrogen source was typically switched off at 300 - 250°C. For the case of $T_{In} = 740$°C, the formation of a (2×2) surface reconstruction is concluded from

the clearly visible half order streaks in both crystal directions. This is an indication for a relatively ordered atom arrangement at the surface. The topography is also improved, but a relatively high roughness is still present (4 - 5 nm rms). For even higher In flux, the surface quality is further improved. In this case, the AFM scan shows the formation of larger and partly coalesced crystallites with a diameter of a few hundred nanometers (see Fig. 3.4). This observation is in in very good agreement with the already discussed tendency that slightly In-rich conditions lead to a higher adatom mobility resulting in improved growth conditions. Since the sample thickness was only ~ 150 nm, it is anticipated that under these growth conditions, a smooth topography can be obtained for thicker layers induced by further coalescence of the islands [34]. However, as will be discussed below, these settings already result in strong accumulation of metallic indium at the surface that makes a determination of the InN properties by PES difficult. A first indication of excessive indium at $T_{In} = 750°C$ is already visible in the corresponding RHEED pattern. During growth, the intensity of the streaks in the RHEED signal is weaker compared to the settings with lower In flux and furthermore a homogeneous background signal is detected in between the streaks. This is an indication for the existence of an unordered surface layer during growth. As soon as the In-shutter is closed, the intensity of the streaks recovers drastically in intensity indicating ordering of the topmost surface layers. The final diffraction pattern after cooling down is presented in Fig. 3.3. Additional weak streaks with a different spacing compared to the reciprocal lattice of InN appear which are marked by white arrows for better visualization. It indicates the formation of a contracted In adlayer at the InN(0001) surface. In the $[1\bar{1}00]$ direction, the spacing ratio between the outermost streaks of the In- and InN-related signal in the RHEED pattern is 1.14 which corresponds to a factor of 0.88 in real space. Accordingly, the spacing ratio in the $[11\bar{2}0]$ direction is estimated to be 0.91. These values are in good agreement with the lattice constants ratio of In and InN ($a_{In}/a_{InN} = 3.2523$ Å / 3.5446 Å $= 0.92$). This observation is in agreement with theoretical works, since a laterally contracted In-bilayer has also been predicted by DFT calculations to be the most stable arrangement under highly In-rich conditions [72].

Besides the variation of the surface morphology upon increasing In-flux, differences have also been found in the photoelectron spectra. A comparison of the most important core level spectra of InN samples grown using different In/N flux ratios and different substrate temperatures are presented in Fig. 3.5. For each growth temperature, the flux ratio has been adjusted in the same way as described above for the example of 440°C. For stoichiometric and N-rich conditions, the $In3d_{5/2}$ and N1s core levels have their maximum intensity at a binding energy of 443.7 eV and 396.0 eV, respectively. As already mentioned, a non-stoichiometric surface composition is found for the In-rich growth conditions. This can be directly deduced from the decrease in N1s intensity found for these settings (blue curve in Fig. 3.5), since all spectra are normalized to the same $In3d_{5/2}$ peak height. Assuming a homogeneous coverage, the thickness of the indium film is calculated from the attenuation of the N1s intensity compared to stoichiometric films to be 0.5 nm (1.5 - 2 ML). Additionally, a shift of the core levels by 0.25 eV towards lower binding energy is observed in this case, approaching the value of the $In3d_{5/2}$ core level of metallic indium as reference.
In some cases, the N1s signal contains a second feature at 397.7 eV. Its intensity depends on the used growth temperature and the In/N flux ratio. For N-rich conditions at 400°C it

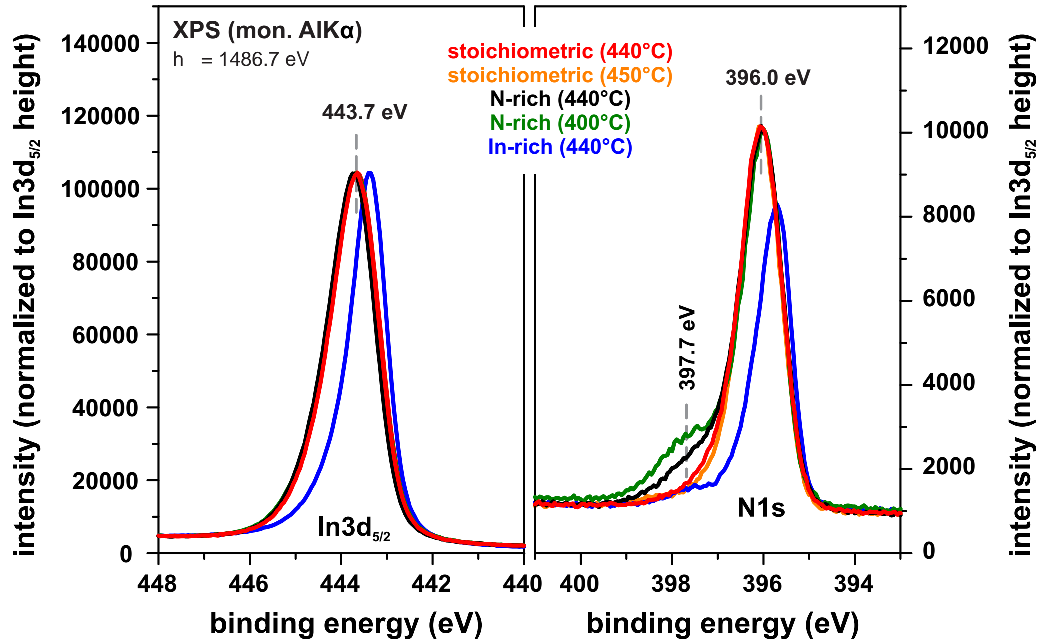

Fig. 3.5: $In3d_{5/2}$ and N1s core level spectra of *in-situ* prepared InN films. Compared are samples that have been grown at different In/N flux ratio and different substrate temperatures. For further details see text.

is observed as a directly visible peak with an amount of ~15% compared to the main N-In structure. As clearly visible, this feature is only present as a shoulder on the high binding energy side for $T_{growth} = 440°C$ for N-rich growth, while under stoichiometric conditions, this feature is absent resulting in a narrow peak with a slight asymmetry. Finally at 450°C the N1s peak exhibits the smallest FWHM. Due to the performed *in-situ* analysis of the sample stoichiometry and, hence, absence of carbon- or oxygen-related impurities within the detection limit of XPS, this additional structure at 397.7 eV cannot be attributed to N-O bonds, which have been observed at the surface after transport through ambient conditions [34]. It is concluded that this structure in the N1s spectra is caused by incorporated nitrogen species due to the excess nitrogen supply. In a study on differently prepared InN films it has been suggested that point defects such as antisite defects (nitrogen on metal site), indium vacancies or N interstitials could cause this level with shifted binding energy [73].

Interestingly it was found that the samples grown at N-rich conditions and lower temperatures exhibited an additional signal in XRD measurements as well. In Fig. 3.6 the ω-2Θ scans of the InN(0004) reflex for two different samples, prepared under stoichiometric (red curve) and N-rich (black curve) conditions, are compared[1]. One has to be aware that the intensity axis is presented in logarithmic scale. The red curve exhibits an extra peak at 64.8° close to the InN(0004) signal which might be related to the excess nitrogen growth conditions. However, normally for defects inserted into the bulk crystal, a strain-induced change in the lattice constant would be expected resulting in a shift of the single peak

[1]X-ray diffraction analysis was implemented using a Bruker AXS D8 high resolution X-ray diffractometer. The measurements were performed by K. Tonisch

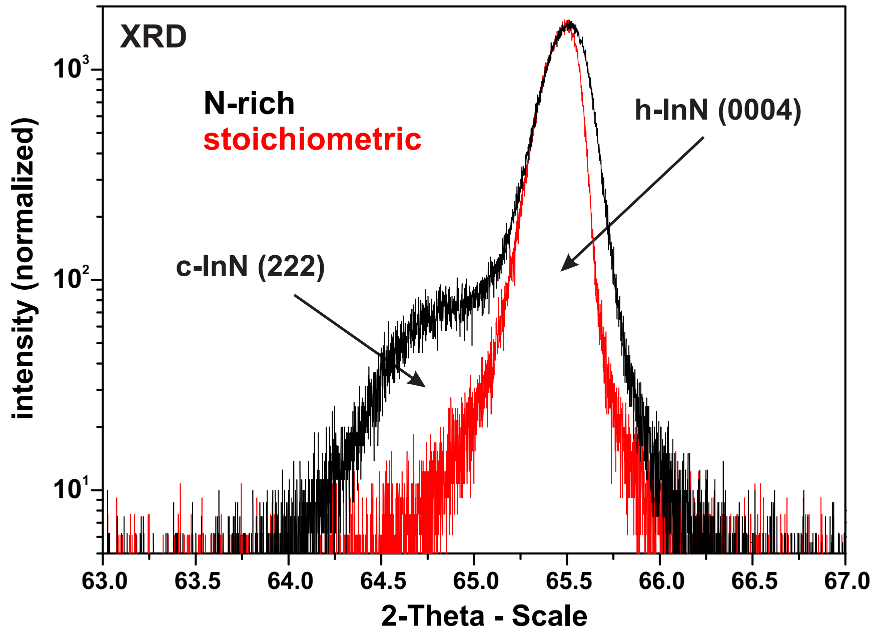

Fig. 3.6: XRD ω-2Θ scans of the InN(0004) reflex comparing InN samples with and without excess nitrogen.

in the X-ray diffractogram, rather than occurrence of a second component. A detailed analysis of the additional structure in the measured symmetric (0002), (0004), (0006) and asymmetric $(1\bar{1}05)$ reflexes (not shown) results in the conclusion that this structure is due to the formation of cubic InN crystallites during growth at nitrogen-rich conditions. For example, the structure in Fig. 3.6 at the angle of 64.8° corresponds to the (222) reflex of cubic InN. In correspondence, a second feature related to the cubic (333) reflex of InN was found close to the (0006) peak and a (224)-related signal in the surrounding of the $(1\bar{1}05)$ reflex. Possibly this cubic phase is formed during initial nucleation of cubic crystallites at the InN/GaN interface under the used N-rich conditions. This effect has been reported to occur in the wetting layer during growth of InN on GaN(0001) [74] and is explained in terms of energetic stability of the cubic phase due to the incorporated strain. This is believed to be the underlying phenomenon the leads to the unusual results of the XRD measurements on the samples grown at N-rich conditions. After the initial first layers of InN growth, the hexagonal phase is more stable and is of course the dominating part in the MBE grown InN samples. Nevertheless, the formation of cubic crystallites in the beginning of the InN growth does not correspond to the detected second chemical state in the N1s core level spectrum. The difference in crystal structure (wurtzite vs. zincblende) cannot induce the large shift of the electron binding energy of 1.7 eV and therefore, as discussed above, the additional N1s feature must be caused by excess nitrogen that is inserted into the film.

The variation of In/N flux ratio during InN MBE has further influence on the surface properties of the films. X-ray photoelectron spectra of the shallow In4d core level and the valence band distribution measured using monochromated AlKα radiation are compared in Fig. 3.7 for the different growth parameters. As already observed for the In3d$_{5/2}$ peak, no difference is found between the spectrum of a sample prepared at stoichiometric conditions compared to a surface that has been prepared at a high N-flux. A direct extrapolation of the

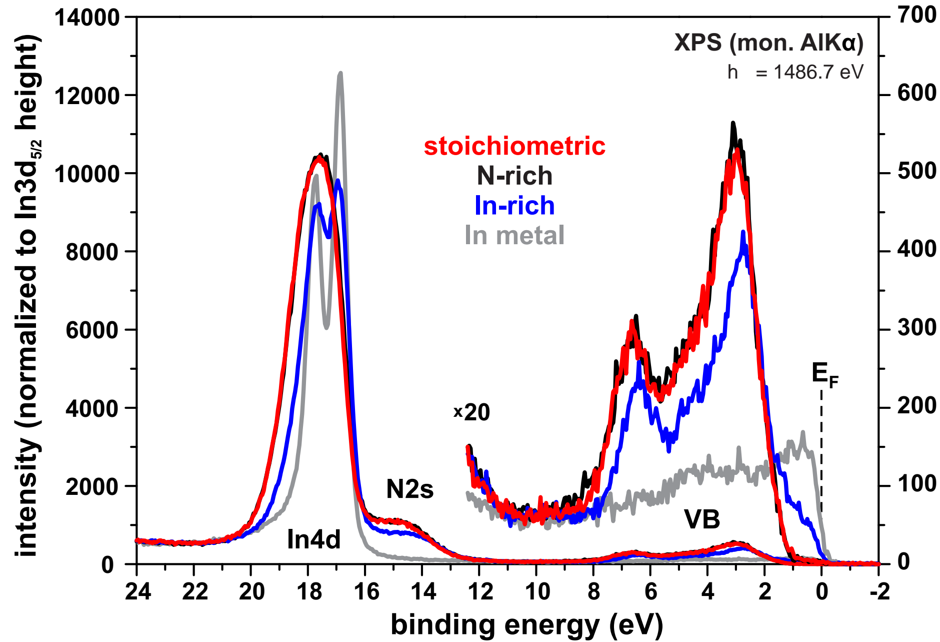

Fig. 3.7: Photoemission spectra of the InN valence band and the In4d and N2s semi-core level measured using monochromated AlKα radiation ($h\nu = 1486.7\,\text{eV}$). Presented are measurements of films that have been deposited under different In/N flux ratio in comparison to metallic In.

valence band trailing edge from the XPS scans leads to a valence band maximum of 1.55 eV below the Fermi level E_F. This value is in excellent agreement with published data [60] and proves the existence of the electron accumulation layer at contamination-free InN surfaces. MBE growth at slightly indium-rich conditions modifies this behavior. Most noticeably, now strong electron emission is detected up to E_F and the N2s and valence band intensity, which mainly consists of N2p states, is reduced. Furthermore, the electronic states are shifted by 0.25 eV towards E_F and the In4d spin orbit splitting is well resolved. All these features can be explained by the existence of excess surface indium under these conditions. To support this statement, an indium reference spectrum is plotted for comparison. It has to be mentioned that reports exist which contain VB spectra of InN films prepared by atomic hydrogen cleaning (AHC) that also show electron emission up to the Fermi level [52]. This feature was explained by the formation of stable indium adlayers with a simulated thickness of ~3.4 ML on top the InN crystal lattice for In-polarity InN. Theoretical calculations also predict the stability of metallic adlayer configurations under In-rich conditions [72, 75]. A similar origin can be assumed for the results presented here, since no droplet formation was observed in the AFM measurements.
Using He II radiation to study the valence band and the In4d structure, brings the advantage of being even more surface sensitive. The respective measurements are shown in Fig. 3.8. One has to be aware of some special aspects of these spectra. Since photoelectrons are generated by all spectral lines produced by the UV source, several features in the presented spectra are caused by ghost/satellite lines and do not belong to the actual density of states of InN at the respective binding energy values. First of all, most of the signal below a kinetic energy of 21.2 eV is generated by He I radiation. Furthermore, disturbing signals

from In4d emission induced by the He II β and γ satellites, which occur at 7.56 eV and 10.20 eV higher energy compared to the main line, have to be also considered as artifacts. The trend discussed for the AlKα measurements can be found here (Fig. 3.8) as well. Due to the narrower line width of He II, it is possible to resolve the spin orbit splitting of the In4d peak for the surface with a (2×2) reconstruction that has been prepared using stoichiometric conditions. This is an indication for a good crystalline order at the surface. In comparison, for N-rich growth, this feature is not as well resolved. On the other hand, for In-rich growth, the signal consists also of a superposition from information of InN as well as the indium adlayers.

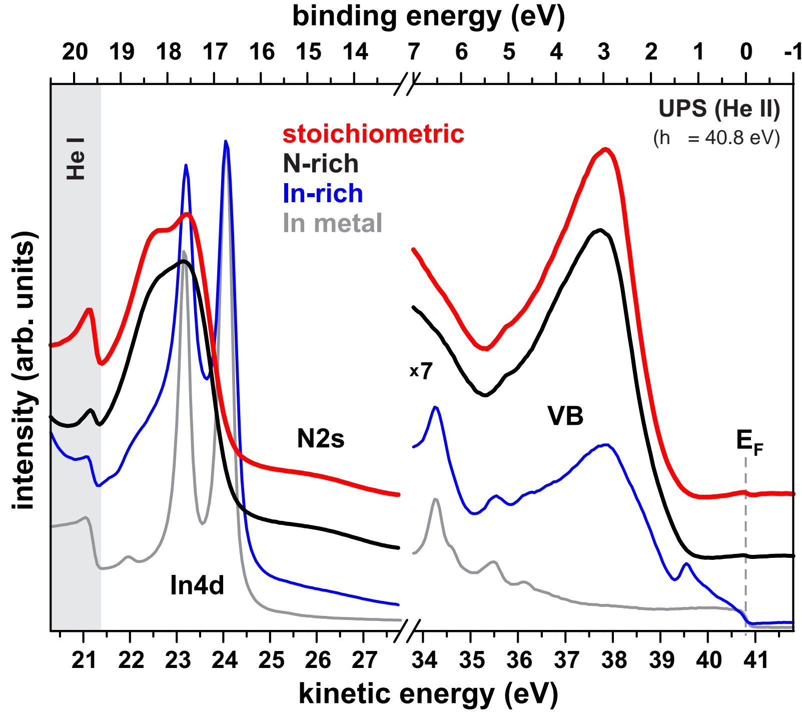

Fig. 3.8: Photoemission spectra of the InN valence band and In4d semi-core level measured using He II radiation ($h\nu = 40.8$ eV). Presented are measurements of films that have been deposited under different In/N flux ratio in comparison to metallic indium.

The work function of the grown samples shows a linear dependency on the In/N flux ratio. For highly N-rich conditions, the highest value of 4.8 eV is measured, while under stoichiometric conditions, the values vary between 4.5 and 4.6 eV. As expected for slightly In-rich growth, ϕ approaches the value of 4.1 eV for metallic indium. In these cases a work function of 4.2 eV is typically measured.
One important fact has to be additionally highlighted. In all UPS measurements, independent of the surface preparation, the electron density reaches up to the Fermi level. A highly nitrogen enriched environment can only partially reduce the intensity of this signal. Especially the fine structure of this feature for the (2×2)-reconstructed surface is an indication for the existence of surface states. This aspect will be addressed in more detail and is discussed in a separate section below (see 3.6.2).

3.5 Bulk properties of InN(0001) samples grown under optimized conditions

For selected samples that have been grown under stoichiometric conditions, a comparative series of external measurements has been realized in order to evaluate the bulk properties of the material since surface sensitive techniques alone cannot be considered for judging the sample quality. X-ray diffraction measurements allow the determination of the crystallographic properties and the lattice constants, while the optical properties were characterized by spectroscopic ellipsometry. Furthermore for one sample it was possible to perform an extensive HREELS analysis in order to determine the surface and bulk electron density. The results are briefly summarized in this section in order to evaluate the quality of the prepared InN films and to prove the reliability of the discussed results on the surface properties.

3.5.1 X-ray diffraction (XRD)

The crystal structure of the samples was characterized by X-ray diffraction measurements at room temperature. Conventional ω-2Θ scans prove the formation of hexagonal c-plane InN films. Only reflexes related to the epilayer as well as the GaN/Al_2O_3 template were found. Hence the existence of other crystalline phases, such as for example the formation of metallic inclusions in the material can be excluded. For the evaluation of the lattice constants of the films, XRD reciprocal space maps across the (0002) and $(1\bar{1}05)$ reflex of GaN and InN were measured. The results are summarized in Tab. 3.1[2]. Compared to available literature

XRD reflex	c (Å)	a (Å)
InN(0002)	5.6965	-
InN$(1\bar{1}05)$	5.6971	3.5432
GaN(0002)	5.1852	-
GaN$(1\bar{1}05)$	5.1865	3.1884

Tab. 3.1: Lattice constants of InN epilayer and GaN template as determined from XRD reciprocal space maps of the symmetric (0002) and asymmetric $(1\bar{1}05)$ reflexes. The sample was grown at 440°C under stoichiometric conditions and has a thickness of ~320 nm.

data, the resulting lattice constants of $a = (3.543 \pm 0.001)$ Å and $c = (5.697 \pm 0.001)$ Å are in agreement with the observed dependency of c and a on the introduced biaxial strain depending on film thickness and growth mode. The determined values indicate that the prepared films are slightly tensily strained [76, 77].

[2] X-ray diffraction analysis was implemented using a Bruker AXS D8 high resolution X-ray diffractometer. The measurements were performed by K. Tonisch

3.5.2 Spectroscopic ellipsometry (SE)

For the examination of the optical properties of InN films grown at 440°C and 450°C, samples were hand over to the Experimental Physics I group at TU Ilmenau, which has extensive experience in the characterization of optical semiconductor properties, especially of III-Nitrides. Variable angle spectroscopic ellipsometry was performed in the energy range from 0.7 eV to 5.0 eV using a commercially available rotating-analyzer ellipsometer (Woollam VASE) at incidence angles of 62°, 68° and 74° with respect to the surface normal[3]. The samples were examined according to their studies on In- and N-polarity hexagonal InN films [78]. The real (ϵ_1) and the imaginary part (ϵ_2) of the complex dielectric function $\bar{\epsilon} = \epsilon_1 + i\epsilon_2$ were obtained by fitting the experimental data Ψ and Δ using a multilayer model similar to the procedure reported in [79]. In that way, the InN film thickness could be determined. Taking into account the Burstein-Moss shift and band-gap renormalization due to occupancy of the conduction band as well as the intrinsic InN band-gap of 0.68 eV, the bulk carrier concentration can be estimated by a comparison of the calculated shape of the imaginary part of the dielectric function with the experimental data (see Fig. 2 in Ref. [78]).

For the examined samples, the bulk carrier concentration was estimated to lie between 8×10^{18} cm^{-3} and 1×10^{19} cm^{-3}. In comparison to the typical values obtained for MBE grown InN films, this carrier concentration is about one order of magnitude higher. This fact can partially be explained by the relatively low film thickness (250 - 300 nm) of the produced InN samples. Normally, the dislocation density as well as the carrier concentration is drastically lower at a film thickness above 1 μm [43]. However, due to the low growth rate of $\sim$20 nm/h, such a thickness of the InN films could not be achieved in a reasonable time with the given setup.

3.5.3 High-resolution electron energy loss spectroscopy (HREELS)

High-resolution electron energy loss spectroscopy (HREELS) measurements were performed on a sample with a thickness of 320 nm. For this purpose, the as-prepared sample was transferred via a high-vacuum transport box to a second UHV system equipped with a HREEL spectrometer. It allows transfer of samples without exceeding a pressure of 1×10^{-5} mbar for approximately 1 hour. In this manner, sample contamination could be minimized enabling measurements without any further preparation steps. For evaluation of the electron density profile inside the InN film, a series of HREEL spectra were measured varying the primary electron energy E_0 from 1 eV to 200 eV. Besides the detected vibrational modes such as the InN Fuchs-Kliewer phonon at 566 cm^{-1} (70.2 meV) as well as the C-H stretching and bending modes, the shift of the carrier plasmon could be evaluated. Since the probing depth for inelastic scattering is inverse proportional to the scattering vector

$$q_{\parallel} = \frac{\sqrt{2E_0 m_e}}{\hbar} \cdot sin(\Theta) \cdot \left(1 - \sqrt{1 - \frac{E_L}{E_0}}\right) \tag{3.1}$$

which depends on the used primary energy E_0, the respective loss energy E_L (the measured carrier plasmon energy in this case), the electron mass m_e and the chosen scattering geome-

[3]The SE measurements as well as the subsequent modeling were carried out by P. Schley.

try (all measurements were performed in specular geometry with the chosen scattering angle of $\Theta = 55°$ with respect to the surface normal), the carrier density profile can be probed by varying the primary electron energy E_0. Resulting spectra from the performed HREELS measurements and the dependence of the carrier plasmon (CP) energy on E_0 are presented in Fig. 3.9 together with the calculated probing depth variation according to Eq. 3.1. The obtained values are compared to published measurements on samples prepared by MBE and by high-pressure CVD [80, 81]. The variation found is in very good agreement with the values reported for MBE-grown samples. However, an extension of the primary electron energy to lower as well as higher values up to 200 eV allows a more detailed analysis of the electronic properties in the electron accumulation layer. From theoretical modeling of

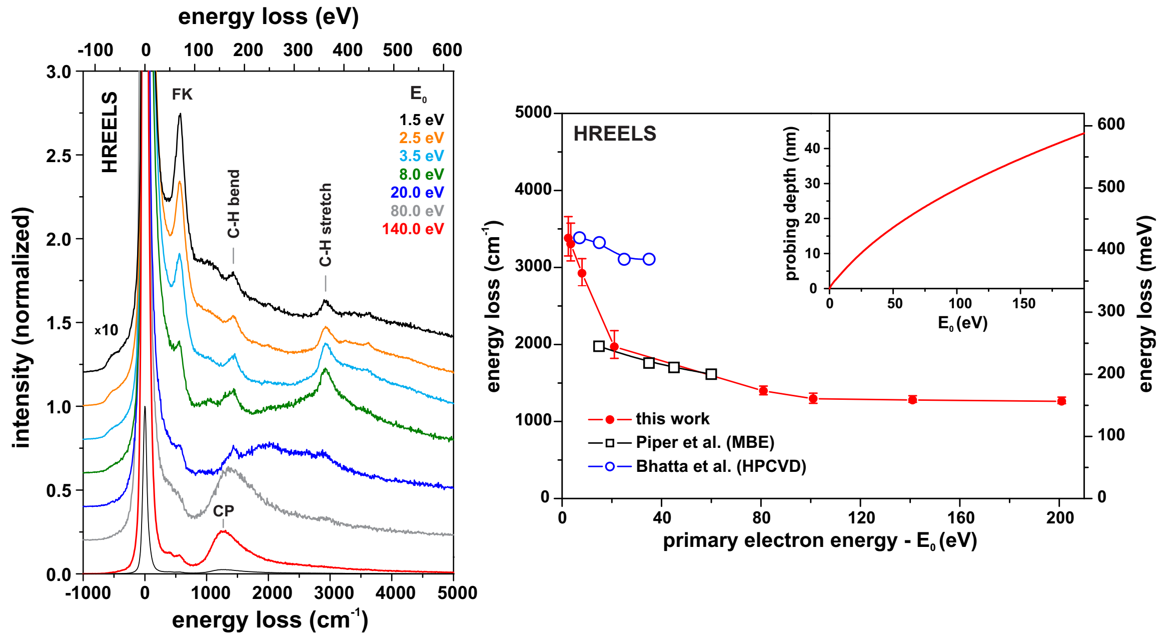

Fig. 3.9: Results of the HREELS measurements on InN(0001) (left) and the corresponding variation of the carrier plasmon induced energy loss in dependence on the used primary electron energy (right). Values from own measurements are compared to available data in the literature [80, 81]. The inset shows the corresponding dependence of the probing depth according to Eq. 3.1.

the carrier density profile and the band distribution and their comparison to the HREEL spectra, the bulk electron concentration was estimated to be $\sim 8 \times 10^{18}$ cm^{-3}. This value is in very good agreement with the results obtained by the optical characterization from spectroscopic ellipsometry measurements. Furthermore, the electron density at the surface accumulation layer has a maximum value of $\sim 3 \times 10^{19}$ cm^{-3}, approaching the bulk concentration within the first 15 nm from the surface [82].

In conclusion, the sample quality obtained for the prepared InN films is already respectable and particularly sufficient for the desired examination of the surface properties of InN thin films and their interaction with atomic or molecular species using electron spectroscopy. Some drawbacks in the surface morphology and electron concentration have to be accepted with respect to the best samples prepared by groups that are specialized in MBE and/or MOVPE growth of group-III nitrides. This is mainly related to the restricted film thickness that can be realized in the used MBE growth setup.

3.6 Electronic properties of clean InN(0001) surfaces probed by electron spectroscopy

In this section, the surface electronic structure of InN samples, that have been produced after careful optimization of all growth parameters, to assure a clean surface with stoichiometric composition, are described.

3.6.1 Occupied and unoccupied electronic states

The possibility to investigate several aspects of the density of occupied electron states by means of photoelectron spectroscopy has already been presented above. Such investigations have been applied in the past using X-ray photoelectron spectroscopy to support bulk band structure calculations from density functional theory as well as to analyze the effect of downward band bending induced by the formation of the electron accumulation layer [83, 60]. Implementing X-rays, the resulting VB spectra are comparable to the bulk density of states integrated over the whole Brillouin zone of the material. The first aspect is caused by the fact that the inelastic mean free path of electrons with a kinetic energy around 1500 eV is relatively large (between 25 and 30 Å). Therefore, the resulting signal consists of information integrating over several lattice planes. In contrast, the implementation of ultra-violet photoelectron spectroscopy for the examination of the surface valence band density of states is strongly restricted to adsorbate-free samples due to the extremely low electron inelastic mean free path in this case. Hence, such investigations are strongly linked to the preparation of the samples and have so far not been satisfactory [49, 65].
For a correct interpretation of the PES measurements, one further aspect has to be considered. Since the analyzer electron optics determines the angular acceptance angle $\Delta\Theta$ of the detected electrons, only electrons in a certain range of the wave vector component parallel to the surface are detected in the normal emission geometry. Hence, the measured valence band spectra consist of a summation of electron states in the Brillouin zone around the Γ-point. Depending on the kinetic energy of the emitted electrons and the analyzer acceptance angle, only parts of the whole electron states in the Brillouin zone are accessible according to

$$k_{\|,max} = \frac{\sqrt{2E_{kin}m_e}}{\hbar} \cdot sin(\Delta\Theta) \tag{3.2}$$

This dependency is depicted in Fig. 3.10 for the used experimental settings (acceptance angle of 8°). In the energy range of XPS measurements, the whole Brillouin zone is covered, while for the He I and He II as well as the secondary electron region only states from a certain proportion around the Γ-point are analyzed, which gives a limitation of the performed measurements. On the other hand, this aspect enables k-mapping of the occupied electron states using angle-dependent UPS measurements. However, the above discussed aspects are only strictly true for perfectly flat single crystal surfaces. Since the investigated InN samples have a topography with a roughness of 4 - 5 nm, an additional contribution in the photoelectron spectra is caused by emission of electrons from other crystal directions than the c-plane. A quantification of this effect is almost impossible, but in summary it has to be kept in mind that UPS spectra do not contain information about the whole set of states

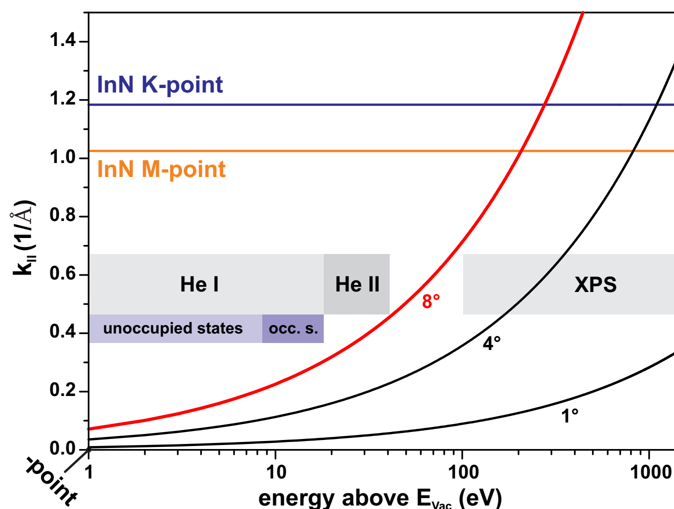

Fig. 3.10: k-dependence of the detected electron states in PES for different analyzer acceptance angles ($\Delta\Theta = 1$, 4 and 8°). For a given electron energy, the information in the PES spectrum includes information from electron states of a certain k-range ($0 \leqq k_{\parallel} \leqq k_{\parallel,max}$).

in the Brillouin zone.
In addition to the usually investigated occupied electron states in PES, further information on unoccupied states can be obtained by the analysis of the fine structure of the secondary electron cascade peak. Most of the information on unoccupied states is currently available from ellipsometry measurements [40, 84] and soft X-ray emission/absorption (XES/XAS) experiments [85], which were already compared to results from band structure calculations. For the involved processes, typically the projected partial density of p-like states (p-DOS) has to be considered [84, 85].
An example of a complete photoelectron spectrum excited by He I radiation is shown in Fig. 3.11. Such spectra normally contain a superposition of information from electrons that have not suffered any energy loss during movement towards the surface and those which were subject of inelastic scattering. Due to the special distribution of the energy levels in InN (the density of states between the In4d level and valence band region is almost zero - see Fig. 3.7), these two contributions can be divided. The region between the abrupt onset of the secondary cascade peak, which represents the position of the vacuum level E_{Vac}, and a kinetic energy of ~ 15 eV contains no spectral information of occupied InN states. Since the cascade peak of true secondary electrons normally represent a broad and featureless signature, as exemplarily indicated in the picture as gray graph, any fine structure is related to electrons that were scattered into unoccupied states above E_{Vac} before exiting the surface. Since multiple scattering processes are involved, the resulting energetic levels represent states from the complete density of states (s-, p- and d-like). The separation between occupied and unoccupied states for InN can therefore be made by a simple cut through the He I spectrum as indicated in Fig. 3.11. In that way the information of PES measurements are expanded to unoccupied states up to ~ 12 eV above the Fermi level. Unfortunately, since electrons that are scattered into unoccupied states below the vacuum level cannot exit the surface, the region between E_F and E_{Vac} is not accessible by PES in this way.
For stoichiometric InN(0001) films prepared using the optimized growth conditions, the

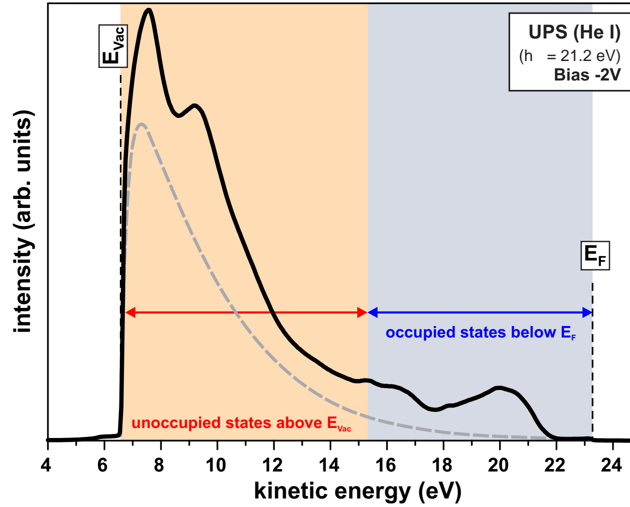

Fig. 3.11: Schematic of the different energy regions in a He I spectrum of InN that contain information about occupied states below the Fermi level E_F as well as unoccupied states above the vacuum level E_{Vac}.

whole energetic distribution is presented in Fig. 3.12, including a compilation of the photoelectron spectra obtained using different excitation sources. It consists of occupied electron states around the shallow In4d core level around -18 eV, well defined structures in the valence band between -8 and -1 eV as well as features up to 12 eV above E_F. The resulting energy distribution is compared to published results from DFT calculations of the density of states from the groups of F. Bechstedt [83] and C.G. Van de Walle [61]. Of great importance for the exact determination of the band structure is the correct treatment of the shallow semi-core In4d level whose binding energy is typically underestimated in DFT. The choice of the proper functionals is a further aspect for obtaining adequate band structure results. Typically, the calculated band gap values from DFT are too small and for InN even negative gaps were calculated. Both groups have achieved a correct determination of the band gap energy, by extensive studies either by using the HSE03 functional [86] or using modified pseudopotentials [87].

An overall qualitative agreement is found for the occupied states between the theoretical and the experimental data presented here, which is also comparable to recently published measurements [83] (the peak notations in Fig. 3.12 are adopted from this publication). The measured width of the valence band is in between the values of the theoretical calculations as can be seen in the energetic location of the structures denoted S_I^{WZ} and P_{II}^{WZ} in Fig. 3.12. As quality indicator, the structure at -5.05 eV (denoted S_I^{WZ} in [83]) is much better pronounced in the UPS measurements. This is due to the better energy resolution and signal-to-noise ratio for these measurements compared to the XPS results. In contrast to the slightly overestimated width of the VB calculated using HSE03, the energetic position of the In4d level together with the N2s contribution is slightly lower if compared to the experimentally determined values, but it has to be mentioned that the comparison with the experiments is complicated since e.g. spin orbital splitting of the In4d level is too complex to be implemented in the DFT calculations [88]. However, this effect has a strong influence on the actual peak shape as visible in the He II spectrum, where the contributions from the

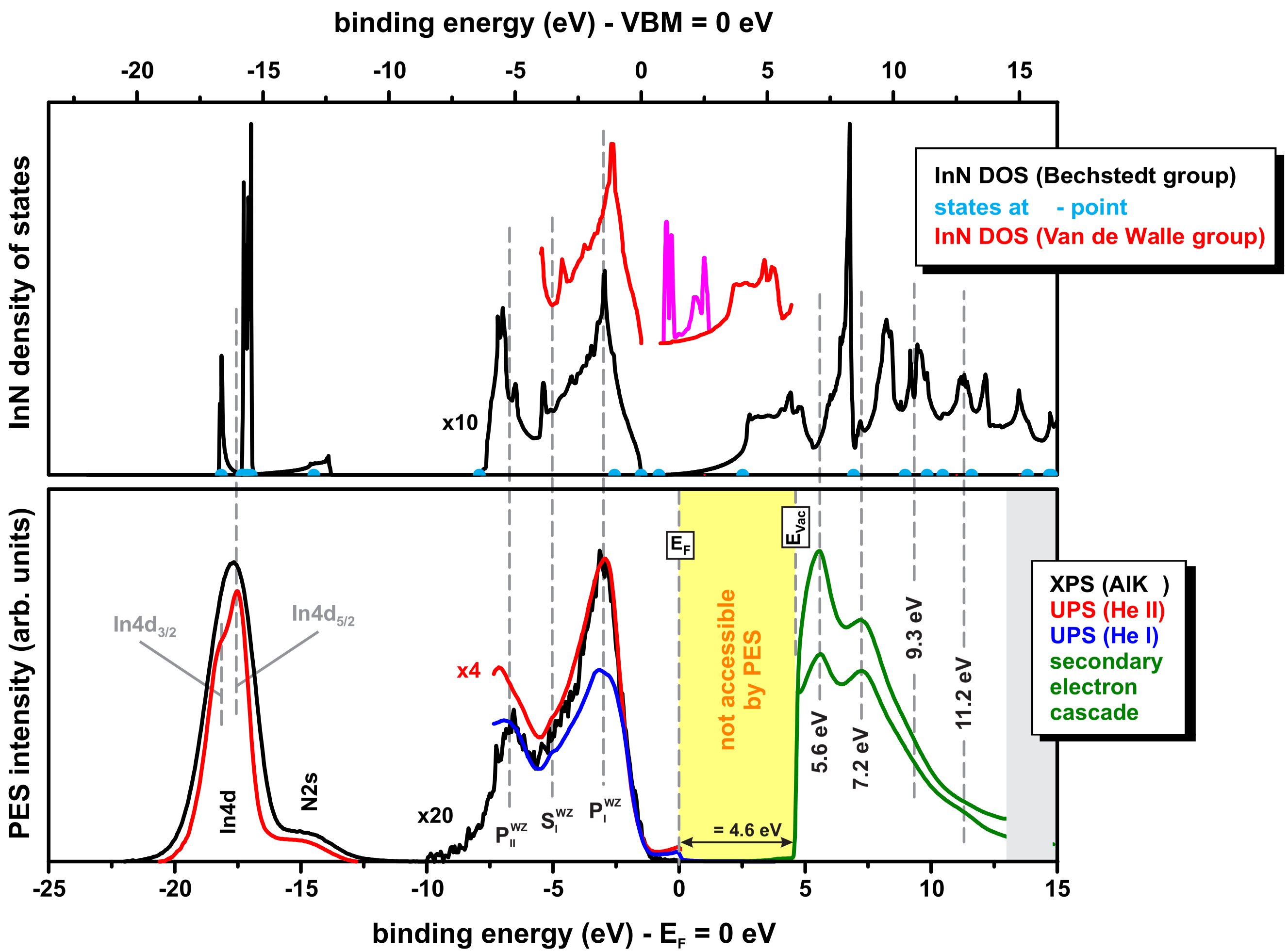

Fig. 3.12: Comparison of the InN density of occupied and unoccupied states between available DFT calculations (from the groups of F. Bechstedt [83] and C.G. Van de Walle [61]) and the results of photoemission spectroscopy. For the signatures of the In4d level and the valence band distribution, a Shirley-type background has been subtracted from the measured spectra.

$In4d_{3/2}$ and $In4d_{5/2}$ electrons are clearly separated.
The comparison of the calculated unoccupied electron states is more complicated, since the structures in the secondary electron signal are partially only visible as weak shoulders. Nevertheless, features with an energy of 5.6 eV, 7.2 eV, 9.3 eV and 11.2 eV above E_F could be identified in the measurement. These states do not agree very well with the position of the electronic states in the above plotted theoretical data in Fig. 3.12. A direct comparison is difficult, since the aspects of not detecting all electron states from the whole Brillouin zone plays an important role in that case. Therefore, the calculated energy states at the Γ-point are included in addition. It seems that a qualitative agreement could be achieved if one regards the states in the measurement to be shifted to higher energy values by about 1 eV. A comparable shift between the theoretical data and experimental results was also found in XAS/XES experiments and was there assigned to final state effects, such as the measured electron is bound in an exciton [85]. Final state relaxation effects due to the formation of core-holes can indeed cause a shift of the measured energy values of core electrons in PES. However, for the process of scattering of slow electrons into unoccupied states above E_{Vac}, such a strong shift is not expected. Since possible explanations are only speculative, it has to be stated that the difference between the calculated DOS of unoccupied states and the measurements from photon-induced secondary electron emission are not well understood at the moment, but matter of further investigations.

3.6.2 InN(0001)-(2×2) and -($\sqrt{3} \times \sqrt{3}$)R30° surface states

Adequate procedures to prepare well ordered and stoichiometric InN surfaces are rather rare. Most of the studies of the InN electronic structure are performed on samples with a (1×1) diffraction pattern. On the other hand, documented surface reconstructions of In-polarity InN are limited to *in-situ* RHEED measurements during growth. So far a ($\sqrt{3} \times \sqrt{3}$)R30° reconstruction has been reported to exist on InN(0001) [89, 52]. From ion scattering and PES measurements it was concluded that this reconstruction is related to the formation of metallic indium adlayers at the InN(0001) surface due to In-rich growth conditions. Indeed, the formation of In-adlayers has also been predicted by density functional theory calculations to be stable in that case [75, 72].
For the experiments performed on InN(0001), two surface reconstruction could be detected for specially adapted preparation conditions. Fig. 3.13 contains the RHEED patterns along the [11$\bar{2}$0] and [1$\bar{1}$00] directions for these two cases. The two top images represent the already mentioned (2×2) superstructure with half order streaks in both directions. This reconstruction was observed for the optimized In/N flux ratio at the following growth parameters: $p_{nitrogen} =$ 3×10^{-5} mbar, P = 350 W, $T_{growth} = 440$°C. For experiments that aimed the achievement of slightly higher growth rates, different growth conditions were chosen. Since the growth rate of the used MBE system is mainly restricted by the low nitrogen flux, the parameters of the plasma source were set to higher, but still stable conditions ($p_{nitrogen} = 7\times10^{-5}$ mbar, P = 450 W) in order to achieve the maximum flux of reactive nitrogen towards the surface. At the same time, a slightly higher growth temperature of 450°C had been chosen. The growth parameters were adjusted in order to obtain stoichiometric InN surfaces as judged from XPS and UPS measurements following the same routine

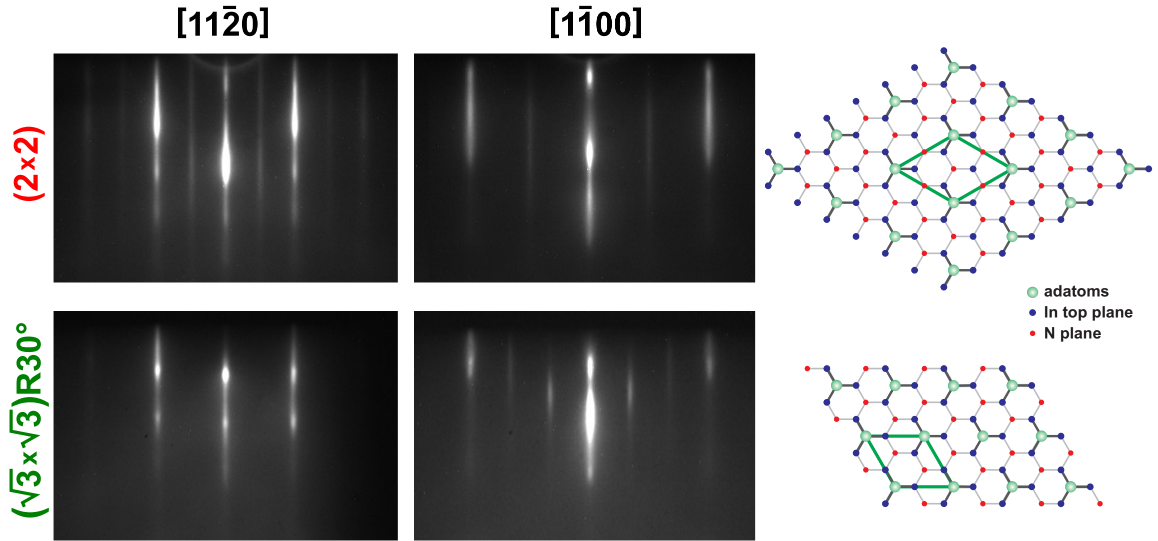

Fig. 3.13: RHEED patterns along the [11$\bar{2}$0] and [1$\bar{1}$00] direction and geometric atom arrangement of InN(0001) surfaces with (2×2) and ($\sqrt{3} \times \sqrt{3}$)R30° reconstruction. The adatoms (green) are shown for the case of being located at T4-sites.

as discussed in Sect. 3.4. In that way, a higher In-flux could be used, resulting in a higher but still fairly low growth rate of ~40 nm/h, which is also the maximum value that has been realized in comparison for the deposition of GaN in this system [90].
The RHEED patterns at the bottom of Fig. 3.13 represent the corresponding structure after optimization of the flux ratio under these conditions. The aspect that the extra third order streaks are only observed along the [1$\bar{1}$00] direction, defines the diffraction pattern to be caused by the existence of a ($\sqrt{3} \times \sqrt{3}$)R30° superstructure, which has already been reported at InN(0001) surfaces [89, 52]. On the other hand, the found (2×2) superstructure has not been reported to be experimentally observed so far.
Implementing DFT-calculations, D. Segev and C.G. Van de Walle have calculated the stable surface modifications of GaN and InN for different surface orientations. For In-polarity c-plane InN a (2×2) reconstruction is predicted to be the most stable configuration for a moderate In/N ratio. In this case the reconstruction is induced by In-adatoms located at T4 sites on top of the crystal lattice [72]. With increasing In flux, the stable configuration changes to the formation of a In-bilayer according to their calculations. Unfortunately, a ($\sqrt{3}\times\sqrt{3}$)R30° structure was not regarded in these DFT studies. However, since the amount of indium adatoms increases monotonously following the route (2×2) → ($\sqrt{3} \times \sqrt{3}$)R30° → In-bilayer, it could be possible that the ($\sqrt{3} \times \sqrt{3}$)R30° structure is formed under certain experimental conditions with medium In/N flux ratio.
The formation of surface superstructures is typically accompanied by the existence of distinct electronic states in the valence band as well as across the gap region of the material. Such surface states can have great influence on the surface and interface properties and are e.g. of importance for pinning the Fermi level. Since the sheet electron concentration of the quasi-free electrons at the dangling bonds of the adatoms can be as high as 10^{15} cm^{-2}, these states can strongly influence the properties of surfaces and interfaces. For example, the surface is thought to be the main source of electrons for the channel in high electron mobility

transistors. Possible electronic states originating from surface atoms can be found in the valence band spectra of the differently prepared surfaces. A comparison of the measured spectra obtained using He I radiation ($h\nu = 21.2\,\text{eV}$) is given in Fig. 3.14 for surfaces with a (2×2) or ($\sqrt{3} \times \sqrt{3}$)R30° reconstruction as well as after preparation at In-rich conditions. Most noticeably are the features found in the emission close to the Fermi level E_F. For all

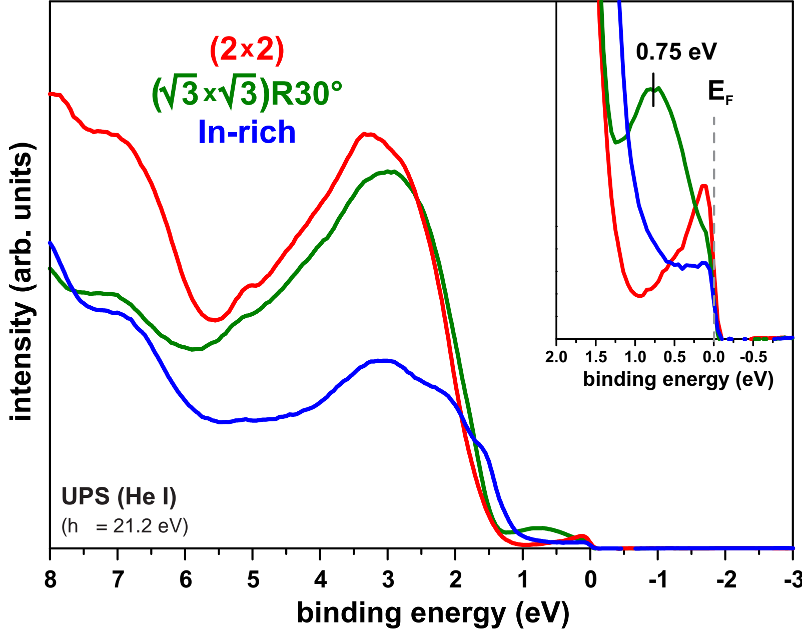

Fig. 3.14: Valence band photoemission spectra of InN samples with (2 × 2) and ($\sqrt{3} \times \sqrt{3}$)R30° surface reconstruction as well as indium-rich grown InN measured using He I ($h\nu = 21.2\,\text{eV}$) radiation. The inset shows a magnification of the emission close to the Fermi level.

three cases, a remarkable electron emission is found up to E_F. On the other hand it has to be pointed out that for far less surface sensitive PES measurements with AlKα, only in the case of In-rich growth conditions, a signal is detected up to E_F (see Fig. 3.7). For the other two cases, which have been prepared under stoichiometric conditions, the emission breaks down at the valence band edge. This finding is also in contrast to published data on AHC cleaned InN surfaces, where a strong signal from emission up to the Fermi level is discussed as the existence of indium adlayers at the surface [52]. Possibly, the accumulation of metallic indium in that case might come from the atomic hydrogen etching itself. Nevertheless, in the case of the indium-induced (2×2) and ($\sqrt{3} \times \sqrt{3}$)R30° reconstructions discussed here, an excess of metallic indium, forming several In-layers, can be excluded.

For samples with (2×2) superstructure, an interesting feature is found in the UPS measurement. The typical valence band distribution is found for all InN samples with a VBM at 1.55 eV (extrapolated from the XPS measurements). The signal drops strongly at the valence band edge and exhibits a strong rise into a peak close to the Fermi edge. This distribution of the density of states is unusual and is an indication for the existence of a surface state directly located at E_F. In contrast, for In-rich surfaces, a shift of the VBM by $\sim 0.25\,\text{eV}$ is found, but the spectrum is flat when approaching E_F.

These experimental results can be directly compared to the available DFT-data. The calculated DOS of bulk and surface states for the predicted stable conditions of a (2×2) structure

for moderate In/N ratio and the In-bilayer configuration for In-rich conditions are presented in Fig. 3.15. In the case of the (2×2)In_{T4} structure, the bonds between the In adatoms and the three surface atoms result in the existence of occupied states inside the conduction band that pin the Fermi level ∼0.6 eV above the CBM according to the calculations. This behavior was predicted to be one microscopic origin of the intrinsic electron accumulation at InN(0001) surfaces [61, 62]. The dangling bond of the In adatoms result in unoccupied states at even higher energy inside the conduction band (see Fig. 3.15). In contrast, for the

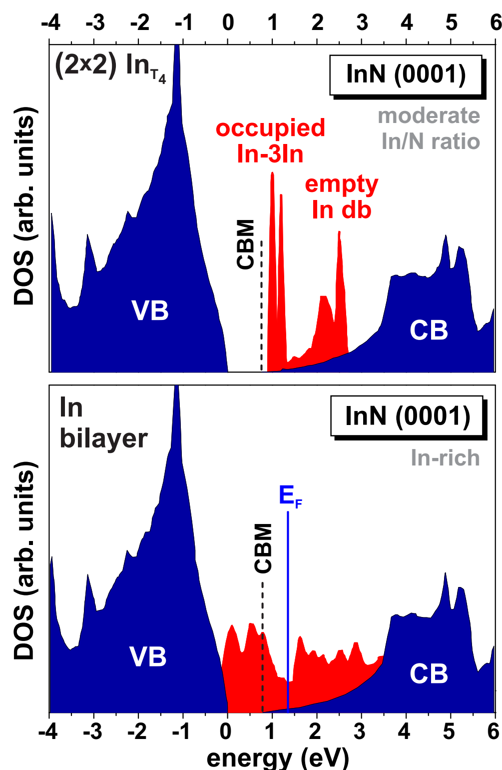

Fig. 3.15: Bulk and surface density of states for InN(0001) with an indium-induced (2×2) reconstruction (top) and in In-bilayer configuration (bottom) calculated using density functional theory (data from D. Segev and C.G. Van de Walle [61]).

existence of an In-bilayer at the surface, no sharp surface state is predicted. In this case the In-In bonding and dangling-bond strongly interact, leading to a large energy dispersion within the band gap. This is reflected in the DOS shown at the bottom of Fig. 3.15. The cations in the bilayer form relatively strong metallic bonds within the plane and between the two adlayers, and the Fermi level is located at ∼0.7 eV above the CBM. Inspection of the charge density distribution for states around the Fermi level shows them to be localized on In-In bonds within the underlying In adlayer, with some admixture of dangling bonds on the upper adlayer [61, 62].

The qualitative statements from the theoretical calculations agree very well with the experimental results and can give a very good explanation for the observed differences upon growth at stoichiometric or In-rich conditions. However, a shift of ∼250 meV of the InN valence band and core level states towards the Fermi level was experimentally found for In-rich conditions, which is not predicted by the DFT-calculations.

For the experimentally observed $(\sqrt{3}\times\sqrt{3})$R30° reconstruction, distinct states are found at other energy values. As can bee seen in Fig. 3.14, a strong peak is detected 0.75 eV below E_F. For that case no theoretical calculations on surface states are available at present, but it is anticipated that the detected feature is most likely also related to the In-In bonds of the adatoms to the three In surface atoms. Due to the higher adatom density and different arrangement compared to the (2×2) structure, they might be slightly shifted in energy. There is a second feature around 1.6 eV visible as a slight shoulder in the spectrum (green) compared to the other cases. Whether this is caused by a second surface state or is rather related to the bulk valence band emission cannot be clarified at the moment. However, it is believed that the $(\sqrt{3}\times\sqrt{3})$R30° superstructure is directly formed on top of the last plane of indium atoms for the surface preparation used in this case. For the here presented results, the spectral signatures in all measured XPS and UPS spectra disagree with the proposed 3 layers of metallic indium forming the $(\sqrt{3}\times\sqrt{3})$R30° reconstruction, as has been suggested for AHC treated films [91].
Since the experimental results for the InN(0001) surfaces agree very well with the predictions from DFT-calculations, one important perspective has to be mentioned. Evidence for the existence of an electron accumulation layer at nonpolar surfaces [63, 64] has been already experimentally found, which is also predicted from theory for In-rich growth conditions. On the other hand, in the cases of m- or a-plane oriented InN films produced at moderate In/N ratio, there is a chance that occupied electron states are absent inside the conduction band and hence electron accumulation might not occur in this case according to theoretical predictions [61, 62]. Whether this aspect can also be experimentally confirmed will be the subject of upcoming studies in the near future. Nevertheless, this might be difficult since other donor-type electron states, preferably related to crystal imperfections or impurities can also act as electron source and can emit their electrons into the conduction band due to the unusual location of the branch point energy in InN [60].

3.6.3 Interaction of InN(0001) with oxygen

Besides the knowledge of the electronic properties of clean surfaces, changes upon interaction with other atoms and/or molecules are of great importance. Mainly, the initial stages of surface modification play the most important role. First experiments were initiated to study the oxidation of InN(0001) surfaces using well defined starting conditions. As-grown InN films were exposed to different amounts of molecular oxygen. Upon exposure to 250 L during *in-situ* measurements in the surface analysis chamber, only slight changes were detected. Therefore, a significantly higher oxygen exposure was realized by venting the load lock chamber with pure oxygen while the sample was stored therein. Fig. 3.16 summarizes the results of the characterization of the valence band states upon interaction with O_2. Two structures appear in the valence band at 5.2 and 10.3 eV. This supports the interpretation of the results discussed in an earlier publication [65], where the spectral features could not be separated into oxygen states and hydrocarbon related structures. Hence, impurity-free preconditions allow a doubtless assignment of these features to oxygen adsorbates. As will be shown in the next chapter, the same adsorbate-induced states are found for the interaction of indium oxide surfaces with oxygen-containing molecules, such as O_2, O_3 and H_2O.

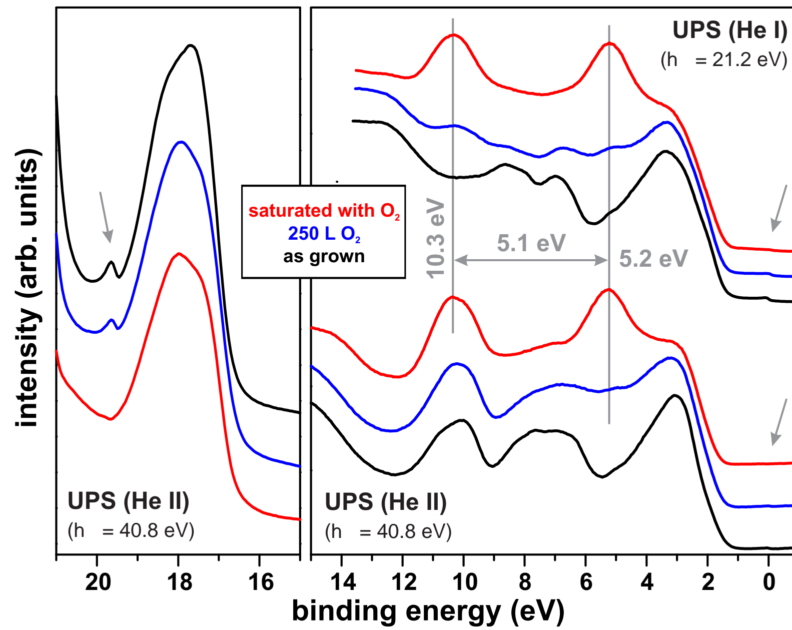

Fig. 3.16: Changes in valence band spectra of InN(0001) upon interaction with O_2. The measurements were performed using He I and He II radiation.

It is believed that the adsorption of oxygen takes place by a dissociation of the O_2 molecule and bonding of atomic oxygen at indium atoms.

Theoretical studies on the energy dependence of different adsorption sites are rarely reported. For the InN(000$\bar{1}$) surface, calculations predict the T_4 site to be the most stable for adsorption of oxygen or carbon [92]. Unfortunately, no reports can be found for In-polarity InN.

As a second aspect, exposure of the clean InN surfaces to oxygen leads to the vanishing of the emission due to the surface states close to the Fermi edge as well as the surface reconstruction. Hence, the initial adsorption of oxygen atoms is linked to the reaction at the In-adatoms. Surprisingly, the interaction with oxygen has only minor influence on the energetic position of the valence band maximum and the core level states as well as the work function of the sample (ϕ increases by 0.1 eV). Furthermore only a minor influence of the interaction with O_2 on the core levels is detected.

Finally it can be stated, that the sample quality achieved is suitable for surface reaction studies which have been preliminary demonstrated for the case of oxygen interaction. Possible further measurements will address the interaction with other oxygen-containing molecules (for example water) or organic molecules as well as alkali metals. Of further relevance will be studies on the electronic band alignment properties of InN interfaces with possible gate materials for transistor applications, e.g. the In_2O_3/InN interface.

In further measurements, a strong oxidation by reaction of the InN surfaces with ozone was observed. Investigation of the surfaces properties on InN samples that were exposed to O_3 has so far only been possible on contaminated samples. However, the formation of a thin indium oxide layer could be detected which results in the variation of the electron transport properties in the material. The details and results of these experiments are published in [93] and will not be discussed in detail here.

In summary, implementation of *in-situ* surface analyses of InN thin films has been realized for the first time. Although, the thermodynamic properties of the In-N system are not very suitable for MBE growth and subsequent surface analysis, since better crystalline quality is typically achieved at In-rich conditions, a sufficient sample quality of the thin InN films was attained. The influences of different growth parameters on the surface composition and possible excess atoms was studied without having disturbing contribution from exposure of the samples to ambient conditions. By the successful preparation of stoichiometric and contamination-free surfaces, it was possible to study the electronic properties of InN including the consequences of stable surface reconstructions on electronic states above the valence band maximum. Surface states were found to exist for the observed (2×2) and $(\sqrt{3} \times \sqrt{3})R30°$ reconstructions of In-polarity InN films. From this starting base, many interesting aspects can be studied in future experiments. For example, the interaction with reactive species has been demonstrated by preliminary oxidation experiments.
Nevertheless, it is important to note that the interpretation of the experimental data is only possible with a strong support from theoretical calculations. So far, only a few works on pure InN surfaces are available and especially data for the interaction with adsorbates is missing.

Chapter 4

Surface properties and ozone interaction of indium oxide films grown by MOCVD

4.1 Indium oxide - an ozone sensitive material at room temperature

Metal oxide films are widely used for sensor applications to measure the concentration of environmental and hazardous gases. Both, oxidizing and reducing species can be detected depending on the properties of the used material and the actual operation conditions [94]. One important class of these sensors is based on the variation of the film conductivity upon interaction with atoms or molecules. Prominent representatives of this group of materials are transparent conductive oxides (TCOs) such as SnO_2, ZnO, TiO_2 and In_2O_3, which belong to the wide band gap materials. Typically the changes in conductivity upon oxidation or reduction can have two different contributions: *i)* change of the bulk carrier concentration by formation or annihilation of intrinsic dopants and *ii)* variation of the surface band bending induced by chemisorption of surface species or reaction of gases with adsorbed species [95]. The surface band bending changes result in the alteration of the charge carrier profile at the surface and induce the formation of energy barriers at grain boundaries in polycrystalline materials. The complex connections between material properties, device related technological aspects and the gas interaction processes are composed in a comprehensive overview article on metal oxide based gas sensors [96].
The capability of indium oxide films to detect ozone has already been reported in the 80's [94]. Since then, many different approaches have been followed to tailor the material properties by different synthesis methods, such as RF sputtering or sol-gel processes to improve the sensitivity of the films towards O_3 [97, 98, 99, 100]. Of special importance for this purpose is the realization of defect-rich In_2O_{3-x} films with a high concentration of oxygen vacancies. It has been found that especially indium oxide nanoparticles and nanowires possess a very high sensitivity for the detection of ozone.
Most solid gas sensors require temperatures between 200 and 600°C in order to reach their optimal performance. This is normally realized by passive heating of the sensor device or by

current induced self-heating during operation. Both principles rely on a relatively high energy consumption since electric power is required for heating. On the other hand, In_2O_{3-x} films can be implemented in ozone sensors operating at room temperature [98, 100]. This makes indium oxide based gas sensors very promising for the realization of low energy-consumption and low-cost devices. The regeneration of the material after oxidation is in this case not engendered by thermal desorption, but realized by illumination of the active sensor area by UV light from a LED. The straightforward layout of such a sensor structure is demonstrated in Fig. 4.1. The O_3 concentration is determined via measurement of the increase in film resistance upon ozone-induced oxidation of the In_2O_{3-x} layer. For thin

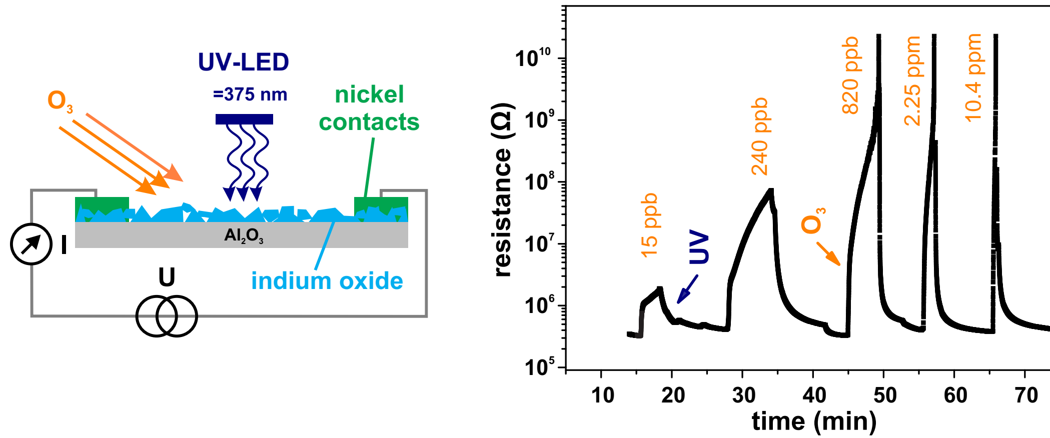

Fig. 4.1: Room temperature ozone detectors based on polycrystalline indium oxide. (left image: schematic of the sensor layout, right image: dependence of the film resistance on the ozone concentration and illumination with UV light for a ∼80 nm nanoparticle layer grown at a substrate temperature of 200°C (data from Ch. Y. Wang [100]).

nanocrystalline indium oxide films prepared by MOCVD, ozone concentrations as low as 15 parts per billion (ppb) can be detected [100]. The signal response at room temperature to different concentrations of O_3 is exemplarily depicted in the right part of Fig. 4.1. A device sensitivity $(R_{ozone}/R_{UV}) > 10^5$ could be realized and the response time was as low as 1 s for 10 nm thick films. The film resistance can be reproducibly regenerated by the illumination with UV light. This is one key aspect for practical use in reliable and long-term stable ozone sensors. Furthermore, the operation at room temperature assures a low interference from reducing gases and hence low cross-sensitivity. Nevertheless, for operation temperatures above 150°C, In_2O_{3-x} films have been found to be also sensitive to other gases such as H_2, NO_x, CO, NH_3, CH_4 and C_2H_5OH [101, 102, 103, 104, 105].
The surface properties of different metal oxides as well as adsorption of many atomic and molecular reactive species have already been extensively studied during the last decades [106, 107]. Among the variety of the many functional metal oxides, TiO_2 is one of the in most detail investigated material [108]. It is generally accepted that TiO_2 is more bulk sensitive, i.e. it exhibits conductivity changes due to variations in intrinsic dopants as a consequence of the formation of oxygen vacancies and Ti interstitials, while SnO_2 and ZnO are considered as surface sensitive materials. In the case of surface sensitive oxides for the detection of oxidizing and reducing gases, the adsorption of charged surface oxygen species plays a central role [95]. Most of the known surface investigations of In_2O_3 have

concentrated on tin-doped material with a very high electron concentration. However, in the case of pure indium oxide, without additional dopants, available information on the surface electronic structure investigated by photoelectron spectroscopy are restricted to a few publications. First studies on the interaction with adsorbates like O_3, O_2, H_2O and CO are reported [109, 110, 111, 97].
In a collaboration aiming to develop inexpensive integrated ozone sensors based on indium oxide thin films prepared by MOCVD, photoelectron spectroscopy analyses were performed in order to characterize the surface chemical and electronic properties of these films depending on different preparation conditions. The underlying sensor principle based on ozone oxidation and UV reduction is investigated by O_3 adsorption/desorption experiments and possible disturbing influences by contact to ambient species, such as oxygen and water are analyzed.

4.2 Valence band structure and electronic properties of different In_2O_3 polymorphs

Indium oxide films or particles prepared by different preparation methods, such as physical or chemical vapor deposition or by chemical synthesis, are commonly formed in the thermodynamic stable body-centered cubic crystal structure (bcc-In_2O_3, a = 10.118 Å) in bixbyite configuration. This structure has been reported to exist in two configurations: SG199 and SG206 with different space groups $I2_13$ and $Ia\bar{3}$, respectively [112]. However, density functional theory (DFT) calculations predict only the SG206 to be a stable modification [113, 114]. In bixbyite In_2O_3, the primitive unit cell consists of 40 atoms corresponding to 8 In_2O_3 units. Recently, it has been found that corundum type In_2O_3, which is normally specified to be the high pressure phase, can be grown in a MOCVD reactor at fairly low pressure and temperature [115]. This polymorph (SG167, space group $R\bar{3}c$) has a rhombohedral unit cell (rh-In_2O_3, a = 5.478 Å, c = 14.51 Å) where the In atoms are surrounded by oxygen in a trigonal biprism [114].
While both types are chemically identical, it has been experimentally observed that rhombohedral and cubic In_2O_3 thin films deposited by MOCVD exhibit distinct differences in their optical properties. From the extrapolation of the absorption edge, typically an optical band gap of ∼ 3.6 eV is extracted for bcc-In_2O_3 while the onset of absorption for rh-In_2O_3 was found at much lower energies of ∼ 3.0 eV [115]. Although the band gap of indium oxide was believed to lie between 3.6 and 3.7 eV for many years, indications for the existence of an indirect gap around 2.1 eV were reported [116]. On the other hand, recent experimental and theoretical studies state that the band gap of indium oxide is of direct type, but the commonly accepted band gap value of bcc-In_2O_3 is too high and suggest a value in the range of 2.9 - 3.1 eV [114, 117]. This uncertainty has also some influence upon the models that describe the band alignment at In_2O_3 surfaces. Hence, the commonly accepted picture of the existence of a depletion layer at the indium oxide surface has to be questioned. This aspect will be examined in detail in the following analysis of the valence band measurements.
The investigation of the surface chemical properties and electronic structure of In_2O_3 films

with bcc and rhombohedral crystal structure has been performed on three samples (see Fig. 4.2) that have been prepared by MOCVD on different substrates using tailored deposition parameters. All samples were grown by Ch. Y. Wang from the Nanotechnology group at TU Ilmenau in a horizontal MOCVD reactor (AIXTRON 200) using trimethylindium ($In(CH_3)_3$) and H_2O as precursors and N_2 as carrier gas. A phase diagram for MOCVD growth of indium oxide including the dependence of the crystal structure on the growth conditions such as substrate temperature and $In(CH_3)_3$ flow rate is documented in [115].

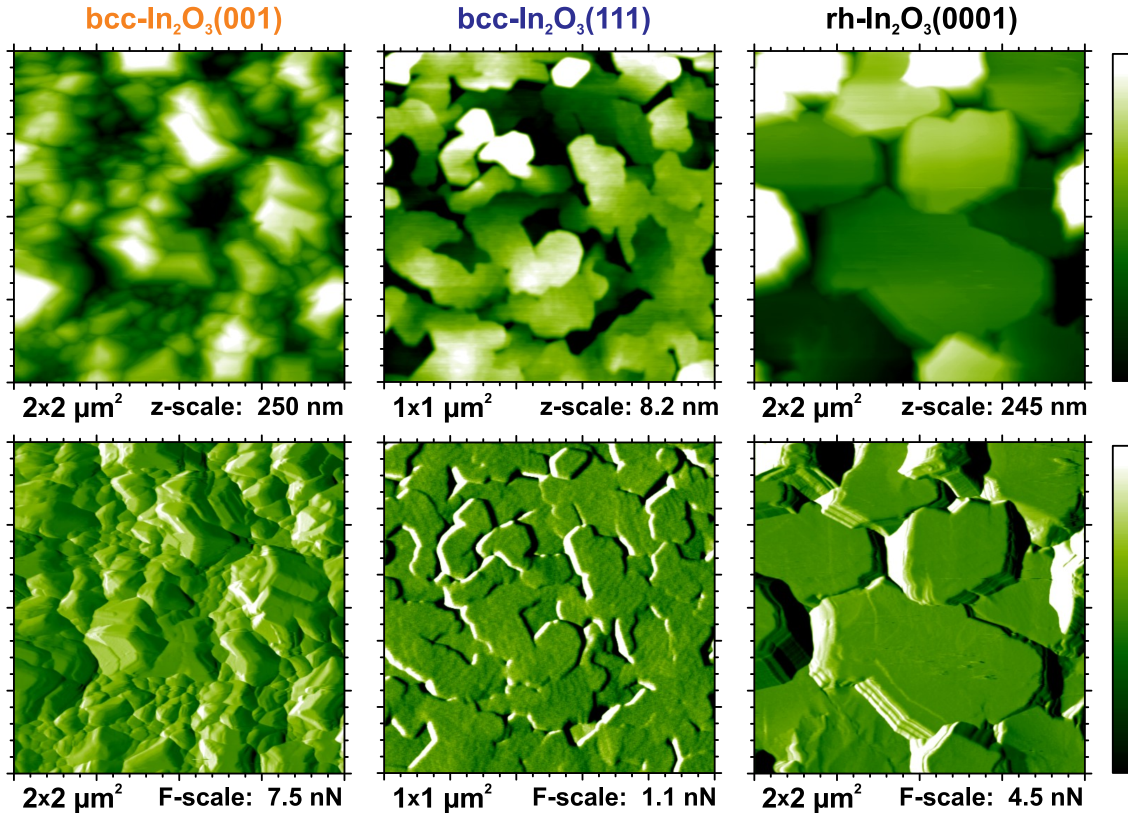

Fig. 4.2: Morphology of the bcc-In_2O_3(001), bcc-In_2O_3(111) and rh-In_2O_3(0001) samples measured using contact mode atomic force microscopy. The upper images represent the topography signal while the images at the bottom represent the force signal.

The first sample was deposited on Al_2O_3(0001) at a growth temperature of 600°C, after growth of a thin nucleation layer at 300°C. Under these conditions, a highly textured bcc-In_2O_3 film is formed with the (001) orientation aligned to the wafer normal. The growth of single crystalline cubic indium oxide with (111) orientation has been realized by deposition at 400°C on a InN/GaN/Al_2O_3(0001) template [118]. The oxide thickness of this second sample is $\sim$55 nm. These two bixbyite bcc-In_2O_3 samples are compared to a corundum rh-In_2O_3 film that has been synthesized also on sapphire. For obtaining single crystalline rh-In_2O_3 using MOCVD, the deposition parameters have to be modified to a higher substrate temperature and a very low $In(CH_3)_3$ flow rate. The investigated sample consists of a $\sim$150 nm thick nucleation layer grown at 600°C followed by the deposition of a $\sim 1\,\mu m$ thick indium oxide film at 300°C. Under these experimental conditions almost pure rhombohedral indium oxide can be produced with a negligible proportion of the cubic phase present

in the films (in XRD scans the intensity ratio $I_{rh(0006)}/I_{bcc(222)}$ was found to be ~1200) [119]. The electrical properties of the indium oxide films have been characterized by Hall measurements. The electron concentration was determined to be between 5×10^{18} cm^{-3} and 1×10^{19} cm^{-3} for all samples that have been grown between 400°C and 600°C.

The different sample morphology, as characterized by contact mode AFM measurements, is presented in Fig. 4.2. All three indium oxide films consist of crystallites with different average diameter. While the rough surface of the bcc-In_2O_3(001) is characterized by rectangular based islands and pyramids which appear to be {111} facetted, the crystallites at the bcc-In_2O_3(111) surface exhibit flat terraces and have a lateral dimension of ~100 - 200 nm. In this case, existing surface steps at the crystallite top side are clearly visible in the force signal scan. The surface of the rh-In_2O_3(0001) sample consists of the largest crystallites with a mean diameter of ~1 μm. Although each island appears to be very flat, this surface is fairly ragged exhibiting steep trenches between each crystallite. Besides the different growth conditions it has to be mentioned that the differences in sample morphology is of course also dependent on the different growth time and film thickness of all reference samples. Nevertheless, for the performed characterization by XPS and UPS, this parameter is not of importance, since all films are thick enough to ensure that no substrate related signal will affect the analysis of the surface properties. On the other hand, adsorbed molecules on the surface disturb an accurate interpretation of the electronic properties. Therefore special attention has been paid to reduce the amount of time which the samples have been exposed to ambient conditions before surface characterization. Whenever possible, the wafers were, after removal from the growth reactor, immediately cut into 8×6 mm^2 large pieces, mounted onto a sample holder and introduced into the load lock chamber of the UHV surface analysis system. The remaining low amount of contaminants have been removed by careful Ar^+ ion bombardment or annealing up to 250°C in 1×10^{-7} mbar oxygen environment.

As already pointed out, the chemical structure of both polymorphs is identical and, as a

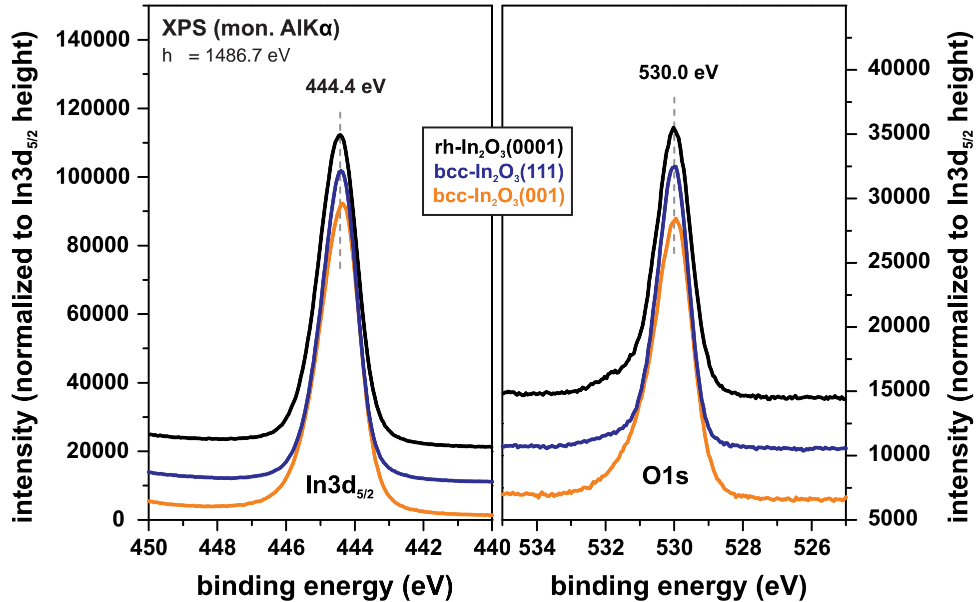

Fig. 4.3: $In3d_{5/2}$ and O1s core level spectra of bcc-In_2O_3(001), bcc-In_2O_3(111) and rh-In_2O_3(0001) measured using monochromated AlKα radiation ($h\nu = 1486.7$ eV).

consequence, no differences in the core level emission are expected from XPS measurements. Fig. 4.3 shows a comparison of the measured In3d$_{5/2}$ and O1s core level spectra which prove that there is no evidence for any difference in the local chemical environment or surface composition. All three samples exhibit similar spectra with symmetrical core levels and a peak maximum of the In3d$_{5/2}$ and O1s emission at 444.4 eV and 530.0 eV, respectively, which can be ascribed to the indium and oxygen atoms in the crystal lattice. It has to be mentioned that neither C1s related emission (not shown) nor the typical adsorbate-related structure in the O1s signal around 532 eV were detected. This is a prerequisite for the analysis of the valence band photoemission spectra shown in Fig. 4.4, especially when UV radiation is used for the generation of electrons. The spectra represent the valence electron emission measured using different excitation sources for the generation of He I, He II and monochromated AlKα radiation, respectively.

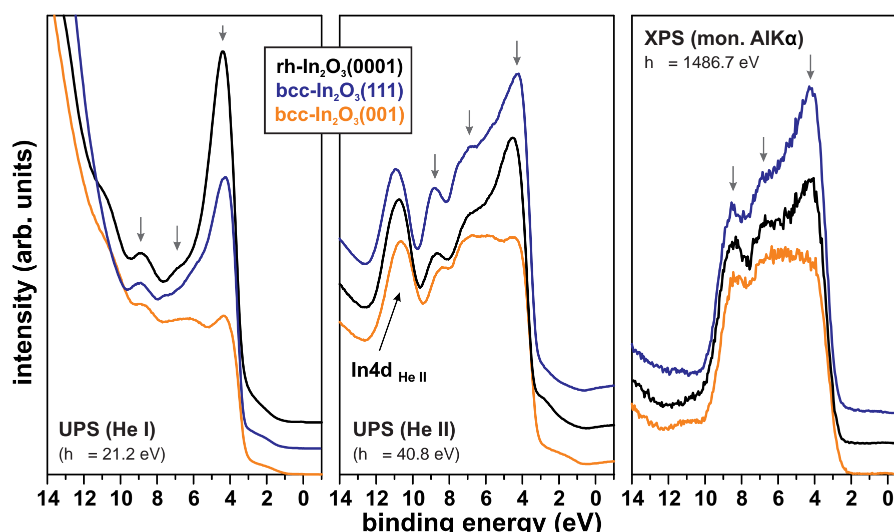

Fig. 4.4: Valence band photoelectron spectra of bcc-In_2O_3(001), bcc-In_2O_3(111) and rh-In_2O_3(0001) measured using He I ($h\nu = 21.2$ eV), He II ($h\nu = 40.8$ eV) and monochromated AlKα ($h\nu = 1486.7$ eV) radiation.

Comparing the three different samples, it has to be mentioned that the characteristic emission features agree well with the results of earlier studies on the surface electronic properties of In_2O_3 [109] and DFT calculations of the bulk DOS [120, 114]. According to these works, the valence band features are mainly comprised of O2p states. Pronounced structures in the VB are found at 4.4, 6.8 and 8.7 eV (indicated by arrows in Fig. 4.4). The (001)-oriented sample exhibits a fairly flat valence band, while in the other two cases, the emission at the valence band onset leads to a sharp peak, comparable to the calculated DOS [120, 114]. This observation is believed to be related to orientational effects in the photoemission yield rather than being caused by different chemical bonds, since no modification of the chemical composition was found in the XPS measurements and a similar flat valence band distribution has already been reported for d.c. sputter deposited films [121].

For all three investigated indium oxide films, the shallow In4d core level is found at a binding energy of 18.2 eV (not shown here). Furthermore, the work function was determined to be $\sim$4.2 eV and the extrapolation of the valence band trailing edge gives a VBM of 3.1 eV.

The energetic position of the valence band maximum with respect to the Fermi level has also been reported in earlier works to lie around 3 eV [109, 122]. As already explained for the InN measurements, the measured value E_F - VBM is mainly determined by two parameters: *i)* the energetic position of the bulk Fermi level and *ii)* the band bending at the surface. Since In_2O_3 is a degenerate semiconductor, the Fermi level is located inside the conduction band and the occupation of the conduction states is dependent on the carrier concentration inside the film. According to recent band structure calculations, for an electron concentration in the range between $5{\times}10^{18}$ cm^{-3} and $1{\times}10^{19}$ cm^{-3}, which is present in the films investigated here, the bulk Fermi level is located $\sim$50 - 70 meV above the conduction band minimum [114]. Under the assumption of a band gap of 3.6 eV, photoelectron spectroscopy indicates a strong upward band bending, as discussed in [123]. However, this model does not agree very well with the observed variation of the conductivity of these films upon oxidation and reduction of indium oxide sensor surfaces. This discrepancy led, for example, to the proposal of a modified band gap at reduced In_2O_3 surfaces [111]. The recently discussed lower band gap value of 2.9 - 3.1 eV would describe the electrical characteristics of the films much better. The band alignment at the In_2O_3 surface for these three different band gap values is schematically plotted in Fig. 4.5. In contrast to the strong upward band bending in the case of $E_g = 3.6$ eV, for the experimentally determined distance between E_F and the surface VBM, almost flat band conditions would result for a band gap around 3 eV. Depending on the exact value, slight upward or downward band bending of about 100 meV would result. A final picture cannot be developed for the band alignment at the In_2O_3 surface at the moment since too many uncertainties are still existing in the experimental results as well as in the theoretical calculations. Nevertheless, a scenario with almost flat band conditions is more favorable.

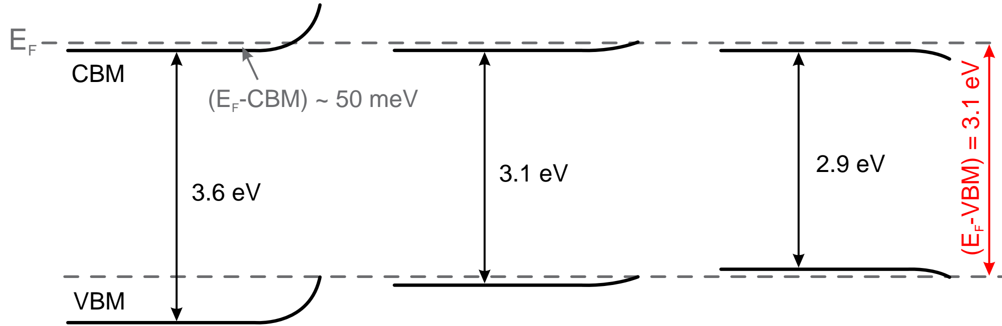

Fig. 4.5: Model of the band alignment at In_2O_3 surface depending on different band gap energies of 3.6, 3.1 or 2.9 eV. The left scenario corresponds to the common picture of strong upward band bending [123], while in the case that the real band gap is around 3 eV [114, 117], an almost flat band distribution would result.

The characteristics of the three different stoichiometric and crystalline indium oxide samples presented above are the reference for a subsequent analysis of the surface properties of nanocrystalline In_2O_{3-x} films prepared by MOCVD at very low temperatures discussed in the next section. As will be shown below, the high sensitivity of these films towards ozone is related to differences in the indium oxide crystallite size as well as in the surface composition of the material.

4.3 Non-stoichiometry and defect states in In_2O_3 films grown by MOCVD at low temperatures

Upon a detailed study of the ozone sensing characteristics of polycrystalline indium oxide thin films prepared by MOCVD, it was established that the ozone detection efficiency is strongly dependent on the growth temperature used. For films prepared at temperatures as low as 200°C, a sensitivity of up to 10^5 was observed for an ozone concentration of ~ 10 ppm and a remarkably low response time of ~ 1 s could be achieved for 10 nm thick films. By implementing these films into sensor devices, it was possible to reduce the detection limit to around 15 ppb O_3 [100]. The ozone sensitivity dependence of the indium oxide films is mainly caused by two reasons. First, there is a strong relation between the indium oxide particle size and the used deposition temperature. As demonstrated in Fig. 4.2, for growth temperatures above 400°C, the crystallites have an average diameter of a few hundred nm. Upon reducing the growth temperature, the particle size is strongly decreased, approaching a value of 7 - 8 nm around 200°C. The typical crystal structure of such an indium oxide film grown at 200°C (this type of sample is subsequently denoted "LT-InOx") is presented in Fig. 4.6. On the left side, a transmission electron micrograph of a LT-InOx/Al_2O_3 interface is shown, indicating the existence of a closed film of single crystallites with a diameter of

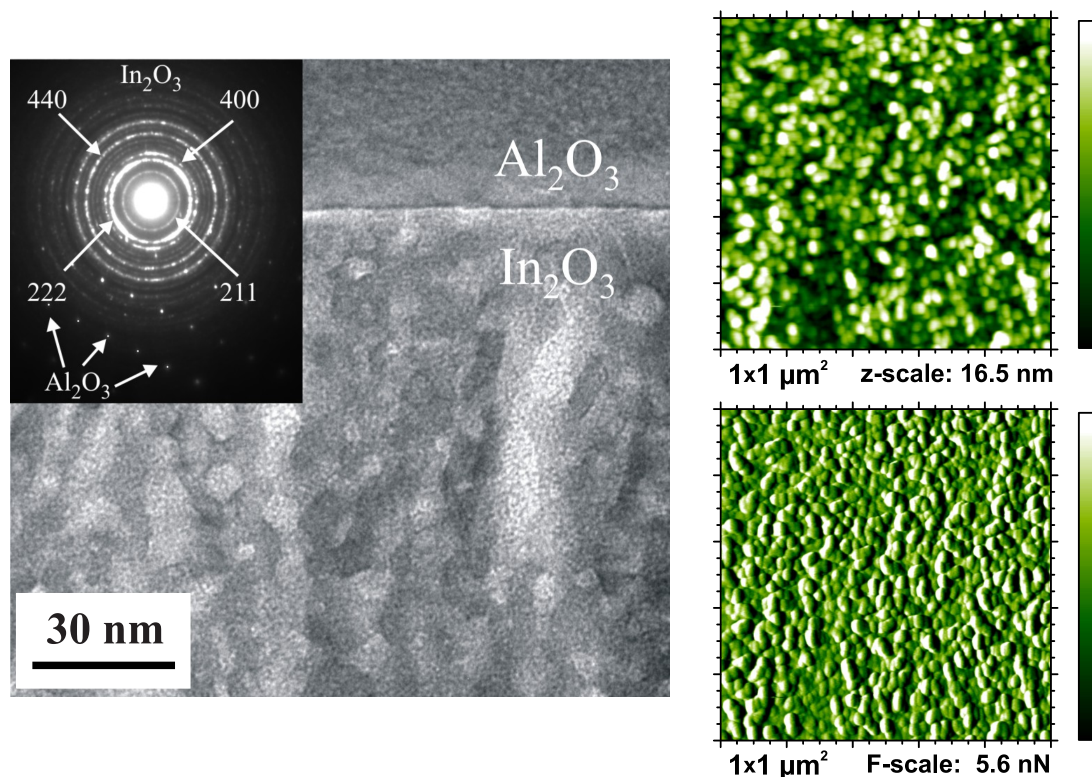

Fig. 4.6: Crystal structure and surface topography of nanocrystalline indium oxide grown by MOCVD at 200°C. Left picture: TEM (transmission electron microscopy) image and SAED (selected area electron diffraction) pattern (inset) of the nanoparticles [100]. The small grain size is also observed in contact AFM measurements (picture on the right).

less than 10 nm [100]. On the right side of the figure, corresponding atomic force micrographs are presented. Due to the low substrate temperature, the chemical reactions are inhibited, the adsorption/desorption ratio of molecules of the gas phase is strongly modified and especially the low diffusion rate of atoms and molecules at the surface of the formed nuclei leads to the formation of only small particles, while the resulting grain size at higher temperatures is much larger. The porous nanocrystalline character of these LT-InOx films is clearly visible and is one reason for the observed high ozone sensitivity. It is strongly enhanced by the fact that the active surface, where the reaction with ozone takes place, is strongly increased. However, as will be discussed in the following, the nanocrystalline structure of these LT-InOx films is not the only difference compared to conventional In_2O_3 films.

The surface stoichiometry of these films was characterized by X-ray photoelectron spectroscopy measurements. Differences in the chemical composition can be deduced from the comparison of results from LT-InOx samples with the measurements of conventional In_2O_3 films as presented in Figs. 4.7 and 4.8. All electron states shift by 0.2 eV towards higher

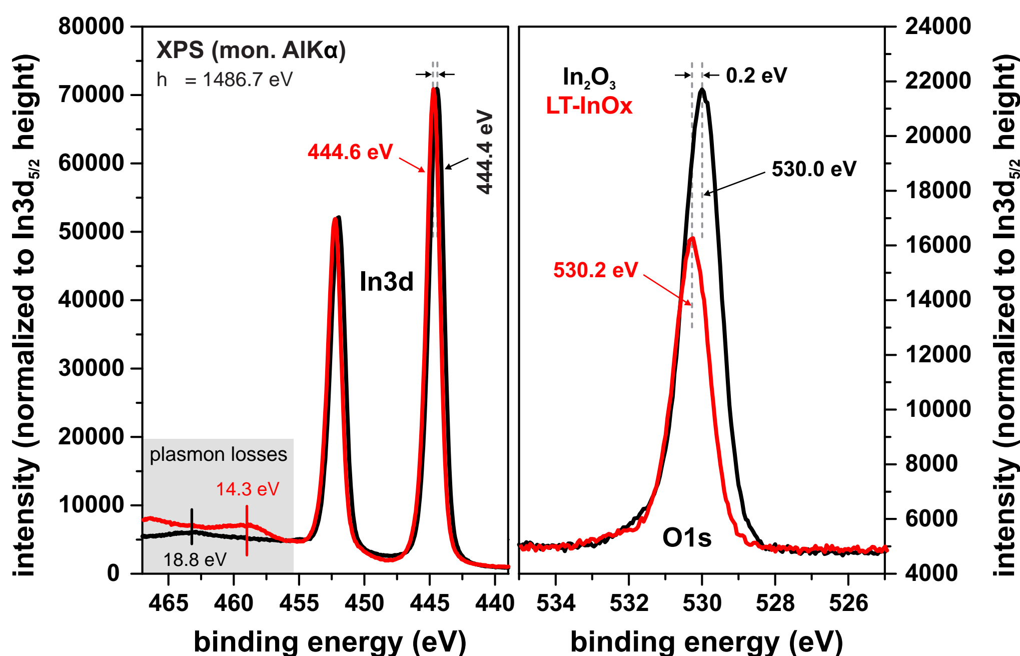

Fig. 4.7: Comparison of the In3d and O1s core level spectra between crystalline In_2O_3 grown above 400°C and nanocrystalline LT-InOx deposited at 200°C.

binding energy. An explanation for this observation will be discussed below together with the changes in the valence band emission. The most prominent difference of LT-InOx is the drastically reduced amount of oxygen at the surface compared to stoichiometric In_2O_3 films grown at higher temperatures. From analysis of the peak area ratio of the single electron core level contributions it was determined that the oxygen content is reduced to ∼67%, which corresponds to a 1:1 proportion of indium and oxygen at the surface. Therefore, it can be concluded that the very low deposition temperature leads to a highly oxygen-deficient and sub-stoichiometric material.

A similar result has been found for nanocrystalline indium oxide prepared by spray pyrol-

ysis [124]. In this publication, the authors explain the oxygen deficiency by the instability of certain oxygen bonds at the (100) surface which leads to a release of oxygen, forming an energetically stable lattice with oxygen vacancies. Hence, unsaturated In ions are expected to serve as the surface sites for the chemisorption of oxygen and water related species.
Further experimental evidence for the oxygen deficiency can be found in the location of the plasmon loss structure in the In3d signal. For In_2O_3, the loss structure is found at 18.8 eV, while for the LT-InOx films it is shifted to 14.3 eV (see Fig. 4.7). Enhanced excitation of surface plasmons it not believed to be the reason for this shift, but rather the differences in the In/O ratio. In comparison, for other indium compounds with 1:1 composition, the bulk plasmon energy is also found at lower values, for example at 15.6 eV for InN [50] and at 15.1 eV for InP [125].
It is anticipated that the used precursors, H_2O and trimethylindium ($In(CH_3)_3$), are not efficiently converted into In_2O_3 and CH_4 at these low growth temperatures, resulting in a high amount of missing oxygen. At the same time, intermediate cracking products might be formed. This presumption is supported by the observation that a huge amount of carbon ($\sim$ 25 at. %) is found at the surface of the LT-InOx films after deposition. Fig. 4.8 contains a compilation of C1s spectra from different indium oxide films in order to distinguish between chemical states that are formed during growth and contamination related features which result from contact to ambient conditions. The gray spectrum represents the case of

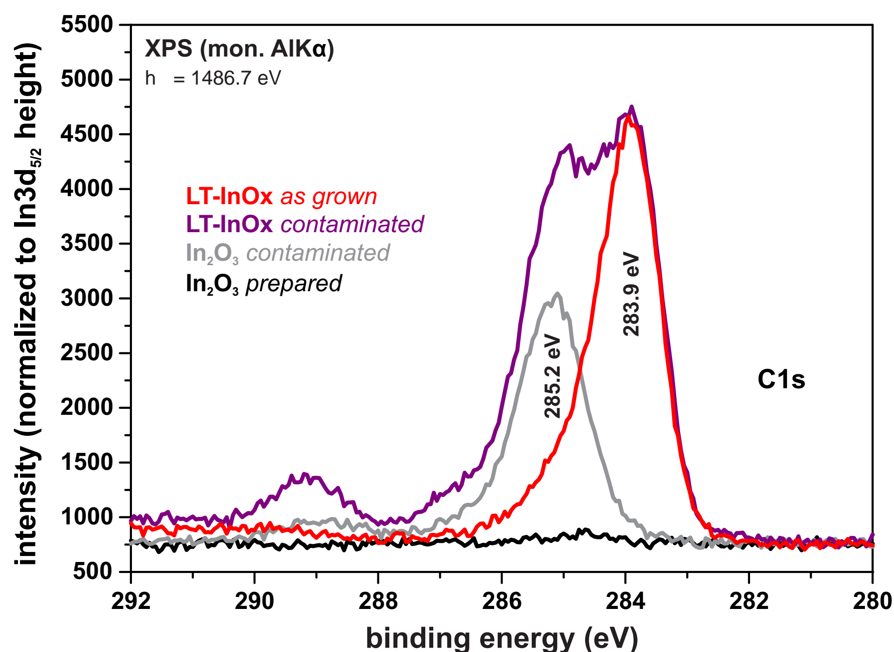

Fig. 4.8: Carbon impurities at In_2O_3 surfaces depending on preparation conditions.

a conventional In_2O_3 sample that has been stored in air with the typical carbon impurities. The features observed at 285.2 eV and around 289 eV are typically found for organic hydrocarbon adsorbates [126] and correspond to C–CH_x and C=O bonds, respectively. For the as-grown LT-InOx films (red spectrum), these structures are absent, but instead a highly asymmetric peak is detected with a maximum intensity at 283.9 eV. The proof that the features at 285.2 eV and $\sim$ 289 eV are due to contaminants is made by the comparison with the

C1s signal of a In_2O_3 film after surface cleaning by gentle Ar^+ sputtering (black spectrum) and a LT-InOx film that has been stored for about one week in air (purple spectrum). In the latter case, the same adsorbate-related structures as for the contaminated In_2O_3 films are detected, but the structure at 283.9 eV is present as well. Therefore, one would expect that the spectral feature at 283.9 eV is caused by incorporated cracking products of the $In(CH_3)_3$ precursor during growth at temperatures around 200°C. The reaction balance for the formation of In_2O_3 from TMI and H_2O is

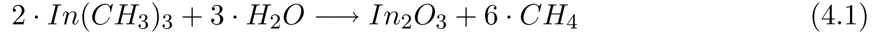

$$2 \cdot In(CH_3)_3 + 3 \cdot H_2O \longrightarrow In_2O_3 + 6 \cdot CH_4 \quad (4.1)$$

The decomposition of TMI typically takes place by a homolytic fission of the three In-C bonds following the pathway TMI → DMI → MMI. The cracking product monomethylindium (MMI - $InCH_3$) is reported to be relatively stable [127] and might be incorporated into the film at these low temperatures. However, a chemical analysis by interpreting the binding energy of this state is difficult since not much reference data is available. Unfortunately, no XPS analyses of In–C bonds are reported in the literature, but typically the binding energy of carbide compounds is 1 - 2 eV lower than the value of 283.9 eV [128], e.g. a C1s binding energy of 282.9 eV was determined for clean SiC(0001) surfaces using the same experimental setup. Nevertheless, possible In-C_xH_y components could be an explanation for this chemical state and therefore it is concluded that the very low temperature of 200°C results in the incorporation of weakly bound carbon material during growth that can be removed by UV exposure of the samples as will be shown below. Since the samples exhibit so many active sites because a high amount of oxygen is missing in the material, it is anticipated that the carbon related species are weakly bound and saturate the active In sites at the surface of the single grains. It is worth further mentioning that additional investigations are currently being performed to identify the molecular structure of the incorporated species. For this purpose XRD and IR-spectroscopy examinations are on the way. Preliminary results from XRD measurements reveal additional diffraction peaks for as-deposited LT-InOx films that disappear upon UV illumination [129].

The comparison of the valence band structures of conventional In_2O_3 and LT-InOx films is shown in Fig. 4.9. While the valence band spectra of LT-InOx and In_2O_3, measured using X-ray radiation, are similar in shape except for the enhanced emission above the valence band edge that will be discussed on the next page, distinct differences were observed for the more surface sensitive measurements using ultra-violet radiation. In the case of LT-InOx, a strong peak is detected at ~ 9 eV which is attributed to the modified chemical composition at the surface of these single grains. Furthermore, a shift of the electron states by about 0.2 eV to higher binding energy is detected, resulting in a distance between VBM and E_F of 3.3 eV for the LT-InOx films. This increase in binding energy is also found for the In3d and O1s core levels (see Fig. 4.7) and can be explained by a shift of the Fermi level with respect to the occupied bands. Although not possible to be measured by Hall experiments, the internal electron concentration in these defect-rich films is believed to be higher compared to the crystalline material. An electron concentration of about 10^{20} cm^{-3} and the associated shift of the Fermi level inside the CB would explain the observed differences. Additionally, for the as-grown LT-InOx samples, a higher work function of 4.4 eV is typically measured ($\phi\,(In_2O_3) = 4.2$ eV). This observation is in contradiction to a simple conception that the Fermi level is only shifted inside the conduction band, which would result in a lower work

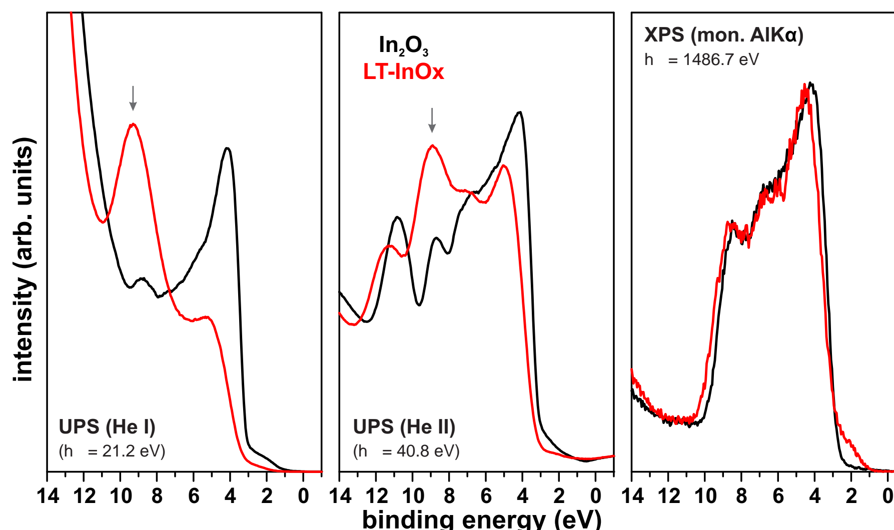

Fig. 4.9: Valence band photoelectron spectra of In_2O_3 and LT-InOx films measured using He I ($h\nu = 21.2$ eV), He II ($h\nu = 40.8$ eV) and monochromated AlKα ($h\nu = 1486.7$ eV) radiation.

function as has been for example reported for doped In_2O_3 films [122]. However, the origin of this behaviour can have manifold reasons. It may be related to a surface dipole induced by adsorbates, to the surface non-stoichiometry or to a change of the energetic position of the electron states due to the nanoscopic dimensions of the indium oxide crystallites with an average diameter of 7 - 8 nm. Strong band bending effects are normally not expected for nanoparticles [130].

In order to study the UV photoreduction and ozone oxidation cycle, on which the principle of operation of these LT-InOx sensors is based on, model experiments have been carried out in the surface analysis system. In the actual sensor assembly, a LED with a wavelength of 375 nm is used for the regeneration of the active layer after interaction with O_3 (see Fig. 4.1). In order to mimic the influence of this light source for comparable experiments in UHV, the samples were irradiated by a mercury discharge lamp, which has a broad emission spectrum with a cut-off photon energy of $\sim$5.0 eV ($\lambda \sim 250$ nm) [23]. The LT-InOx samples were illuminated by light generated from this Hg lamp with or without an additional optical filter (cut-off wavelength 360 nm) inserted into the optical path in order to remove the high energy region of the emission spectrum.

Upon the initial illumination of the LT-InOx films with the used UV lamp, a pressure rise was detected in the UHV chamber. This desorption from the material is accompanied by a reduction of the carbon content as determined from the decrease of the C1s peak intensity at 283.9 eV in the XPS measurements (not shown). Furthermore, an interesting observation is made in the valence band measurements. Fig. 4.10 compares the electron emission signal from a LT-InOx film before and after illumination with the Hg lamp. A broad distribution of additional electron states occurs close to the valence band edge which has its maximum intensity $\sim$0.5 above the VBM (3.3 eV). This feature is known for many polycrystalline oxide materials to originate from intrinsic defects that can, for example, be generated by harsh ion bombardment or annealing [131, 110]. Theoretical calculations on the energetic position of defect levels inside the band gap of indium oxide predict that this feature is due

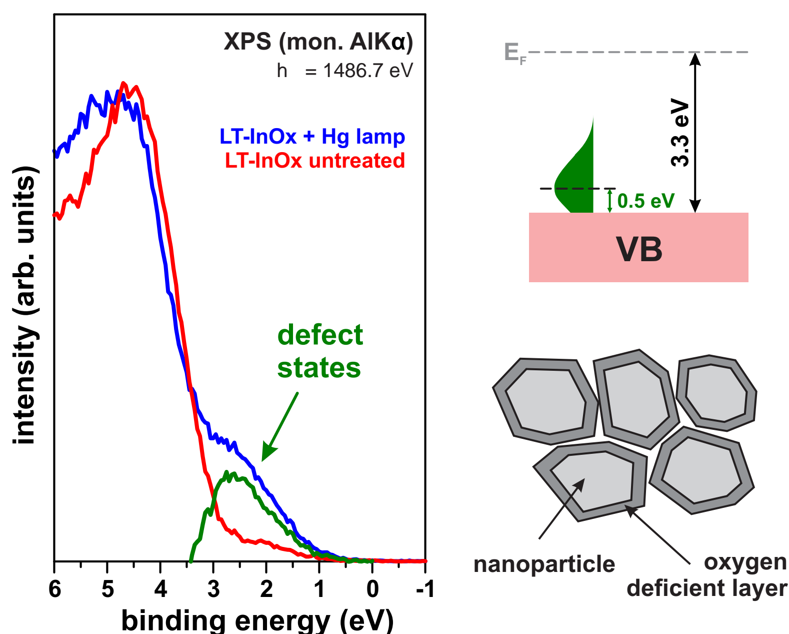

Fig. 4.10: UV-induced changes of the valence band states of LT-InOx films. Defects states are generated approximately 0.5 eV above the valence band maximum. The schematic depicts the proposed formation of a strongly reduced crystallite surface layer with a high content of oxygen vacancies.

to the existence of oxygen vacancies [132, 133], which is conform to the properties of other unstoichiometric oxide surfaces, such as SnO_{2-x} and TiO_{2-x}. Therefore, the observation of the defect states above the VBM in the PES spectra can be used as indicator for the existence of oxygen defects, or more correctly In derived states (5s-5p) arising from broken In-O bonds [111]. For each missing oxygen atom, up to two additional electrons are existing in the material which are contributing to a higher electron concentration. In consequence, the remaining unsaturated indium ions are very reactive and can act as centers for the adsorption of atoms and molecules. Nevertheless, the large amount of these defect states for the LT-InOx films after UV irradiation is surprising and points towards a high concentration of reactive centers at the surface of the 7 - 8 nm large indium oxide crystallites.

Summarizing the results from the structural and spectroscopic characterization of indium oxide films grown by MOCVD at 200°C, the following conclusions can be drawn: Due to the low growth temperature and hence limited diffusion of adatoms at nuclei, the crystallite diameter is in the range of a few nanometer. These nanocrystals exhibit a strong deviation in the surface stoichiometry compared to conventional In_2O_3 films. A reduction of the oxygen content of - 33% was observed. It is anticipated that especially the outermost layers of the particles consist of a high degree of oxygen vacancies resulting in the existence of excess electrons, which are partially localized at the remaining indium atoms forming reactive defect sites. The proposed scenario is schematically depicted at the right bottom of Fig. 4.10. The existence of an oxygen deficient top layer results in a very high reaction potential of the nanocrystal surface. During growth in the reaction chamber, the defects are decorated with cracking products from the used $In(CH_3)_3$ that are weakly bound to the surface of

the particles. By UV irradiation or annealing of the LT-InOx layers above 200°C (results not shown here), these bonds are broken and consequently the carbon species desorb from the surface and the existing defect sites are "activated" for the interaction with other gases such as ozone.

4.4 UV photoreduction and oxidation of LT-InOx sensor surfaces

In the last section, the initial properties of the LT-InOx thin films have been characterized. In order to examine the interaction of these films with ozone, adsorption experiments have been performed on previously UV irradiated films. Since ozone is unstable and cannot be transferred through long gas inlet tubes, a special setup had to be used for the oxidation experiments. For this, the samples were transferred into the load lock chamber (base pressure $\sim 5\times10^{-8}$ mbar) which was connected to a self made ozone generator consisting of a tube filled with pure oxygen (99.9999%) and a high intensity UV discharge lamp that induced the ozone generation. In that way, an O_3 concentration of up to 1000 ppm (0.1%) could be realized. The load lock chamber was then flushed with this O_3/O_2 gas mixture several times and in that way the indium oxide samples could be fully saturated by these oxidizing species. In this context it has to be mentioned that the co-exposure with molecular oxygen might lead to O_2 induced changes of the surface. However, this is a minor effect and can be neglected in the considerations here, since ozone has a much higher reactivity and provokes the important processes related to the oxidation of the indium oxide surface. This is in

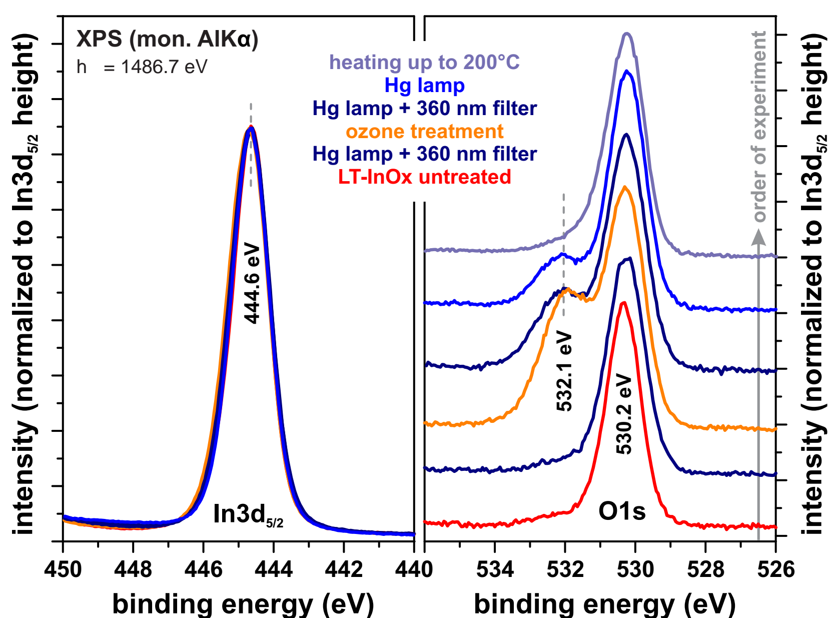

Fig. 4.11: Changes of the $In3d_{5/2}$ and O1s photoelectron spectra of LT-InOx films upon UV illumination and ozone oxidation. The spectrum after heating at 200°C from a different series of measurements is shown for comparison. For details of this series, see Fig. 4.13 and the corresponding text.

agreement with the electrical characterization, where only a minor influence of the sensor performance on the co-existence of O_2 is found. The interaction of the LT-InOx films with O_2 and further oxygen containing molecules is examined in more detail at the end of this section.

Figs. 4.11 and 4.12 represent photoelectron spectra measured during a cycle of successive UV-irradiation and ozone oxidation treatments of a LT-InOx sample. As already discussed, the initial UV exposure has only influence on the C1s signal, which is reduced in combination with the formation of the oxygen vacancy related states above the VBM. When the samples are brought into contact with ozone, distinct spectral signatures are observed. First of all, an additional component in the O1s signal is detected at 532.1 eV. It has approximately 50% of the intensity of the initial oxygen signal, which corresponds to a capture of the initially missing $\sim$ 33% of oxygen. Therefore, it can be stated that the interaction with O_3 is very efficient to compensate the oxygen deficiency inside the material since many of the active sites are decorated by the provided adsorbates. However, the oxygen is not incorporated into the crystal structure forming In_2O_3, since the chemical bonds of the additional oxygen have a different binding energy. The occurrence of the feature at 532.1 eV is similar to observation reported in earlier works on the interaction of ozone with indium oxide films prepared by sol-gel methods [97, 102]. The difference between the films prepared by sol-gel compared to the MOCVD films is that they initially already exhibit a large amount of oxygen adsorbates before ozone interaction.

In addition to the In3d and O1s core level measurements, examinations of the valence band structure upon O_3 interaction gives further information on the adsorption process. The emission from the defect states, which is not as pronounced in the UPS measurements compared to the results from XPS (for comparison see the respective spectra after illumination with the Hg lamp without filter in Fig. 4.10 and Fig. 4.12), is strongly reduced. Further-

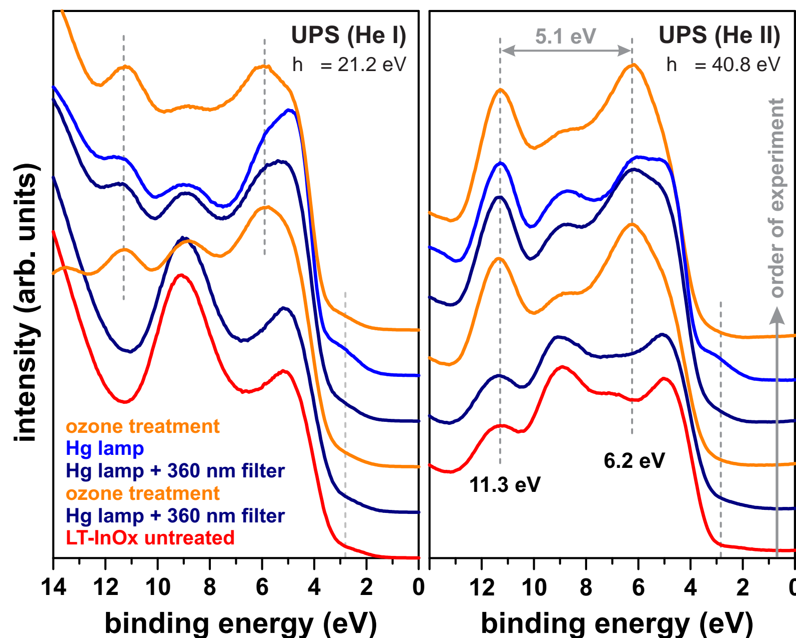

Fig. 4.12: Changes of the valence states of LT-InOx films upon ozone oxidation and subsequent UV illumination.

more, two features due to oxygen adsorbate related states appear in the valence band at 6.2 and 11.3 eV and the valence band maximum is shifted by 0.2 eV away from E_F.
The regeneration of the sensor is implemented by illumination with UV light. PES experiments on the influence of the UV irradiation after ozone oxidation show that the adsorbates are partially desorbed, but do not completely recover the initial conditions as after growth. As can be deduced from Figs. 4.11 and 4.12, the emission from the structures associated to the oxygen adsorbates are only in parts reduced to about 50%. The degree of desorption is further dependent on the used light intensity and, more critically, the wavelength. For the measurements performed after illumination with the Hg lamp without filter, the highest degree of adsorbate removal is achieved. In this case, the reappearance of the defects states in the photoelectron spectra is also stronger and the valence band edge shifts back to the initial value of 3.3 eV. Upon the second cycle of oxidation, the same properties are found as after the first cycle. Hence, once the sensor is initiated by UV irradiation, the LT-InOx films can be reversibly oxidized and reduced by ozone oxidation and subsequent UV illumination. Thus, while the initial surface configuration after deposition might not be recoverable, the surface stoichiometry is altered within steady state conditions.
Since the ozone sensors can also be reactivated by annealing, the desorption of oxygen adsorbates upon thermal treatment were additionally investigated. Measurements of the valence band and In4d level during gradual increase of substrate temperature of an ozone oxidized LT-InOx film are presented in Fig. 4.13. Initially the surface exhibits the adsor-

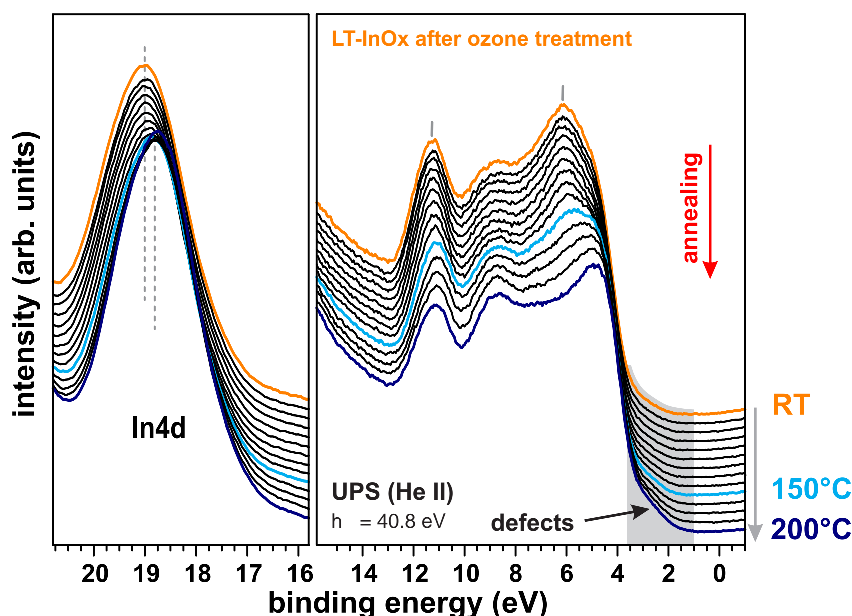

Fig. 4.13: Temperature dependent desorption of ozone-induced adsorbates from LT-InOx surfaces.

bate related spectral features at 6.2 and 11.3 eV. A reduction of this emission is detected at temperatures above 150°C and the defect states induced emission above the VBM increases simultaneously with oxygen desorption. Finally the adsorbates are completely removed at temperatures above 200°C and the valence band spectrum becomes similar to LT-InOx. Additionally a shift of the valence states by ∼0.2 eV is detected (best visible in the shift of the In4d peak maximum). In contrast to the regeneration of the surface with UV light, for

careful annealing of the films up to 200°C, the entire amount of adsorbed oxygen is removed. This statement can already be deduced from the comparison of the valence band spectra in Figs. 4.12 and 4.13 and is further supported by the complete disappearance of the peak at 532.1 eV in the O1s spectrum after annealing up to 200°C (see Fig. 4.11). Therefore, when the indium oxide sensors are operated at higher temperatures, a certain balance between adsorption and desorption of oxygen will occur and a decrease in sensitivity is expected. Furthermore, the reactivity towards reducing gases, such as CO or H_2, might be enhanced and consequently cross-sensitivity effects are expected [104].
After the cycles of oxidation and subsequent photo-induced reduction, differences in the electronic properties were found to occur on the basis of photoelectron spectroscopy measurements. A small shift of the core levels is found after every surface treatment (see Fig. 4.11). All measured binding energy values vary slightly - after oxidation the In3d and O1s peaks are slightly shifted to higher binding energy compared to the reduced state after UV illumination. Additionally, from the UPS measurements, a clear trend in changes of

sample	$E_F - VBM$ **(eV)**	ϕ **(eV)**
In_2O_3	3.1	4.2
LT-InOx	3.3	4.4
LT-InOx + O_3	3.5	4.6
LT-InOx + O_3 + UV	3.3	4.4

Tab. 4.1: Variation of the work function and the valence band maximum of different indium oxide samples as a function of preparation conditions.

the VBM and work function was determined. Tab. 4.1 summarizes the different locations of the VBM with respect to E_F as well as the determined work function depending on the different indium oxide samples and surface treatments. Upon ozone interaction, the work function increases by 0.2 eV while the distance between Fermi level and VBM is also measured to be 0.2 eV larger. In a classical model for single crystalline surfaces, this behavior could be interpreted in terms of an enhanced downward band bending due to accumulation of additional electrons at the surface together with a surface dipole $\Delta\phi_{dip} = 0.4\,\text{eV}$ which is induced by the formation of oxygen adsorbates. This is schematically displayed in Fig. 4.14. Problematic is the fact that this simple model does not agree with the changes of the electric properties. During ozone oxidation, the indium oxide film resistance increases strongly, which has two main influencing factors: *i)* the electron concentration in the films is reduced due to localization of charge by the adsorption of oxygen atoms and *ii)* formation or increase of the contact barrier between single crystallites that strongly influences the current flow through the film [96]. The measured increase in the work function of the LT-InOx film after exposure to ozone is indeed in accordance with the electrical characteristics. Oxygen atoms adsorb at the In defect sites of the crystallite surface and charge is transferred from the material towards the adsorbate. The formed dipole with the negative charge pointing away from the surface explains the increase in work function. However, the observed shift of the valence band at the surface away from the Fermi level is contradictory to what is expected to occur during oxidation. One would expect a depletion of electrons at the crystallite surface since charge is removed from the particle and transferred towards the

adsorbed oxygen atoms. Assuming a constant band gap, this leads to an upward bending of both, the valence and conduction band at the surface. In contrast, the experimentally observed shift of the VBM away from the Fermi energy points towards a downward bending of the valence and conduction band due to charge accumulation at the surface or towards a shift of the bulk Fermi level caused by an increase of electron concentration. An UV-

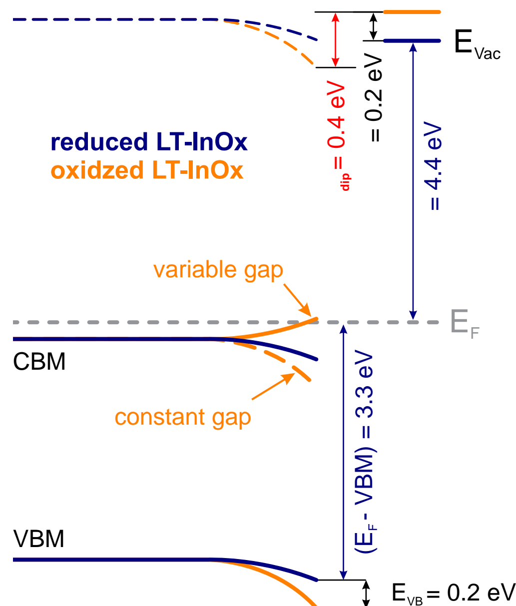

Fig. 4.14: Schematic of a possible band distribution at indium oxide nanoparticles after ozone oxidation and UV-induced photoreduction. The conduction band after oxidation is shown for the case of a constant or variable band gap. For discussion, see text.

induced photocurrent could be an explanation for this observation, since the LT-InOx films are known to be sensitive to UV light. However, the used photon energies of 21.2 and 40.8 eV are usually not considered to induce these effects that typically occur when films are excited by light with an energy slightly above the band gap in order to excite electrons into the conduction band. With the assumption that photocurrent-induced influences can be neglected, a different interpretation of the experimental results is possible. The UPS measurements are even more surface sensitive than the signal from XPS. Since the core level appear not to shift as much as the VB, this would imply that most of the changes appear in a very thin layer in the vicinity of the surface. As presented in the last section, the nanoparticle films have a surface that is strongly reduced with a high degree of oxygen vacancies. When this layer is oxidized by ozone, the stoichiometry at these particles is strongly modified. This can also be interpreted in terms of a change of the material properties and might lead to a different band gap at the surface. For oxidation one would expect a higher value. As displayed in Fig. 4.14 a changed band gap value would lead to an upward bending of the conduction band and simultaneously explain the downward shift of the valence band. This model would lead to a depletion of carriers and to the formation of a small energy barrier at the interface of the crystallites, since the conduction band might be bent above the Fermi level, which explains the drastic changes of the electrical properties (strong increase in resistance) after interaction with ozone and hence confirms

the sensor performance. This suggested model is able to correlate the experimental results from PES measurements with the electrical characteristics of LT-InOx films. The concept of an altered surface band gap has also been suggested by other persons [111] and explains the experimental observations. Since the discussions presented here are only restricted to the properties of the active layer, it should not be forgotten that many other parameters also influence the device performance. Especially the optimization of the UV source used as well as the properties of the metal contacts plays an important role for the resulting sensitivity of the produced ozone detectors. Some other aspects related to environmental influences will be discussed in the following.

The final sensor device applied in ozone detection at ambient conditions is exposed to many external influences. Besides pollution of the material by dust, especially humidity is a factor that influences the performance of In_2O_3 based ozone sensors [129]. The interaction of molecular oxygen and water with the UV reduced LT-InOx films was therefore examined in addition. The samples were initially activated by illumination with the Hg lamp and subsequently exposed to 1 bar O_2 or 17 Torr H_2O in the load lock chamber. Special attention was paid to carefully evacuate the gas inlet system to assure experiments with pure gases. Also, the gas composition was validated by QMS measurements.

The In4d and valence band spectra of the LT-InOx films after interaction with ozone, oxygen, water, and air are compared in Fig. 4.15. It should be noted, that although the exposure time was similar for all gases, the actual amount of molecules offered to the sample is different for the series of measurements. The generated 1000 ppm of ozone correspond to a partial pressure of ~ 0.8 Torr and have to be compared to 17 Torr water or 760 Torr O_2 exposure. The corresponding exposure in Langmuir (L) is indicated in the spectra. Surprisingly, for all performed gas experiments, the most significant spectral features are the already described structures at 6.2 and 11.3 eV. Although not at the same absolute energy, these two structures are similar to the observed oxygen-induced adsorbate states on InN(0001) (at 5.2 and 10.3 eV, see Fig. 3.16) with the same energy splitting of 5.1 eV. It is anticipated that the same adsorbate is formed in both cases and the energy shift is due to the different band structure of InN and indium oxide surfaces. Similar adsorbate structures have also been found for the interaction of water with monocrystalline indium oxide films [111]. This implies the capability of the indium oxide nanoparticles to react with oxygen containing molecules. Only in the case of exposure with O_2, the adsorbate related structures are weaker pronounced and the degree of coverage is much lower, which points towards a lower reaction rate with the LT-InOx surfaces compared to O_3 or H_2O.

Unfortunately, due to the complexity of the indium oxide lattice, supporting theoretical investigations on the adsorption of oxygen at In_2O_3 surfaces are lacking in literature and consequently an interpretation can only be made on the basis of the obtained experimental results. Since the exposure to O_3 and H_2O leads to the same electronic states, the observed features are not related to hydrogen. Furthermore due to the fact that O_2 is rather weakly interacting with the surface and O_2 or O_3 adsorbates formed by dissociation of water is very unlikely, the adsorbate is most likely atomic oxygen. The additionally observed increase in work function which is a results of the formation of a surface dipole, points towards the adsorption of negatively charged oxygen atoms (O^- or O^{2-}). It is anticipated that O_3 and H_2O molecules are dissociated at the surface of the oxygen deficient indium oxide parti-

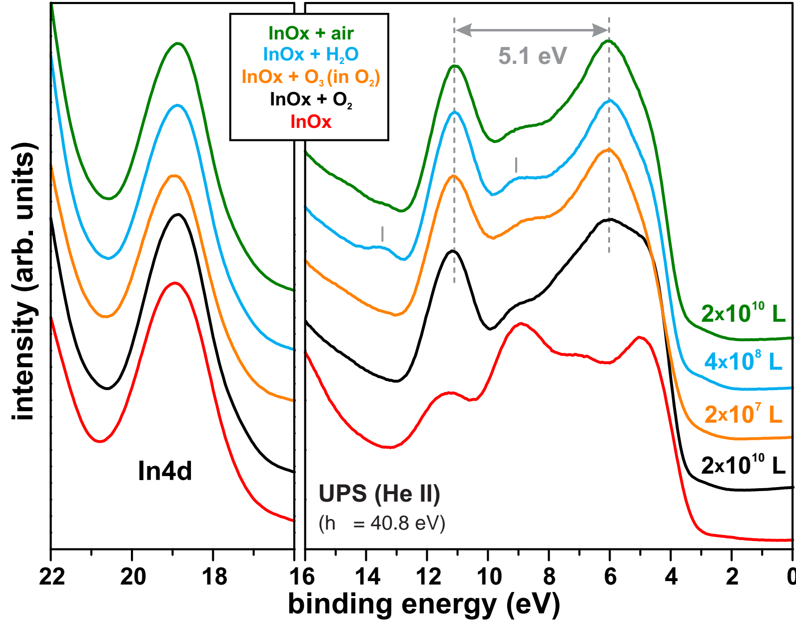

Fig. 4.15: In4d semi-core level and valence band spectra of LT-InOx films after interaction with O_3, O_2 and H_2O measured using He II radiation ($h\nu = 40.8\,\text{eV}$).

cles, negative oxygen ions bound at the defect sites and the remaining oxygen or hydrogen remains in gas phase.

$$O_3 \rightarrow O_2\ (gas) + O \tag{4.2}$$

$$H_2O \rightarrow H_2\ (gas) + O \tag{4.3}$$

$$O + e^- \rightarrow O^-_{ads} \tag{4.4}$$

The unsaturated indium sites are very reactive and act as centers for the adsorption of oxygen by transfer of electronic charge. Tentatively it is believed that the dissociated species are bound in the form of negatively charged oxygen ions (O^-). Similar conclusions that O^- is formed, have been found from electrical characterization of In_2O_3 ozone sensors on the basis of O_3 exposure dependent measurements of the sensor response [99, 102]. The increase in film resistance is caused by the removal of electrons from the defect rich oxide upon adsorption of atomic oxygen that is formed due to the decomposition of ozone [99]. However, there is one publication reporting that the formation of O^- is restricted to temperatures of 200°C and higher, while at lower temperatures the adsorption of O_2^- is more likely [102]. But this would imply the dissociation of two water molecules and the subsequent diffusion and recombination of two oxygen atoms in order to form molecular oxygen ions. The fact that atomic oxygen species are formed by dissociation of water was also not expected before performing the experiments, because H_2O typically dissociates at metal oxide surfaces by forming OH-groups [106], which can be excluded as the reason for the two main adsorbate states, since the energy separation of 5.1 eV is larger than expected for OH-states [134] and the formation of OH by O_3 exposure is unlikely. It has to be mentioned that the valence band spectra in Fig. 4.15 contain two additional structures at 9.1 and 13.4 eV (indicated in the figure) for the samples that were exposed to water or air. These features might be related to the 3σ and 1π bonds of OH, but this has to

be confirmed in further examinations using extremely adsorbate sensitive techniques; for example metastable impact electron spectroscopy or high-resolution electron energy loss spectroscopy. Nevertheless, the amount of this second adsorbate group is relatively low compared to the dominating oxygen adsorbate states.
The results from the PES measurements allow some conclusions on the influence of ambient gases like oxygen and water on the performance of ozone sensitivity. First, both species interact with the indium oxide nanoparticles forming the same adsorbate species as ozone. Especially after the exposure to H_2O, the surface exhibits the same degree of coverage. Therefore, in the presence of water due to humidity, it is expected that water molecules occupy available adsorption sites and lead to a reduced sensitivity and response of the indium oxide layers towards ozone compared to dry conditions. On the other side, pure oxygen alone is not as reactive and is believed to influence the sensor performance not as much as water. It has to be pointed out that especially the instability of ozone and its high oxidation potential lead to a much higher reaction rate compared to other oxygen containing molecules. Exposure dependent measurements in UHV in order to study the reaction kinetics would be desirable, but not easy to realize since ozone molecules will most likely decay before reaching the surface. Here one has to refer to the results from the electrical characterization of the processed sensor films [129].

Chapter 5

Surface composition and electronic properties of indium tin oxide and oxynitride films

5.1 Indium tin oxynitride - transparent conductive oxide with improved optical properties

Indium-tin-oxide (ITO) thin films are strongly degenerate semiconductor materials, since the incorporation of tin as well as the formation of oxygen vacancies result in n-type conductivity. Due to the high electron concentration and occupancy of the conduction band states, the onset of optical absorption is typically between 3.7 eV and 4.4 eV [135, 136] depending on the fabrication technique. Due to its unique properties, such as high electrical conductivity, very high optical transmittance, high infrared reflectance, excellent hardness and chemical inertness [137], ITO is used in optoelectronic applications where it serves as an optical as well as contact material, in, for example, display devices, solar cells, organic light emitting diodes, touch screens and many other optical applications [138]. Additionally, due to the lack of p-type oxides with similar properties (wide band-gap and at the same time high conductivity) ITO is being used in many III-V based optoelectronic devices. In particular, for the case of solutions based on the wide band gap III-nitride compounds, ITO has been used as ohmic contact material, e.g. on p-type GaN layers [139, 140]. Indium tin oxide thin films are commonly deposited by reactive sputtering from an ITO target in a reducing atmosphere or from elemental targets (In, Sn) in an oxygen atmosphere as well as using sol-gel methods. A few years ago, it was found that the use of N_2 as process gas during magnetron sputtering of indium-tin-oxide (ITO) leads to the incorporation of nitrogen in the ITO thin film forming indium-tin-oxynitride (ITON) [141]. In comparison to ITO films that were deposited in a Ar plasma using identical conditions, differences in the electrical and optical properties were observed [142]. Rapid thermal annealing (RTA) results in improved optical properties due to a shift of the absorption edge to shorter wavelength. Fig. 5.1 presents typical measurements of the optical transmission of ITO and ITON films directly after deposition and after RTA at 800°C. The blue shift of the onset of transmittance after annealing is clearly evident. However, the improvement of optical properties

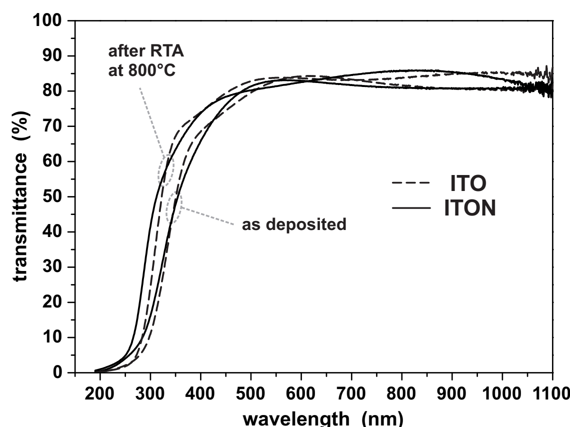

Fig. 5.1: Influence of rapid thermal annealing on the optical transmittance of ITO and ITON films. A typical blue shift of the absorption edge is found after rapid thermal annealing at 800°C.

is only in parts related to the changes in carrier concentration. The larger window of transparency in the UV-region for ITON is believed to be correlated to the incorporation of nitrogen into the material [142]. The carrier concentration of as deposited ITON films ($n_d \sim 10^{19}$ cm^{-3}) is more than one order of magnitude lower compared to the ITO reference films produced in Ar plasma ($n_d \sim 2 \times 10^{20}$ cm^{-3}). While rapid thermal annealing has only minor influence on the carrier concentration of ITO, a strong impact on RTA is found for the films deposited in a nitrogen plasma. After annealing of the films at 600°C, comparable values of carrier concentration as for the ITO films were measured. The dependence of the carrier concentration on annealing temperature is presented in Fig. 5.2 for a set of ITON films deposited with different plasma power. The increase by about one order of magnitude is typically observed at $T \geq 600$°C, independent on deposition power.
In this work, an attempt is made to correlate the observed modifications of the technologically relevant material properties (carrier concentration and transmittance) to studies on the surface properties of these films (chemical composition, chemical states and work function). Besides the fact that nitrogen is inserted into the ITON material, little is known about how the N atoms are actually incorporated into the structure. Furthermore the lack of knowledge about the underlying processes leading to this strong increase in carrier density upon RTA initiated the investigation of the surface properties using electron spectroscopy. Surface changes of ITO thin films after various treatments, like annealing [143, 144], KrF excimer laser irradiation [145], plasma treatments (in atmospheric air [146], N_2, Ar or O_2 [147, 122]) and UV-ozone exposure [148] have already been reported in literature. However, at present only little information is available for ITON films.

5.2 ITO(N) sample preparation and morphology

The supplied ITO and ITON thin films[1] with a thickness of 200 - 300 nm were fabricated by rf-sputtering ($\sim$ 13.56 MHz) in plasma containing Ar or N_2, respectively. The deposition

[1]The samples were provided by M. Koufaki and E. Aperathitis (Microelectronics Research Group at the Foundation for Research and Technology-HELLAS in Heraklion, Crete).

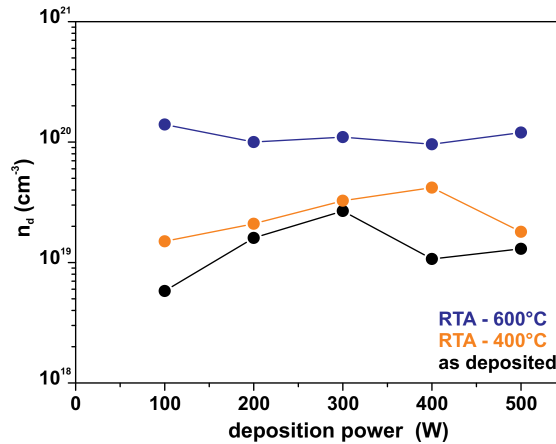

Fig. 5.2: Influence of deposition power and annealing temperature on the electron concentration of rf-sputtered ITON samples.

was performed at room temperature on pre-cleaned Si wafers (1 - 10 Ωcm) in a Nordiko NS2500 system using an indium-tin-oxide target (80% In_2O_3 + 20% SnO_2, diameter 6 inch). During this procedure the gas flow (Ar for ITO and N_2 for ITON) was controlled by mass flow controllers to maintain a total pressure of 5×10^{-3} Torr in the chamber (base pressure $< 1\times10^{-9}$ Torr) [141]. The dependence of the surface chemical composition and the electronic properties on the rf-power (150 - 550 W) was examined by X-ray and ultra-violet photoelectron spectroscopy (XPS, UPS) as well as electron energy loss spectroscopy (EELS). Changes upon annealing of the ITO and ITON samples were investigated after *ex-situ* rapid thermal annealing (RTA) (heating ramp ∼45 K/s, t_{hold} = 1 min, T = 400°C, 600°C and 800°C) in an N_2 atmosphere (flow 450 sccm). Results of the carrier density determined by Hall measurements for the samples under investigation are shown in Fig. 5.2. The samples were analyzed directly after loading into the UHV analysis system and after gentle sputtering with Ar^+ ions (2 keV, 30 min) for the removal of surface contaminants. Special care has been taken to avoid metal formation at the surface due to preferential sputtering of oxygen. Additionally, *in-vacuo* heating of as-deposited samples combined with a monitoring of the desorbing atoms and molecules using quadrupole mass spectroscopy (QMS) was performed. For further information of the elemental distribution, Auger-electron spectroscopy (AES) and depth profiling measurements have been carried out in a separate UHV system. Atomic force microscopy was implemented for the characterization of surface topography and roughness of the magnetron sputtered ITO and ITON films. The results of ITO and ITON samples deposited at 350 W are shown in Fig. 5.3. RF-sputtered ITO(N) films exhibit a polycrystalline structure with a typical grain size in the range of 50 - 100 nm [141]. An examination of the film morphology revealed that the roughness of the ITON films (rms 7 - 8 nm) was almost twice as large compared to the prepared ITO (rms 3 - 4 nm). Besides this aspect, only a minor influence of deposition power as well as post-growth rapid thermal annealing on the surface topography was detected. The grain size as measured by AFM and SEM remained well below 100 nm in all cases and no indication for lateral inhomogeneity across the sample was detected. This is important for the validity of the subsequently performed chemical analysis.

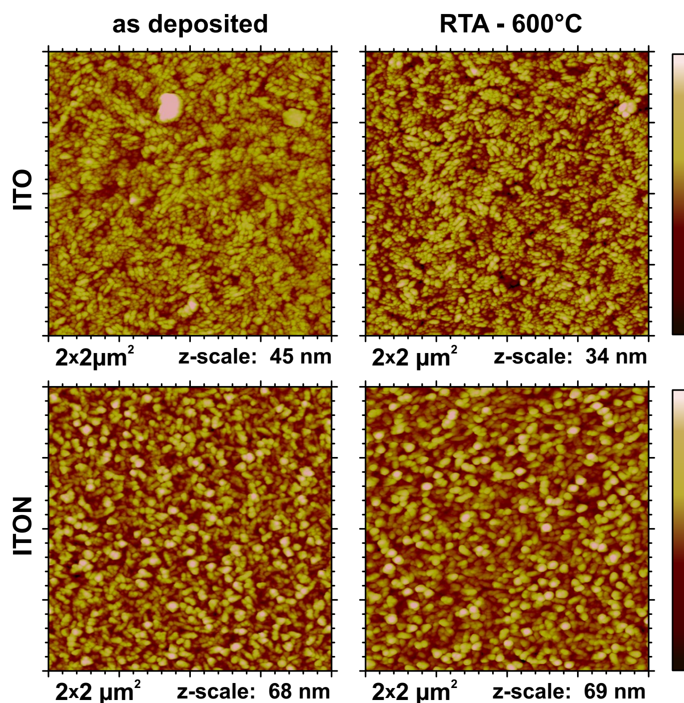

Fig. 5.3: Atomic force micrographs of ITO and ITON films deposited by rf-sputtering at 350 W (left column: as deposited films, right column: films after rapid thermal annealing at 600°C in N_2).

5.3 Analysis of the incorporated nitrogen in ITON

In order to characterize the elemental distribution through the films as well as the surface chemical composition of ITON and ITO samples prepared by rf-sputtering, X-ray photoelectron spectra and Auger-electron depth profiles have been recorded. The typical XPS core level peaks related to the detected elements have their maximum intensity at a binding energy (BE) of 18.4 eV, 26.2 eV, 444.7 eV, 486.5 eV, and 530.2 eV for the In4d, Sn4d, $In3d_{5/2}$, $Sn3d_{5/2}$, and O1s state, respectively. As expected for samples that have been deposited using N_2, nitrogen was also detected in the films. However, it is not uniformly distributed throughout the film, but concentrated in the first 40 - 50 nm. In deeper regions the N signal decreases below the detection limit of AES. Furthermore, for as-deposited ITON and ITO as well as annealed ITO samples, a fairly homogeneous distribution of indium, tin and oxygen through the films is found [149]. This is not the case for annealed ITON films (see Sect. 5.4). For a quantification of the amount of inserted nitrogen, the XPS core level spectra were fitted using Gauss-Lorentz functions, after the removal of a Shirley-type background. The elemental proportions were calculated under the assumption of a homogeneous distribution of all detected elements through the depth of information of the XPS measurement, taking into account the cross section, and asymmetry parameters of the detected spectral lines according to Yeh and Lindau [11]. In the case of film uniformity

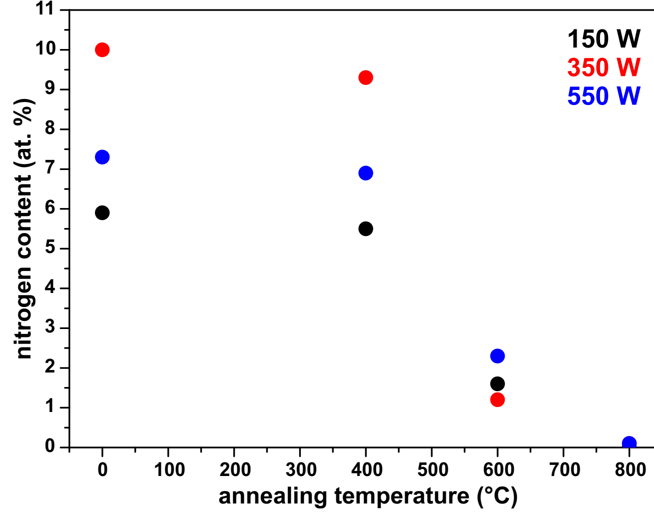

Fig. 5.4: Amount of incorporated nitrogen in ITON films deposited at 350 W depending on subsequent rapid thermal annealing.

Eq. 2.10 simplifies to

$$I_i \propto \sigma_i(\hbar\omega) \cdot L_i(\gamma, \hbar\omega) \cdot T(E_i) \cdot N_i \cdot \lambda_m(E_i) \tag{5.1}$$

The transmission function of a hemispherical electron analyzer is normally $T(E_i) \propto 1/E_i$ and the IMFP of electrons can be approximated with $\lambda_m(E_i) \propto \sqrt{(E_i)}$. This enables the calculation of the chemical composition C_i in at. % by a summation of the sensitivity factor corrected photoemission intensities I_i using the dominant spectral line of each detected element (in this case In3d, Sn3d, O1s and N1s)

$$C_i\,(at.\,\%) = \frac{N_i}{\sum_i N_i} \tag{5.2}$$

with

$$N_i = \frac{I_i \cdot \sqrt{(E_i)}}{\sigma_i \cdot L_i} \tag{5.3}$$

As deposited ITON films possess a nitrogen content of 6 - 10 at. %, which depends on the used deposition power (see Fig. 5.4). The whole set of data recorded for the series of samples deposited at 150, 350 and 550 W is presented in Fig. 5.4. Interestingly, the maximum nitrogen incorporation is achieved at 350 W, while a higher deposition power results in a lower efficiency. Although the absolute values in the nitrogen proportion differ slightly, a general trend upon rapid thermal annealing can be deduced. RTA at 400°C results in a minor reduction of the amount of incorporated nitrogen. For samples that have been heated at 600°C, the nitrogen signal is strongly reduced to less than one third of the initial value. Finally, after RTA at 800°C the amount of incorporated nitrogen is below the sensitivity limit of photoelectron spectroscopy ($\sim$0.1% for the used setup). Clearly, desorption of nitrogen takes place at temperatures $\geq$600°C.

For a detailed chemical analysis of the existing nitrogen at the surface, measurements of the N1s electron emission of samples before and after Ar^+ ion bombardment were made.

The results of the ITON sample series prepared at 350 W and annealed at different temperatures are presented in Fig. 5.5. In samples that have not undergone any treatment after deposition, the nitrogen atoms are found to exist in four different chemical states located at binding energies (BE) of 396.7 eV, 398.3 eV, 400.0 eV and $\sim$404.0 eV, respectively. The structure at 400.0 eV is only found for directly loaded samples and can be easily removed by the Ar^+ ion bombardment procedure. These states only exist at the surface and are typical for N-O bonds which are most likely formed due to oxidation of the samples at ambient conditions. The feature at 396.7 eV is attributed to nitrogen bound to metal atoms (N-In and N-Sn bonds). Unfortunately, the binding energy for both species is almost equal [150, 151] and a separation between these two contributions is beyond the energy resolution of the measurement. The third structure at 398.3 eV is found to originate from oxynitride bonds [152], where oxygen as well as metal atoms are located in the surrounding of the nitrogen atom (InN_xO_y). The peak at 404.0 eV can originate from two possible sources: a) NO_2 bonds or b) unbound nitrogen incorporated into the crystal structure. Since no indication for a NO_2-related component was found in the O1s signal and the rf-sputtering process is performed in a nitrogen plasma, this structure at 404.0 eV, in very good agreement with a nitridation study of III-V semiconductor surfaces, is assigned to incorporated unbound nitrogen that is formed due to the harsh deposition conditions. It is believed that this unbound nitrogen is most likely located at interstitial sites [153, 154].
Upon RTA, besides a small reduction of the total nitrogen concentration (see Fig. 5.4), no changes concerning the nitrogen states were observed after annealing at 400°C. Obviously, since the samples were exposed to ambient conditions prior to introduction to UHV, the surfaces that have been characterized prior to ion bombardment still reveal a non-negligible amount of N-O and oxynitride bonds. However, these features are present only due to reoxidation of the surface and are not related to changes induced by annealing of the films. For tracking these changes, the ion bombarded surface measurements have to be analyzed. As already mentioned, the amount of nitrogen is strongly reduced after RTA at 600°C. This is mainly related to the disappearance of the structure at 404.0 eV as well as almost the entire oxynitride component and parts from the metal-N signal, reducing the total N content to less than 2%. Finally, the rest of the nitrogen vanished after annealing at 800°C.
For a better analysis of the underlying desorption processes, ITON sample have also been heated and analyzed in the UHV system. The same behavior was found for the disappearance of unbound nitrogen as well as oxynitride bonds. In order to understand the processes related to annealing of the ITON films, quadrupole mass spectroscopy (QMS) measurements were performed during annealing under UHV conditions. The desorption of molecules from the film as a function of temperature was analyzed *in-situ* during linear increase of the sample temperature. It has to be mentioned that the used experimental setup is not sufficient for any quantitative desorption analysis as in thermal desorption spectroscopy (TDS), since the QMS setup geometry (see Fig. 2.1) allows only analysis of the residual gas in the whole preparation chamber including effects of desorption from parts of the manipulator assembly. Furthermore the heater assembly is not optimized for guaranteeing linear ramps at high heating rates. However, qualitative information about the temperature-induced processes can still be obtained. The most striking effect during ramping up the temperature of a ITON sample is detected in the range between 550°C and

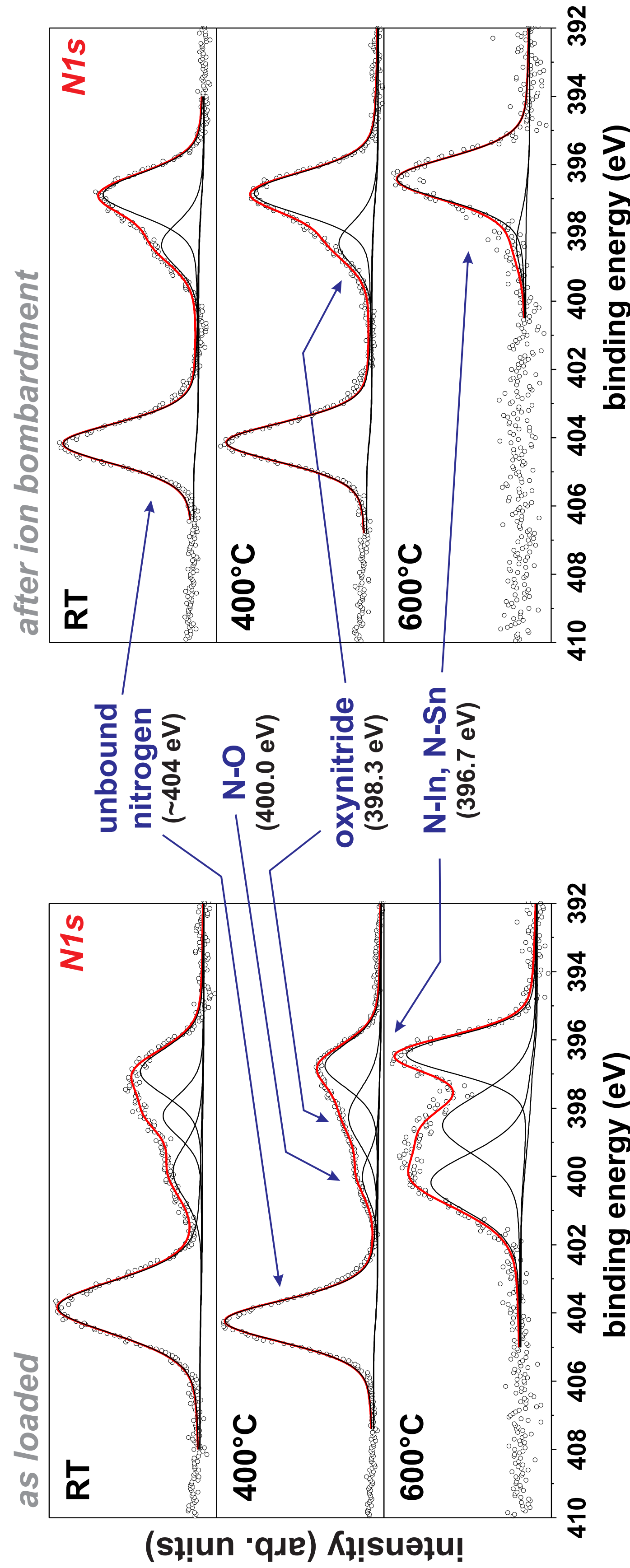

Fig. 5.5: N1s core level spectra of ITON films deposited at 350 W prior to and after rapid thermal annealing at 400°C and 600°C. The various detected nitrogen bonds with their respective binding energy are indicated. Please note that the relative signal height in the spectra is varied in order to visualize the chemical bonds. A comparison of the nitrogen quantity can be found in Fig. 5.4.

600°C. An abrupt release of nitrogen takes place (rapid increase in signals m/e =14 and 28), while only minor desorption of N_2O was measured. Furthermore, no release of NO, NO_2 or O_2 was found. Any signal related to desorption of In or Sn is not expected at these temperatures and indeed could not be detected. This qualitative experimental finding is in very good agreement with the RTA induced changes observed in the N1s signal. Most of the incorporated unbound nitrogen is released at a certain temperature, while the oxynitride bonds are simultaneously broken. It should be noted that the temperature increase at the sample during the performed annealing in the UHV chamber was rather slow with a temperature ramp of $\Delta T/\Delta t \sim 15$ K/min, the RTA process is much faster ($\Delta T/\Delta t = 45$ K/s). This leads to incomplete nitrogen removal for 1 min RTA at 600°C. Slightly higher temperatures (800°C) are necessary to also remove the N-metal bonds.

5.4 Origin of the thermally induced changes in ITON films

Besides the already discussed release of nitrogen, several other impacts of rapid thermal annealing on the surface properties were found. The left side of Fig. 5.6 shows X-ray induced Auger-electron spectra of ITON samples which were heated at various temperatures using rapid thermal as well as UHV annealing. The measurements include the signals from the In(MNN), Sn(MNN) and O(KLL) transition, respectively. For the RTA process, a strong increase in the Sn(MNN) peak intensity was observed after annealing at $T \geq 600$°C. The amount of Sn is even higher when untreated ITON samples were annealed under UHV conditions. In this case, the signal intensity of Sn(MNN) is equal to the In(MNN) signal. This increase of the surface tin content is a strong indication for thermally induced surface segregation effects taking place above a certain temperature. AES depth profiles have been measured in a separate chamber[2] in order to evaluate the tin distribution within the first layers. The right part of Fig. 5.6 shows the depth profile of the $I_{Sn(MNN)}/I_{In(MNN)}$ peak area ratio for ITON films that have been treated by RTA at different temperatures. For untreated films and after 400°C, a uniform Sn distribution was found through the first 20 nm of the sample with a slight linear reduction of the Sn signal from the topmost layers into the bulk. The only difference is a slightly higher average value at 400°C. Upon RTA above 600°C, this compositional distribution is strongly modified. Now, the intensity ratio at the outermost surface is twice as high, decaying exponentially into the bulk to steady values much lower compared to the untreated samples. This implies a strong segregation of tin atoms from the bulk of the material towards the surface. However, this process is not related to the formation of a separate metallic tin phase at the surface, which would have been visible as a second component of the Sn(3d) core level in XPS. It has to be mentioned, that although such a drastic change of the ITON surface composition is found at $T \geq 600$°C, this behavior did not occur in the case of the ITO reference samples that have been deposited using Ar as discharge gas.

[2]The AES system (Thermo Microlab 350) is equipped with a high spatial resolution field emission electron beam column and a high energy resolution hemispherical analyzer. The primary electron beam (5 keV, 14 nA) had an incidence angle of 45° with respect to the surface normal and sputtering was carried out by a conventional scanned ion beam gun (Ar^+ ions, 1 keV, angle of incidence 47°). The measurements were performed by Ch. Mauder [155].

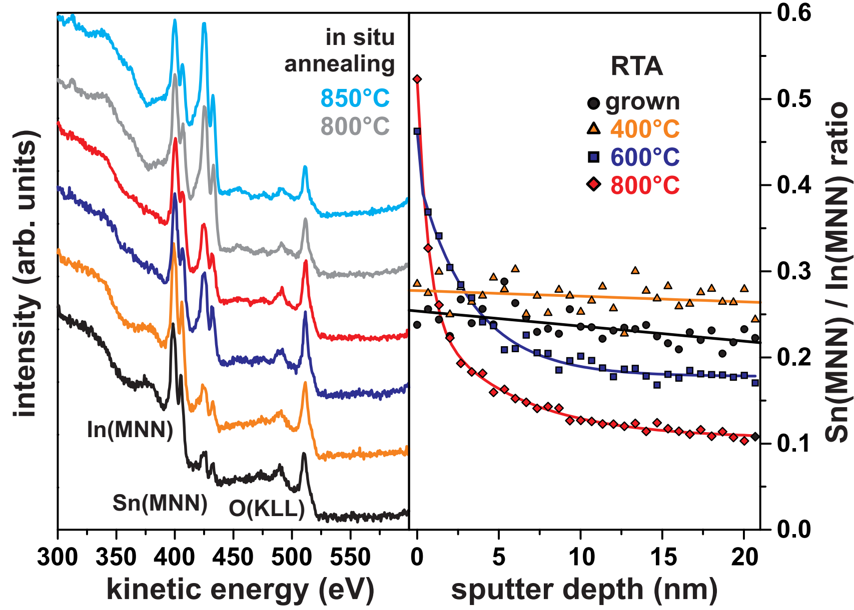

Fig. 5.6: Dependence of the In(MNN), Sn(MNN) and O(KLL) X-ray induced Auger-electron emission as well as the Sn/In intensity ratio depth profile on annealing temperature of ITON thin films.

The presented experimental results of the XPS, AES and QMS analysis allow some conclusions on the origin of the observed changes of surface, electrical as well as optical properties of ITON thin films with respect to the differences of ITO reference samples deposited in an Argon plasma. The high electron concentration in indium tin oxide is caused by two factors: *a*) the existence of a high content of oxygen vacancies and *b*) the incorporation of Sn atoms at In crystal sites leading to the effect of n-type doping [156]. The amount of existing oxygen vacancies is mainly influenced by the deposition conditions during magnetron sputtering (pressure, plasma power, sample temperature). In a highly reducing atmosphere, as used in this case for the deposition of ITO, the process conditions already result in the formation of a high concentration of oxygen vacancies and hence in a very high electron concentration (Hall measurements reveal $n_d \sim 2 \times 10^{20}$ cm^{-3}) right from the beginning. Therefore, any treatment that aims to achieve a further reduction of the material, such as RTA in nitrogen atmosphere, is not very efficient and has only a minor effect on the carrier concentration. A totally different behavior is found when the material is sputtered from an ITO target using N_2 as the discharge gas. In this case nitrogen is incorporated into the material. As described above, a huge amount is inserted unbound at interstitial sites [154]. Additionally, nitrogen is also incorporated in a high amount bound in the surrounding of In, Sn and O and it is supposed that nitrogen decorates the sites where typically oxygen atoms are missing resulting in trapping of electrons. This low amount of oxygen vacancies leads to a noticeable lower carrier concentration in these samples ($n_d \sim 10^{19}$ cm^{-3}). Since the incorporated nitrogen is not strongly bound, it can be released by thermal treatments. Annealing above a critical temperature of ~550°C causes the desorption of the weakly bound nitrogen, which is completely removed after RTA at 800°C for 1 minute. The remaining, previously N-decorated, sites can now act as a source for electrons, resulting in a strong

increase of the carrier concentration of the material. In this way comparable values are achieved as for the Ar-sputtered ITO films. The driving force for these processes is related to the thermal instability observed for all indium-containing III-V compounds, such as InP and InN, which results in thermal decomposition at temperatures above 450°C [71, 157]. However, the thermally induced changes are not restricted to a simple outdiffusion of nitrogen. The observation that Sn is additionally segregating from the bulk to the surface is an indicator for a rather complex rearrangement in the crystal structure. The enhanced Sn concentration at the surface after annealing also contributes to the observed increase in carrier concentration and could be an explanation for the differences in the transmission properties of ITO and ITON films after RTA at 800°C.
It has to be mentioned that thermally induced Sn segregation and enhancement of the carrier concentration has been observed in earlier works for ITO films which were prepared by magnetron sputtering [158] or using a sol-gel method [143]. The non-occurrence of these effects in the investigated ITO reference samples here is believed to be due to the used strongly reducing sputter conditions (Ar plasma). These conditions lead to a high degree of non-stoichiometry along with the existence of a high amount of oxygen vacancies in the material, in contrast to ITON thin films that have been produced with the same sputtering parameters, but with nitrogen as the discharge gas.

5.5 Surface electronic properties of ITON

Analysis of the peak shape of the detected electron core level spectra (In3d, Sn3d and O1s) provides information about distinct changes in the surface electronic structure between the different samples. The as-prepared ITON films exhibit narrow and totally symmetric peaks in XPS, while after annealing at $T \geq 600$°C the structures are broadened and become asymmetric at the high binding energy side. A representative comparison of the two different peak shapes is presented for the $In3d_{5/2}$ core level in Fig. 5.7. The changes in the O1s and $Sn3d_{5/2}$ signals are found to be identical. The asymmetry of the core levels has already been observed for ITO thin films in previous studies [143, 122, 159]. However, there is a controversy about the origin of this structure. It is known that the high conductivity of ITO films is a result of two factors: *a*) the doping effect of the incorporated Sn atoms and *b*) the formation of oxygen vacancies which both act as donors [156]. While on the one hand, the asymmetry of the core level peaks might be attributed to an additional state related to a chemical shift due to the formation of oxygen vacancies [159], on the other hand Christou et al. discuss this behavior as an additional structure caused by the conduction electron plasmon excitation [122]. In an earlier publication about ITON, the asymmetric peak shape was fitted using two Gauss-Lorentz peaks with a fixed G/L-ratio resulting in an energy separation of 0.9 eV [155]. In the following an extensive study on many different samples was performed as a function of deposition power and annealing temperature. The asymmetry of the core levels occurs for samples that have a relatively high carrier concentration. In accordance with earlier works on SnO_2 and ITO, it can be explained by a screening response, in which the Coulomb potential of the core at an ionized atom creates a localized trap state [160, 122]. In this situation, two different final states are then accessible depending on

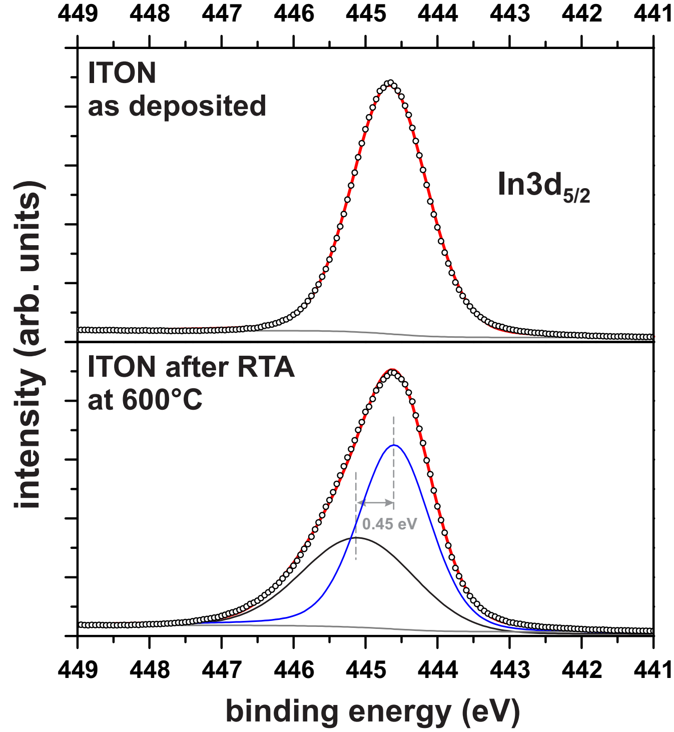

Fig. 5.7: Comparison of the $In3d_{5/2}$ peak shape of a ITON sample prior to and after rapid thermal annealing. Details of the fit parameters are discussed in the text.

whether the localized state remains empty (giving an unscreened state) or is filled by transfer of an electron from the conduction band (resulting in a screened final state). The peak shape of the unscreened state at higher binding energy is much broader compared to the screened state since it involves excitation of plasmons. This intrinsic plasmon excitation is coupled with a certain relaxation rate and therefore lifetime broadening of this contribution is expected, which results in a Lorentzian peak profile [122, 160]. Hence, the different peak shapes of both components have to be taken into account for fitting. This leads to different results compared to the first approach. The energetic separation of the components is only 0.45 eV as displayed in Fig. 5.7. In similarity to the above discussed aspects it has to be pointed out that the asymmetry in peak shape was found for as deposited and annealed ITO films as well as ITON samples that have been annealed at or above 600°C, giving one type of sample state, while untreated and 400°C RTA treated ITON films represent the other type with totally symmetric core levels peaks.
In an alternative picture the high binding energy structure corresponds to an extrinsic plasmon satellite whose Lorentzian linewidth is determined by the conduction electron scattering rate [160]. The energetic separation of these two features can be used for a rough estimation of the carrier concentration. According to the correlation between electron concentration and the bulk plasmon energy

$$\omega_p^2 = \left(\frac{ne^2}{\epsilon_\infty \epsilon_0 m^*(n)}\right) \tag{5.4}$$

n can be calculated. For the case of In_2O_3 and ITO the nonparabolicity of the conduction band has to be considered. Hence, the electron effective mass is dependent on the carrier

concentration $m^*(n)$ which can be quantitatively obtained from available band structure calculations for In_2O_3 [114]. In this way using a high frequency dielectric constant of $\epsilon_\infty = 4.0$ [122], a carrier concentration of $n = 2.1 \times 10^{20}\,cm^{-3}$ is calculated for the measured energy separation of 0.45 eV. This estimation is in very good agreement with the values obtained by Hall experiments (see Fig. 5.2) and is a further proof for the apparent changes of the ITON properties after RTA at $T \geq 600°C$. For all the ITO reference samples this asymmetry was also detected, regardless of whether they were annealed or untreated after deposition which is also consistent with the results from Hall measurements. Additionally, an effective mass of $m^* = 0.36\,m_e$ is estimated which is slightly higher compared to values obtained from optical measurements on indium tin oxide [161]. In comparison, for the as deposited ITON films with $n \sim 10^{19}\,cm^{-3}$, the effect would lead to a negligible shift of about 0.1 eV, which cannot be resolved in the present experimental setup.

For a further analysis of the electronic structure, EELS measurements have been performed on annealed ITON samples which exhibit the asymmetry in the core level peak. Fig. 5.8 presents a series of EELS scans with varying primary electron energy E_0. The left

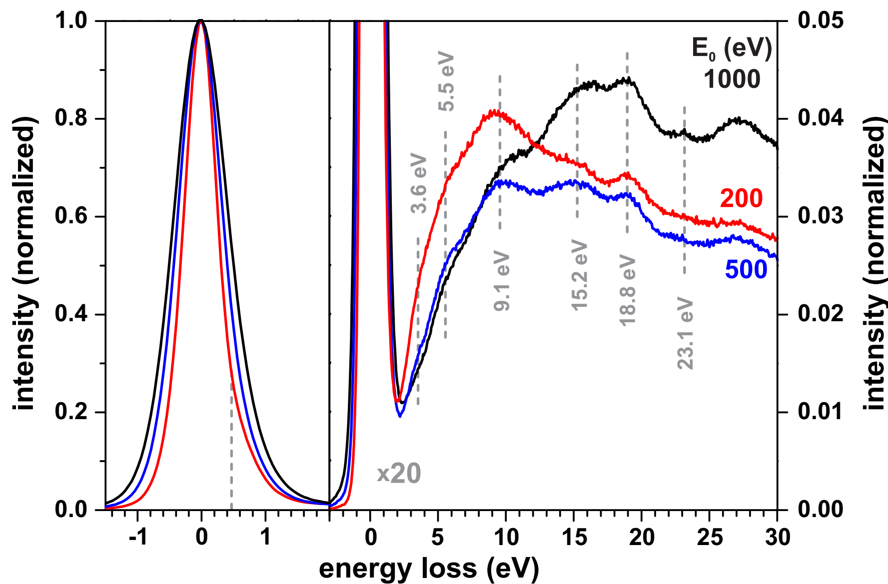

Fig. 5.8: Electron energy loss spectra of a ITON film annealed at 600°C.

side contains the signal in the energy range of the elastically reflected primary electrons. The reduction of the peak width for lower E_0 is not induced by material properties, but directly related to the dependence of the electron beam energy distribution generated by the electron source itself. A feature related to charge carrier plasmons, if present, should be visible in the EELS peak. For the originally assumed shift of 0.9 eV, no structure is found. However, there is evidence for a slight asymmetry, which is best visible in the scan obtained with $E_0 = 200\,eV$ (red curve). This could indeed be caused by an energy loss induced by excitation of charge carrier plasmons with an energy of 0.45 eV and supports the considerations on the XPS peak shape discussed above. However, for a better quantification of the carrier density from EELS, measurements with a better energy resolution are required in order to separate the plasmon signal from the elastically reflected electrons.

The high energy loss part of the EELS scans of an annealed ITON sample is presented in the right part of Fig. 5.8. In order to evaluate the origin of the different features, a comparison of measurements with different primary electron energies is useful, since this parameter allows a variation of the information depth in the measurements and hence allows a discrimination between surface and bulk effects. The dominant structures are located around 9.1 eV, 15.2 eV and 18.8 eV. The first two structures are caused by plasmon losses induced by the excitation of valence electrons, where the feature at 9.1 eV represents the surface plasmon and the one at 15.2 eV is related to excitation of electrons in the bulk [162, 163]. This statement is supported by the fact that the relative intensities change when different primary electron energies are used. When E_0 is reduced, the surface related states are typically more pronounced due to the reduced electron inelastic mean free path. The two peaks at 18.8 eV and 23.1 eV are attributed to transitions from the In4d semi-core level to unoccupied states in the conduction band (In4d $\rightarrow$ CB), consistent with measurements on indium oxide [162, 163]. Since the annealed ITON films also have a high concentration of tin at the surface, the same type of interband transitions from the Sn4d level (Sn4d $\rightarrow$ CB) also contribute to the total spectrum, in agreement with EELS results on the oxidation of Sn [164]. There are also structures at higher energy values which are mainly related to multiples and combinational losses. In addition to these well-pronounced structures, a detailed analysis of the spectra reveals that there are further features in the rising edge between 2 eV and 7 eV. Two structures at 3.6 eV and 5.5 eV are identified (best visible in the scan with $E_0 = 500$ eV), which have also been found, but not discussed in previous measurements on ITO [165]. These spectral features are due to interband transitions from occupied states in the valence band to empty conduction band states above the Fermi level E_F [163, 164].

UPS measurements reveal no clear trend in the work function of the different ITO and ITON samples. All values vary within the range of 4.2 eV $\pm$ 0.1 eV, which have been determined from the onset of the secondary electron peak. The valence band distribution of ITO and ITON samples measured using He I and He II radiation are presented in Fig. 5.9. For the ITO thin films, the valence band maximum determined by extrapolation of the trailing edge to zero is located 3.4 eV below E_F, while it is slightly shifted to 3.2 eV for the untreated and annealed ITON films. Both films exhibit structures in the valence band at 4.5 eV and 8.8 eV, comparable to indium oxide surfaces, as well as the In4d level at 18.4 eV, which agrees with the XPS results and is typical for ITO films [166]. A slight difference between ITO and ITON is detected in the energy range between 1 eV and 3 eV, which is mainly related to defect states in the band gap. For ITON, a higher signal is detected around $\sim$2.7 eV which is probably induced by the incorporated nitrogen atoms. A comparison with the valence band distribution of InN (see chapter 3 and [65]), where the first intensity maximum is located in this energy range, supports this suggestion.
Annealing of ITON at $T \geq 600°C$ also results in changes in the valence band distribution. An increase in intensity between 5 eV and 8 eV is observed with a slightly more pronounced structure at 5.8 eV. This effect can be explained by the surface segregation of tin at higher temperatures. The higher the Sn content on the surface, the more are the SnO_2-like states existent in the valence band, and located at a slightly higher binding energy relative to the In_2O_3-like states [167].

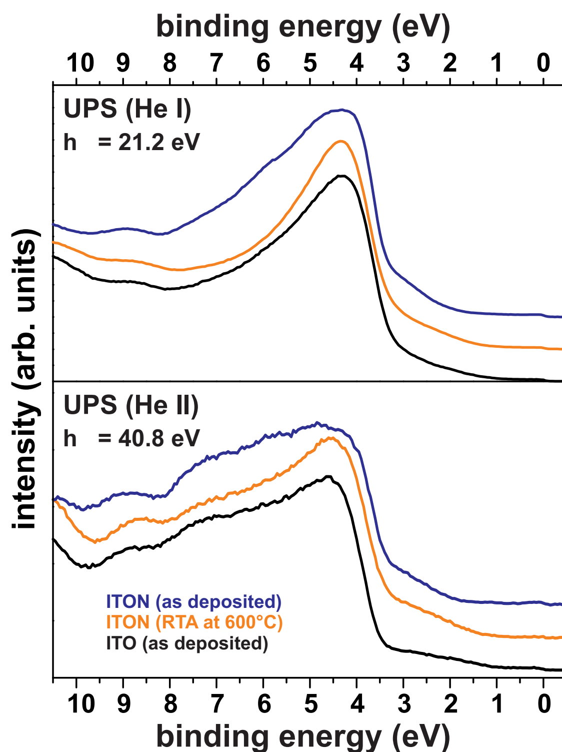

Fig. 5.9: Comparison of the valence band photoemission of ITO and ITON films measured using using He I ($h\nu = 21.2$ eV) and He II ($h\nu = 40.8$ eV) radiation.

In conclusion it can be stated that the incorporation of nitrogen during magnetron sputtering of ITO results in interesting new material properties. The changes related to the use of nitrogen as process gas could be identified to a certain degree using electron spectroscopy measurements. A correlation between the optical and electrical properties of the material to the surface properties was found. It could be directly shown that the incorporated nitrogen plays an important role in the physical properties of these ITON films. However, the thermal instability of the material has to be taken into account for any high temperature processes required for device fabrication. Nevertheless, the extended optical window of ITON after RTA could still be useful in future optoelectronic applications.

Chapter 6

Summary and Outlook

Several aspects of the dependence of preparation conditions on structural properties, surface composition as well as surface electronic structure of different indium compounds have been investigated using surface sensitive techniques such as photoelectron, Auger-electron and electron energy loss spectroscopy as well as scanning force microscopy and reflection high-energy electron diffraction. This includes in particular, the electron density of bulk and surface states of clean InN(0001) films, the properties of polycrystalline indium oxide thin films and their interaction with oxidizing gases for the implementation in ozone detectors as well as changes of the material properties due to incorporation of nitrogen into transparent, highly conductive indium tin oxide films.

Since indium nitride films are very reactive towards ambient gases, the approach to combine the MBE growth of InN(0001) films with the examination of the surface electronic structure in one UHV system was successfully followed for the first time.
A clear correlation between the In/N flux ratio and the surface stoichiometry and morphology is found. In the case of a high nitrogen supply, excess nitrogen is incorporated into the material and the growth is 3-dimensional. Additionally, the formation of a small proportion of cubic InN was noticed after growth at N-rich conditions and low substrate temperatures. The crystal quality and morphology is improved in the case of slightly In-rich growth conditions during MBE due to the accumulation of indium layers at the surface and the consequently enhanced diffusion of the reactants in this case.
For the characterization of the surface electronic structure of stoichiometric InN(0001) films, the growth parameters have been optimized in order to assure the absence of any excess material. Taking into account the low film thickness of $< 300\,\mathrm{nm}$, a good crystalline quality could be achieved. The lowest measured bulk electron concentration was $8\times10^{18}\,\mathrm{cm}^{-3}$, which is about one order of magnitude higher than the best values reported in the literature for films exceeding a thickness of $1\,\mu m$.
From the results of photoelectron spectroscopy measurements using different excitation sources, it can be stated that the measured occupied electron states of InN are in very good agreement with theoretical calculations of the bulk density of states. On the other side, for the unoccupied InN states determined from fine structures in the secondary electron cascade, a qualitative agreement between experimental and theoretical data was found, but the observed energy shift cannot be explained at present.

Depending on the growth temperature, the surface atoms tend to arrange in two different reconstructions at the InN(0001) surface: (2×2) or $(\sqrt{3} \times \sqrt{3})R30°$. Although, the $(\sqrt{3} \times \sqrt{3})R30°$ structure has been already reported in the literature, the presented results exhibit the first experimental study that determines the impacts of the formation of a surface reconstruction on the electronic properties of indium nitride. The indium adatom arrangement leads to distinct electronic states inside the band gap of InN, directly located at the Fermi edge for (2×2) reconstructed films or 0.75 eV below E_F in the case of a $(\sqrt{3} \times \sqrt{3})R30°$ structure. The experimental results agree very well with the available theoretical calculations of InN surface structures.
For stoichiometric InN films that have been examined *in-situ* after MBE growth, a strong electron accumulation is observed at the surface. In this case, oxidation of the surface due to contact with O_2 can be excluded as reason for this characteristic. The formed surface states as well as other intrinsic donor-like states have to be considered as source of electrons in the accumulation layer. Furthermore it was preliminary found that the interaction of clean InN(0001) surfaces with O_2 leads to the adsorption of oxygen, but has no influence on the valence band bending and the electron accumulation layer.

Indium oxide films were investigated in order to study the processes related to the high sensitivity of polycrystalline InOx in detecting ozone. For this purpose, the surface characteristics of externally MOCVD grown In_2O_3 layers were intensively examined depending on their crystalline properties that are mainly controlled by the temperature regime during growth.
For growth temperatures above 400°C, the resulting polycrystalline layers consist of either flat or pyramidal shaped islands, depending on the orientation of the grown film. These layers are not very sensitive towards ozone. In_2O_3 films with bixbyite structure in different orientation ((001) and (111)) or rhombohedral (0001) structure, exhibit similar chemical properties.
Careful examination of the valence band states supports the results from recently published studies that the commonly accepted band gap value of In_2O_3 of 3.6 eV is too large and the correct gap lies around 3 eV. This has also consequences on the interpretation of the surface band distribution. The reduced gap would lead to almost flat band conditions instead of the normally assumed strong upward band bending induced by an electron depletion layer at indium oxide surfaces.

Chemical vapor deposition performed at temperatures as low as 200°C using trimethylindium and water, results in the formation of porous nanocrystalline indium oxide films (particle size 7 - 8 nm) that exhibit a very high sensitivity towards ozone and can be implemented in O_3 sensors. This characteristic is mainly related to the existence of a very high density of defects at the nanocrystallite surface acting as reactive adsorption centers. The ozone sensor principle is based on the reversible adsorption of oxygen species at these reactive centers, resulting in a charge transfer from the substrate towards the adsorbate, as well as the UV radiation or thermally induced desorption which results in a strong variation of the film resistance.
After O_3 oxidation, an unexpected shift of the valence band away from the Fermi level is detected, although the electrical characteristics point towards a reduction of the carrier

concentration. Based upon the photoelectron spectroscopy data, a model is proposed that explains the observations by an altered band gap at the vicinity of the surface, which is induced by the adsorption of oxygen species.
The interaction with O_3 is based on the dissociation of the molecule and adsorption in the form of negatively charged oxygen ions due to electron transfer from the indium oxide towards the adsorbate. The same adsorbate is formed when the surface comes into contact with water. This observation explains the reduced sensitivity of the ozone sensor devices, when operated under humid conditions.

The incorporation of nitrogen into indium tin oxide by rf magnetron sputtering in N_2 atmosphere was characterized by X-ray photoelectron spectroscopy. Depending on the used plasma power, up to 10% of nitrogen is inserted into the films, which is bound in different chemical states. The formation of N-In, N-Sn as well as N-O bonds was verified. Additionally, a large portion of the incorporated nitrogen is inserted into the films without forming chemical bonds with indium, tin or oxygen. In accordance to studies on the nitridation of InP, InAs and InSb, this phase is attributed to nitrogen that is embedded at interstitial sites.
The incorporation of nitrogen leads to a decoration of oxygen vacancies in the material and consequently to a reduction of the electron concentration by about one order of magnitude compared to conventional Ar-sputtered ITO films.
As for all indium compounds, the thermal instability of the material is one major aspect of the properties of these materials. The inserted nitrogen desorbs out of the film above 550°C. Simultaneously the segregation of tin towards the surface occurs. Both processes result in a strong increase in the carrier concentration in the material. Hence, post-processing by rapid thermal annealing leads to improved electrical properties (higher conductivity and high electron mobility). As a consequence, the optical transmission in the near UV region is increased for ITON films compared to conventionally Ar sputtered ITO films.

The performed investigations resulted in new insights to open questions about the properties of indium compounds. Nevertheless, there are still many unsolved problems that require further studies on these materials.
The achieved experience in the preparation of clean and well-defined InN surfaces with pronounced reconstructions allows even deeper fundamental investigations on this special semiconductor. For this purpose, further improvement of the material properties (especially crystallinity, morphology and electron concentration) will be crucial and is expected to be realized by increasing the thickness of the grown films. Especially smooth surfaces would allow angle-dependent photoelectron spectroscopy measurements in order to map the k-dependence of the electronic states. Furthermore, examination of the local structural and electric properties by scanning tunneling microscopy/spectroscopy measurements is encouraged.
The realized capability for *in-situ* characterization of MBE grown films allows further studies of the initial stages of interaction with different atoms or molecules in order to investigate surface reactions on an atomic level, which is not possible on samples that have been

exposed to ambient conditions. This would include extensive studies on the influence of different adsorbates, such as alkali-atoms or gaseous materials.
In particular, for the consideration of indium nitride based transistor devices, characterization of interface and band alignment properties of InN towards possible gate and contact materials will be one important task for future experiments. The technological equipment in the ZMN facilitates these measurements and especially the study of the InN/In_2O_3 interface can be relatively easy realized in the UHV growth and surface analysis system.
The investigation of the surface electronic structure should be further expanded to N-polarity or non-polar InN films that can be grown on special substrates. Of great importance is a confirmation or exclusion of the theoretically predicted absence of the electron accumulation layer at a- and m-plane InN surface prepared under stoichiometric conditions.

Surface studies on defect rich nanocrystalline indium oxide films enabled a qualitative description of the processes related to ozone oxidation and UV-induced reduction of the surface. The presented measurements were performed close to the actual environment the sensor surfaces are exposed to during operation. However, these investigations can only in parts contribute to an overall description of the underlying processes that define the ozone sensor characteristics. This is related to the complexity of the system, where several aspects have to be considered such as the structural, compositional and electronic features of the films. It is worth to study several aspects separately in order to distinguish between the different influences. This includes to switch to epitaxial or single crystal In_2O_3 surfaces for the examination of the surface reactions, and to define reference experiments as is typically done in studies on catalytic materials. For the gas interaction processes, coverage-dependent surface spectroscopy measurements will refine the proposed models and are encouraged for the near future. Especially the implementation of extremely adsorbate sensitive experimental techniques such as high-resolution electron energy loss spectroscopy and metastable impact electron spectroscopy are expected to give further insight into the dissociation processes of ozone and water at the surface.
It has to be mentioned that the performed experiments as well as the measurements proposed for the future strongly rely on theoretical studies of possible stable adsorbate configurations on In_2O_3 surfaces. Hopefully, the progress in computation speed as well as theoretical approaches result in supporting information on the surface properties of the complex system indium oxide in the near future.

The presented studies have established a better knowledge of the surface properties of InN(0001), polycrystalline indium oxide as well as indium tin oxynitride thin films. Most of the aspects discussed here are of fundamental character and do not directly lead into new (opto)electronic applications. However, the results can contribute to a better basic understanding of indium compounds and help to conceive the fundamental material characteristics as well as processes during film preparation or device operation.
Hopefully, some of these indium based materials will lead to improvement of existing or to even new devices in the near future. The transfer from first demonstrators to the realization of commercial LT-InOx based ozone sensors, would give the chance for a wide-range

control of the O_3 concentration in the environment and prevent people to be exposed to harmful doses. Indium nitride based applications are still a perspective, but large efforts are put into the study and development of e.g. extremely fast transistors as well as terahertz emitters. A successful implementation of the material requires further improvement of the film quality and the recently started transition from pure material properties based studies towards applied investigations.

Perspectively, the implementation of annealed ITON layers could improve the performance of devices that rely on transparent conductive oxides, since the window of transparency can be shifted further into the UV. Special impact is expected on the quality of ohmic contacts on p-type nitride films, since the incorporated nitrogen can lead to improved interface properties upon annealing.

Bibliography

[1] J.E. Ayers. *Heteroepitaxy of Semiconductors - Theory, Growth and Characterization.* CRC Press, 2007.

[2] K. Oura, V.G. Lifshits, A.A. Saranin, A.V. Zotov, and M. Katayama. *Surface Science - An Introduction.* Advanced Texts in Physics. Springer, 2003.

[3] A. Ichimiya and P.I. Cohen. *Reflection high-energy electron diffraction.* Cambridge University Press, 2004.

[4] W. Braun. *Applied RHEED - Reflection High-Energy Electron Diffraction During Crystal Growth.* Springer, 1999.

[5] M. Cardona and L. Ley. *Photoemission in Solids, General Principles*, volume 26 of *Topics in Applied Physics.* Springer Verlag, Berlin, 1978.

[6] D. Briggs and M.P. Seah. *Auger and X-ray Photoelectron Spectroscopy*, volume 1 of *Practical Surface Analysis.* John Wiley & Sons, New York, 2nd edition, 1990.

[7] S. Hüfner. *Photoelectron Spectroscopy, Principles and Applications*, volume 82 of *Springer Series in Solid-State Sciences.* Springer Verlag, Berlin, 1996.

[8] M. Henzler and W. Göpel. *Oberflächenphysik des Festkörpers.* Teubner, Stuttgart, 2nd edition, 1994.

[9] M.P. Seah and W.A. Dench. Quantitative Electron Spectroscopy of Surfaces: A Standard Data Base for Electron Mean Free Paths in Solids. *Surface and Interface Analysis*, 1(1):2–11, 1979.

[10] S. Tanuma, C.J. Powell, and D.R. Penn. *Surf. Interface Anal.*, 20:77, 1993.

[11] J.J. Yeh and I. Lindau. *Atomic Data and Nuclear Data Tables*, 32:1, 1985.

[12] W. Mönch. *Semiconductor Surfaces and Interfaces*, volume 26 of *Springer Series in Surface Science.* Springer, 3rd edition, 2001.

[13] R.E. Thomas, A. Shih, and G.A. Haas. *Surf. Sci.*, 75:239, 1978.

[14] J. Schäfer, R. Schoppe, J. Hölzl, and R. Feder. *Surf. Sci.*, 107:290, 1981.

[15] T. Takahashi, H. Tokailin, and T. Sagawa. *Phys. Rev. B*, 32:8317, 1985.

[16] H. Lüth. *Surfaces and Interfaces of Solids.* Springer, 1993.

[17] V.M. Polyakov, A. Elbe, J. Wu, G.J. Lapeyre, and J.A. Schaefer. *Phys. Rev. B*, 54:2010, 1996.

[18] T. Balster. *Untersuchungen an reinen und mit Wasserstoff bedeckten SiC(100)-Oberflächen mit Hochaufgelöster Elektonenenergieverlususpektroskopie.* Dissertation, Institute of Physics, TU Ilmenau, 1999.

[19] X-ray Monochromators XM500 and XM1000 users guide, Version 2.2. Omicron Nanotechnology GmbH, 2003.

[20] Instruction Manual VUV Discharge Lamp HIS13, Version 1.7. Focus GmbH (Omicron), 1996.

[21] D. Sarid. *Scanning Force Microscopy.* Oxford University Press, 1994.

[22] R. Wiesendanger (ed.). *Scanning Probe Microscopy.* Nanoscience and Technology. Springer, 1998.

[23] M. Himmerlich. *Photoelectron Emission Microscopy and Photoelectron Spectroscopy of Ge on Si, InN and InP.* Diplom thesis, Institute of Physics, TU Ilmenau, 2005.

[24] H. Morkoç. *Handbook of Nitride Semiconductors and Devices*, volume 1-3. Wiley-VCH, 2008.

[25] M.S. Shur S.K. O'Leary, B.E. Foutz and L.F. Eastman. *Appl. Phys. Lett.*, 87:222103, 2005.

[26] V.M. Polyakov and F. Schwierz. *Appl. Phys. Lett.*, 88:032101, 2006.

[27] T.L. Tansley and C. Foley. *J. Appl. Phys.*, 59:3241, 1986.

[28] A. Wakahara, T. Tsuchia, and A. Yoshida. *J. Cryst. Growth*, 99:385, 1990.

[29] W.E. Hoke, P.J. Lemonias, and D.G. Weir. *J. Cryst. Growth*, 111:1024, 1991.

[30] S. Yamaguchi, M. Kariya, S. Nitta, T. Takeuchi, C. Wetzel, H. Amano, and I. Akasaki. *J. Appl. Phys.*, 85:7682, 1999.

[31] H. Lu, W.J. Schaff, J. Hwang, H. Wu, W. Yeo, A. Pharkya, and L.F. Eastman. *Appl. Phys. Lett.*, 77:2548, 2000.

[32] B. Maleyre, O. Briot, and S. Ruffenach. *J. Cryst. Growth*, 269:15, 2004.

[33] C.H. Swartz, R.P. Tomkins, T.H. Myers, H. Lu, and W.J. Schaff. *phys. stat. sol. (c)*, 2:2250, 2005.

[34] V. Lebedev, V. Cimalla, J. Pezoldt, M. Himmerlich, S. Krischok, J.A. Schaefer, O. Ambacher, F.M. Morales, J.G. Lozano, and D. González. *J. Appl. Phys.*, 100:094902, 2006.

[35] J. Wu and W. Walukiewicz. *Superlattices Microstruct.*, 34:63, 2003.

[36] K.S.A. Butcher and T.L. Tansley. *Superlattices Microstruct.*, 38:1, 2005.

[37] B. Monemar, P.P. Paskov, and A. Kasic. *Superlattices Microstruct.*, 38:38, 2005.

[38] V.Y. Davydov, A.A. Klochikhin, R.P. Seisyan, V.V. Emtsev, S.V. Ivanov SV, F. Bechstedt, J. Furthmüller, H. Harima, V. Mudryi, J. Aderhold, O. Semchinova, and J. Graul. *phys. stat. sol. (b)*, 229:R1, 2002.

[39] W. Walukiewicz, J.W. Ager, K.M. Yu, Z. Liliental-Weber, J. Wu, S.X. Li, R.E. Jones, and J.D. Denlinger. *J. Phys. D*, 39:R83, 2006.

[40] R. Goldhahn, P. Schley, A.T. Winzer, G. Gobsch, V. Cimalla, O. Ambacher, M. Rakel, C. Cobet, N. Esser, H. Lu, and W.J. Schaff. *phys. stat. sol (a)*, 203:42, 2006.

[41] J. Furthmüller, P.H. Hahn, F. Fuchs, and F. Bechstedt. *Phys. Rev. B*, 72:205106, 2005.

[42] D. Fritsch, H. Schmidt, and M. Grundmann. *Phys. Rev. B*, 69:165204, 2004.

[43] V. Cimalla, V. Lebedev, F.M. Morales, R. Goldhahn, and O. Ambacher. *Appl. Phys. Lett.*, 89:172109, 2006.

[44] Y.-S. Lin, S.-H. Koa, C.-Y. Chan, S.S.H. Hsu, H.-M.Lee, and S. Gwo. *Appl. Phys. Lett.*, 90:142111, 2007.

[45] E. Trybus, G. Namkoong, W. Henderson, S. Burnham, W.A. Doolittle, M. Cheung, and A. Cartwright. *J. Cryst. Growth*, 288:218, 2006.

[46] H. Lu, W.J. Schaff, and L.F. Eastman. *J. Appl. Phys.*, 96:3577, 2004.

[47] R. Ascazubi, I. Wilke, K. Denniston, H. Lu, and W.J. Schaff. *Appl. Phys. Lett.*, 84:4810, 2004.

[48] G.D. Chern, E.D. Readinger, H.G. Shen, M. Wraback, C.S. Gallinat, G. Koblmüller, and J.S. Speck. *Appl. Phys. Lett.*, 89:141115, 2006.

[49] K.A. Rickert, A.B. Ellis, F.J. Himpsel, H. Lu, W. Schaff, J.M. Redwing, F. Dwikusuma, and T.F. Kuech. *Appl. Phys. Lett.*, 82:3254, 2003.

[50] S. Krischok, V. Yanev, O. Balykov, M. Himmerlich, J.A. Schaefer, R. Kosiba, G. Ecke, I. Cimalla, V. Cimalla, O. Ambacher, H. Lu, W.J. Schaff, and L.F. Eastman. *Surf. Sci.*, 566-568:849, 2004.

[51] L.F.J. Piper, T.D. Veal, M. Walker, I. Mahboob, C.F. McConville, H. Lu, and W.J. Schaff. *J. Vac. Sci. Technol. A*, 23:617, 2005.

[52] T.D. Veal, P.D.C. King, P.H. Jefferson, L.F.J. Piper, C.F. McConville, H. Lu, W.J. Schaff, P.A. Anderson, S.M. Durbin, D. Muto, H. Naoi, and Y. Nanishi. *Phys. Rev. B*, 76:075313, 2007.

[53] L.F.J. Piper, T.D. Veal, P.H. Jefferson, C.F. McConville, F. Fuchs, J. Furthmüller, F. Bechstedt, H. Lu, and W.J. Schaff. *Phys. Rev. B*, 72:245319, 2005.

[54] M. Draxler, M. Walker, and C.F. McConville. *Nucl. Instrum. Methods Phys. Res. B*, 249:886, 2006.

[55] I. Mahboob, T.D. Veal, C.F. McConville, H. Lu, and W.J. Schaff. *Phys. Rev. Lett.*, 92:036804, 2004.

[56] T.D. Veal, L.F.J. Piper, I. Mahboob, H. Lu, W.J. Schaff, and C.F. McConville. *phys. stat. sol. (c)*, 2:2246, 2005.

[57] H. Lu, W.J. Schaff, L.F. Eastman, and C.E. Stutz. *Appl. Phys. Lett.*, 82:1736, 2003.

[58] C.G. Van de Walle and J. Neugebauer. *Nature*, 423:626, 2003.

[59] S.X. Li, K.M. Yu, J. Wu, R.E. Jones, W. Walukiewicz, J.W. Ager, W. Shan, E.E. Haller, H. Lu, and W.J. Schaff. *Phys. Rev. B*, 71:161201, 2005.

[60] P.D.C. King, T.D. Veal, P.H. Jefferson, S.A. Hatfield, L.F.J. Piper, C.F. McConville, F. Fuchs, J. Furthmüller, F. Bechstedt, H. Lu, and W.J. Schaff. *Phys. Rev. B*, 77:045316, 2008.

[61] D. Segev and C.G. Van de Walle. *Europhys. Lett.*, 76:305, 2006.

[62] C.G. Van de Walle and David Segev. *J. Appl. Phys.*, 101:081704, 2007.

[63] P.D.C. King, T. D. Veal, C.F. McConville, F. Fuchs, J. Furthmüller, F. Bechstedt, P. Schley, R. Goldhahn, J. Schörmann, D.J. As, K. Lischka, D. Muto, H. Naoi, Y. Nanishi, H. Lu, and W.J. Schaff. *Appl. Phys. Lett.*, 91:092101, 2007.

[64] E. Calleja, J. Grandal, M.A. Sánchez-García, M. Niebelschütz, V. Cimalla, and O. Ambacher. *Appl. Phys. Lett.*, 90:262110, 2007.

[65] M. Himmerlich, S. Krischok, V. Lebedev, O. Ambacher, and J.A. Schaefer. *J. Cryst. Growth*, 306:6, 2007.

[66] V. Cimalla, M. Niebelschütz, G. Ecke, V. Lebedev, O. Ambacher, M. Himmerlich, S. Krischok, J.A. Schaefer, H. Lu, and W.J. Schaff. *phys. stat. sol. (a)*, 203:59, 2006.

[67] R.E. Jones, K.M. Yu, S.X. Li, W. Walukiewicz, J.W. Ager, E.E. Haller, H. Lu, and W.J. Schaff. *Phys. Rev. Lett.*, 96:125505, 2006.

[68] A. Eisenhardt. *Molekularstrahlepitaxie und Oberflächenanalyse von In-polarem InN.* Diplom thesis, Institute of Physics, TU Ilmenau, 2008.

[69] E. Dimakis, E. Iliopoulos, K. Tsagaraki, and A. Georgakilas. *Appl. Phys. Lett.*, 86:133104, 2005.

[70] E. Dimakis, E. Iliopoulos, K. Tsagaraki, and A. Georgakilas. *phys. stat. sol. (a)*, 203:1686, 2006.

[71] C.S. Gallinat, G. Koblmüller, J.S. Brown, and J.S. Speck. *J. Appl. Phys.*, 102:064907, 2007.

[72] D. Segev and C.G. Van de Walle. *Surf. Sci. Lett.*, 601:L15, 2007.

[73] K.S.A. Butcher, A.J. Fernandes, P.P.-T.Chen, M. Wintrebert-Fouquet, H. Timmers, S.K. Shrestha, H. Hirshy, R.M. Perks, and B.F. Usher. *J. Appl. Phys.*, 101:123702, 2007.

[74] Y.G. Cao, S.H. Xu, W. Lü, X.Q. Dai, Y.F. Chan, N. Wang, Y. Liu, H.S. Wu, M.H. Xie, and S.Y. Tong. *Phys. Rev. B*, 71:155322, 2005.

[75] C.K. Gan and D.J. Srolovitz. *Phys. Rev. B*, 74:115319, 2006.

[76] V. Cimalla, Ch. Förster, G. Kittler, I. Cimalla, R. Kosiba, G. Ecke, O. Ambacher, R. Goldhahn, S. Shokhovets, A. Georgakilas, H. Lu, and W.J. Schaff. *phys. stat. sol. (c)*, 0:2818, 2003.

[77] E. Dimakis, E. Iliopoulos, K. Tsagaraki, A. Adikimenakis, and A. Georgakilas. *Appl. Phys. Lett.*, 88:191918, 2006.

[78] P. Schley, R. Goldhahn, A.T. Winzer, G. Gobsch, V. Cimalla, O. Ambacher, H. Lu, W.J. Schaff, M. Kurouchi, Y. Nanishi, M. Rakel, C. Cobet, and N. Esser. *Phys. Rev. B*, 75:205204, 2007.

[79] R. Goldhahn. *Acta Phys. Pol. A*, 104:123, 2003.

[80] L.F.J. Piper, T.D. Veal, I. Mahboob, C.F. McConville, H. Lu, and W.J. Schaff. *Phys. Rev. B*, 70:115333, 2004.

[81] R.P. Bhatta, B.D. Thoms, M. Alevli, and N. Dietz. *Surf. Sci. Lett.*, 601:L120, 2007.

[82] K. Klöckner, V. Polyakov, M. Himmerlich, A. Eisenhardt, R.J. Koch, S.I.-U. Ahmed, S. Krischok, and J.A. Schaefer. *Accumulation layer density profile and bulk electron concentration of MBE grown InN(0001)* (to be published).

[83] P.D.C. King, T.D. Veal, C.F. McConville, F. Fuchs, J. Furthmüller, F. Bechstedt, J. Schörmann, D.J. As, K. Lischka, H. Lu, and W.J. Schaff. *Phys. Rev. B*, 77:115213, 2008.

[84] M. Rakel, C. Cobet, N. Esser, F. Fuchs, F. Bechstedt, R. Goldhahn, W.G. Schmidt, and W.J. Schaff. *Phys. Rev. B*, 77:115120, 2008.

[85] L.F.J. Piper, L. Colakerol, T. Learmonth, P.-A. Glans, K.E. Smith, F. Fuchs, J. Furthmüller, F. Bechstedt, T.-C. Chen, T.D. Moustakas, and J.-H. Guo. *Phys. Rev. B*, 76:245204, 2007.

[86] F. Fuchs, J. Furthmüller, F. Bechstedt, M. Shishkin, and G. Kresse. *Phys. Rev. B*, 76:115109, 2007.

[87] D. Segev, A. Janotti, and C.G. Van de Walle. *Phys. Rev. B*, 75:035201, 2007.

[88] F. Fuchs. private communication.

[89] D. Muto, T. Araki, H. Naoi, F. Matsuda, and Y. Nanishi. *phys. stat. sol. (a)*, 202:773, 2005.

[90] R. Gutt. *Plasma Assisted Molecular Beam Epitaxy of Gallium Nitride on Silicon Carbide Substrates.* Diplom thesis, Institute of Physics, TU Ilmenau, 2008.

[91] T.D. Veal, P.D.C. King, M. Walker, C.F. McConville, H. Lu, and W.J. Schaff. *Physica B*, 401-402:351, 2007.

[92] S.-H. Lee, Y.-S. Kim, and Y.-C. Chung. *Jap. J. Appl. Phys.*, 46:6205, 2007.

[93] V. Lebedev, Ch. Y. Wang, V. Cimalla, S. Hauguth, T. Kups, M. Ali, G. Ecke, M. Himmerlich, S. Krischok, J.A. Schaefer, O. Ambacher, V. M. Polyakov, and F. Schwierz. *J. Appl. Phys.*, 101:123705, 2007.

[94] T. Seiyama (ed.). *Chemical Sensor Technology.* Elsevier, 1988-1991.

[95] M. Batzill and U. Diebold. *Phys. Chem. Chem. Phys.*, 9:2307, 2007.

[96] N. Barsan and U. Weimar. *J. Electroceram.*, 7:143, 2001.

[97] M.Z. Atashbar, B. Gong, H.T. Sun, W. Wlodarski, and R. Lamb. *Thin Solid Films*, 354:222, 1999.

[98] M. Bender, N. Katsarakis, E. Gagaoudakis, E. Hourdakis, E. Douloufakis, V. Cimalla, and G. Kiriakidis. *J. Appl. Phys.*, 90:5382, 2001.

[99] M. Epifani, E. Comini, J. Arbiol, E. Pellicer, P. Siciliano, G. Faglia, and J.R. Morante. *J. Phys. Chem. C*, 111:13967, 2007.

[100] Ch.Y. Wang, V. Cimalla, Th. Kups, C.-C. Röhlig, H. Romanus, V. Lebedev, J. Pezoldt, Th. Stauden, and O. Ambacher. *J. Appl. Phys.*, 102:044310, 2007.

[101] D. Lutic, M. Strand, A. Lloyd-Spetz, K. Buchholt, E. Ieva, P.-O. Kall, and M. Sanati. *Top. Catal.*, 45:105, 2007.

[102] A. Gurlo, N. Barsan, M. Ivanovskaya, U. Weimar, and W. Göpel. *Sens. Actuators B*, 47:92, 1998.

[103] M. Ali, Ch.Y. Wang, C.C. Roehlig, V. Cimalla, T. Stauden, and O. Ambacher. *Sens. Actuators B*, 129:467, 2008.

[104] G. Neri, A. Bonavita, G. Micali, G. Rizzo, N. Pinna, M. Niederberger, and J. Ba. *Sens. Actuators B*, 130:222, 2008.

[105] G. Korotcenkov, I. Boris, V. Brinzari, V. Golovanov, Y. Lychkovsky, G. Karkotsky, A. Cornet, E. Rossinyol, J. Rodrigue, and A. Cirera. *Sens. Actuators B*, 103:13, 2004.

[106] V.E. Henrich and P.A. Cox. *The Surface Science of Metal Oxides.* Cambridge University Press, 1994.

[107] H.H. Kung. *Transition metal oxides: surface chemistry and catalysis.* Elsevier, 1991.

[108] M. Batzill and U. Diebold. *Prog. Surf. Sci.*, 79:47, 2005.

[109] A. Klein. *Appl. Phys. Lett.*, 77:2009, 2000.

[110] V. Brinzari, G. Korotcenkov, and V. Matolin. *Appl. Surf. Sci.*, 243:335, 2005.

[111] V. Brinzari, G. Korotcenkov, M. Ivanov, V. Nehasil, V. Matolin, K. Masek, and M. Kamei. *Surf. Sci.*, 601:5585, 2007.

[112] Inorganic crystal structure database. Fachinformationszentrum Karlsruhe, 2002.

[113] S.Zh. Karazhanov, P. Ravindran, P. Vajeeston, A. Ulyashin, T.G. Finstad, and H. Fjellvåg. *Phys. Rev. B*, 76:075129, 2007.

[114] F. Fuchs and F. Bechstedt. *Phys. Rev. B*, 77:155107, 2008.

[115] Ch.Y. Wang, V. Cimalla, H. Romanus, Th. Kups, G. Ecke, Th. Stauden, M. Ali, V. Lebedev, J. Pezoldt, and O. Ambacher. *Appl. Phys. Lett.*, 89:011904, 2006.

[116] F. Matino, L. Persano, V. Arima, D. Pisignano, R.I.R. Blyth, R. Cingolani, and R. Rinaldi. *Phys. Rev. B*, 72:085437, 2005.

[117] A. Walsh, J.L.F. Da Silva, S.-H. Wei, C. Körber, A. Klein, L.F.J. Piper, A. DeMasi, K.E. Smith, G. Panaccione, P. Torelli, D.J. Payne, A. Bourlange, and R.G. Egdell. *Phys. Rev. Lett.*, 100:167402, 2008.

[118] Ch.Y. Wang, V. Lebedev, V. Cimalla, Th. Kups, K. Tonisch, and O. Ambacher. *Appl. Phys. Lett.*, 90:221902, 2007.

[119] Ch.Y. Wang, Y. Dai, J. Pezoldt, B. Lu, Th. Kups, V. Cimalla, and O. Ambacher. *Cryst. Growth Des.*, 8:1257, 2008.

[120] P. Erhart, A. Klein, R.G. Egdell, and K. Albe. *Phys. Rev. B*, 75:153205, 2007.

[121] T.L. Barr and Y.L. Liu. *J. Phys. Chem. Solids*, 50:657, 1989.

[122] V. Christou, M. Etchells, O. Renault, P.J. Dobson, O.V. Salata, G. Beamson, and R.G. Egdell. *J. Appl. Phys.*, 88:5180, 2000.

[123] Y. Gassenbauer, R. Schafranek, and A. Klein. *Phys. Rev. B*, 73:245312, 2006.

[124] V. Golovanov, M.A. Maki-Jaskari, T.T Rantala, G. Korotcenkov, V. Brinzari, A. Cornet, and J. Morante. *Sens. Actuators B*, 106:563, 2005.

[125] J. Massies and F. Lemaire-Dezaly. *J. Appl. Phys.*, 57:237, 1985.

[126] G. Beamson and D. Briggs. *High Resolution XPS of Organic Polymers - The Scienta ESCA300 Database.* Wiley, 1992.

[127] T.S. Fischer, N. Eisenreich, and A. Pfeil. *Thermochim. Acta*, 339:35, 1999.

[128] J.F. Moulder, W.F. Stickle, P.E. Sobol, and K.D. Bomben. *Handbook of X-ray Photoelectron Spectroscopy.* Physical Electronics, Inc., 1995.

[129] Ch.Y. Wang. *Metal organic chemical vapor deposition of indium oxide for ozone sensing.* Dissertation, Albert-Ludwigs-Universität Freiburg, submitted 2008.

[130] C. Malagu, G. Martinelli, M.A. Ponce, and C.M. Aldao. *Appl. Phys. Lett.*, 92:162104, 2008.

[131] B. Pujilaksono, U. Klement, L. Nyborg, U. Jelvestam, S. Hill, and D. Burgard. *Mater. Charact.*, 54:1, 2005.

[132] M. Mizuno, T. Miyamoto, T. Ohnishi, and H. Hayashi. *Jpn. J. Appl. Phys.*, 36:3408, 1997.

[133] I. Tanaka, F. Oba, K. Tatsumi, M. Kunisu, M. Nakano, and H. Adachi. *Mater. Trans.*, 43:1426, 2002.

[134] S. Krischok. *Wechselwirkung zwischen TiO_2-Oberflächen und verschiedenen Adsorbatatomen und -molekülen.* Dissertation, TU Clausthal, 2001.

[135] A.L. Dawar and J.C. Joshi. *J. Mater. Sci.*, 19:1, 1993.

[136] H. Kim, J.S. Horwitz, G. Kushti, A. Pique, Z.H. Kafafi, and C.M. Gilmore. *J. Appl. Phys.*, 88:6021, 2000.

[137] S.S. Kim, S.Y. Choi, C.G. Park, and H.W. Jin. *Thin Solid Films*, 347:155, 1999.

[138] N. Al-Dahoudi, H. Bisht, C. Gobbert, T. Krajewski, and M.A. Aegerter. *Thin Solid Films*, 392:299, 2001.

[139] T. Margalith, O. Buchinsky, D.A. Cohen, A.C. Abave, M. Hansen, S.P. DenBaars, and L.A. Coldren. *Appl. Phys. Lett.*, 74:3930, 1999.

[140] S.-H. Su, C.-C. Hou, M. Yokoyama, and S.-M. Chen. *J. Electrochem. Soc.*, 153:G87, 2006.

[141] E. Aperathitis, M. Bender, V. Cimalla, G. Ecke, and M. Modreanu. *J. Appl. Phys.*, 94:1258, 2003.

[142] E. Aperathitis, M. Modreanu, M. Bender, V. Cimalla, G. Ecke, M. Androulidaki, and N. Pelekanos. *Thin Solid Films*, 450:101, 2004.

[143] J.S. An, S.C. Kim, S.H. Hahn, S.K. Ko, and E.J. Kim. *J. Korean Phys. Soc.*, 45:1629, 2004.

[144] R.X. Wang, C.D. Beling, A.B. Djurišić, S. Li, and S. Fung. *Semicond. Sci. Technol.*, 19:695, 2004.

[145] Y.-J. Lin, Y.-M. Chen, and Y.-C.Wang. *J. Appl. Phys.*, 97:083702, 2005.

[146] J.H. Choi, E.S. Lee, S.H. Choi, H.K. Baik, K.M. Song, Y.S. Lim, and S.-M. Lee. *J. Vac. Sci. Technol. A*, 23:1479, 2005.

[147] W. Song, S.K. So, and L. Cao. *Appl. Phys. A*, 72:361, 2001.

[148] W. Song, S.K. So, D. Wang, Y. Qiu, and L. Cao. *Appl. Surf. Sci.*, 177:158, 2001.

[149] M. Himmerlich, M. Koufaki, M. Sifakis, S. Krischok, G. Ecke, Ch. Mauder, V. Cimalla, J.A. Schaefer, A. Kondilis, N. Pelekanos, M. Modreanu, and E. Aperathitis. *Investigation on the properties of Indium-Tin-Oxynitride films as ohmic contact for GaN based optoelectronic devices* (to be submitted).

[150] Y. Bu, L. Ma, and M.C. Lin. *J. Vac. Sci. Technol. A*, 11:2931, 1993.

[151] Y. Inoue, M. Nomiya, and O. Takai. *Vacuum*, 51:673, 1998.

[152] I. Bello, W.M. Lau, R.P.W. Lawson, and K.K. Foo. *J. Vac. Sci. Technol. A*, 10:1642, 1992.

[153] J.-D. Hecht, F. Frost, D. Hirsch, H. Neumann, A. Schindler, A.B. Preobrajenski, and T. Chassé. *J. Appl. Phys.*, 90:6066, 2001.

[154] J.-D. Hecht, F. Frost, Th. Chassé, D. Hirsch, H. Neumann, A. Schindler, and F. Bigl. *Appl. Surf. Sci.*, 179:196, 2001.

[155] M. Himmerlich, M. Koufaki, Ch. Mauder, G. Ecke, V. Cimalla, J.A. Schaefer, E. Aperathitis, and S. Krischok. *Surf. Sci.*, 601:4082, 2007.

[156] G.B. Gonzalez, T.O. Mason, J.P. Quintana, O. Warschkow, D.E. Ellis, J.-H. Hwang, J.P. Hodges, and J.D. Jorgensen. *J. Appl. Phys.*, 96:3912, 2004.

[157] T.D. Lowes and M. Zinke-Allmang. *Phys. Rev. B*, 49:16678, 1994.

[158] A. Rogozin, N. Shevchenko, M. Vinnichenko, F. Prokert, V. Cantelli, A. Kolitsch, and W. Möller. *Appl. Phys. Lett.*, 85:212, 2004.

[159] R.X. Wang, C.D. Beling, S. Fung, A.B. Djurišić, C.C. Ling, and S. Li. *J. Appl. Phys.*, 97:033504, 2005.

[160] R.G. Egdell, T.J. Walker, and G. Beamson. *J. Electron Spectrosc. Relat. Phenom.*, 128:59, 2003.

[161] H. Fujiwara and M. Kondo. *Phys. Rev. B*, 71:075109, 2005.

[162] D.-X. Dai, F.-R. Zhu, I. Davoli, and S. Stizza. *Appl. Surf. Sci.*, 59:195, 1992.

[163] H. Öfner, Y. Shapira, and F.P. Netzer. *J. Appl. Phys.*, 76:1196, 1994.

[164] G.B. Hoflund and G.R. Corallo. *Phys. Rev. B*, 46:7110, 1992.

[165] F. Zhu, C.H.A. Huan, K. Zhang, and A.T.S. Wee. *Thin Solid Films*, 359:244, 2000.

[166] K. Sugiyama, H. Ishii, Y. Ouchi, and K. Seki. *J. Appl. Phys.*, 87:295, 2000.

[167] M. Batzill, K. Katsiev, J.M. Burst, and U. Diebold. *Phys. Rev. B*, 72:165414, 2005.

Appendix A

Abbreviations and Symbols

AES	**A**uger-**E**lectron **S**pectroscopy
AFM	**A**tomic **F**orce **M**icroscopy
AHC	**A**tomic **H**ydrogen **C**leaning
CB(M)	**C**onduction **B**and (**M**inimum)
DOS	**D**ensity **o**f **S**tates
E_B	**B**ranch point **E**nergy
E_F	**F**ermi **E**nergy
E_{Vac}	**V**acuum **E**nergy
FWHM	**F**ull **W**idth at **H**alf **M**aximum
(HR)EELS	(**H**igh-**R**esolution) **E**lectron **E**nergy **L**oss **S**pectroscopy
IMFP	**I**nelastic **M**ean **F**ree **P**ath
LEED	**L**ow **E**nergy **E**lectron **D**iffraction
MBE	**M**olecular **B**eam **E**pitaxy
MIES	**M**etastable **I**mpact **E**lectron **S**pectroscopy
MOCVD	**M**etal **O**rganic **C**hemical **V**apor **D**eposition
PEEM	**P**hoto **E**lectron **E**mission **M**icroscopy
PES	**P**hoto **E**lectron **S**pectroscopy
QMS	**Q**uadrupole **M**ass **S**pectroscopy
RGA	**R**esidual **G**as **A**nalysis
RHEED	**R**eflection **H**igh-**E**nergy **E**lectron **D**iffraction
SAED	**S**elected **A**rea **E**lectron **D**iffraction
SE	**S**pectroscopic **E**llipsometry
SEM	**S**canning **E**lectron **M**icroscopy
STM/S	**S**canning **T**unneling **M**icroscopy/**S**pectroscopy
TEM	**T**ransmission **E**lectron **M**icroscopy
TCO	**T**ransparent **C**onductive **O**xide
UHV	**U**ltra-**H**igh **V**acuum (p $< 10^{-9}$ mbar)
UPS	**U**ltra-violet **P**hotoelectron **S**pectroscopy
XPS	**X**–Ray **P**hotoelectron **S**pectroscopy
XRD	**X**–**R**ay **D**iffraction
VB(M)	**V**alence **B**and (**M**axiumum)
ϕ	work function
χ	electron affinity

Appendix B

List of publications

The following compilation consist of the papers published in refereed journals with contributions from my investigations of the surface properties of different materials. Since this thesis addresses the characterization of indium compounds, not all aspects of the performed studies could be discussed. The details about the works on other nitride surfaces (GaN and AlN) as well as the studies of the properties of organic films and ionic liquids can be directly extracted from the original manuscripts:

1. ***Investigations of MBE grown InN and the influence of sputtering on the surface composition***
   S. Krischok, V. Yanev, O. Balykov, M. Himmerlich, J. A. Schaefer, R. Kosiba, G. Ecke, I. Cimalla, V. Cimalla, O. Ambacher, H. Lu, W. J. Schaff, and L. F. Eastman
   Surf. Sci., 566-568 (2004), 849

2. ***The role of Si as surfactant and donor in molecular beam epitaxy of AlN***
   V. Lebedev, F. M. Morales, H. Romanus, S. Krischok, G. Ecke, V. Cimalla, M. Himmerlich, T. Stauden, D. Cengher, and O. Ambacher
   J. Appl. Phys., 98 (2005), 093508

3. ***Surface band bending at nominally undoped and Mg-doped InN by Auger Electron Spectroscopy***
   V. Cimalla, M. Niebelschütz, G. Ecke, V. Lebedev, O. Ambacher, M. Himmerlich, S. Krischok, J. A. Schaefer, H. Lu, and W. J. Schaff
   phys. stat. sol. (a), 203(1) (2006), 59

4. ***Nanocrystalline AlN:Si field emission arrays for vacuum electronics***
   V. Lebedev, F. M. Morales, M. Fischer, M. Himmerlich, S. Krischok, J. A. Schaefer, and O. Ambacher
   phys. stat. sol. (a), 203(7) (2006), 1839

5. ***Doping efficiency and segregation of Si in AlN grown by molecular beam epitaxy***
   V. Lebedev, F. M. Morales, H. Romanus, G. Ecke, V. Cimalla, M. Himmerlich, S. Krischok, J. A. Schaefer, and O. Ambacher
   phys. stat. sol. (c), 3(6) (2006), 1420

6. ***Tuning of surface properties of AlGaN/GaN sensors for nano- and pico-droplets***
C. Buchheim, G. Kittler, V. Cimalla, V. Lebedev, M. Fischer, S. Krischok, V. Yanev, M. Himmerlich, G. Ecke, J. A. Schaefer, and O. Ambacher
IEEE Sens. J., 6(4) (2006), 881

7. ***Electronic Structure of the Surface of the Ionic Liquid*** $[EMIM][Tf_2N]$ ***Studied by Metastable Impact Electron Spectroscopy (MIES), UPS, and XPS***
O. Höfft, S. Bahr, M. Himmerlich, S. Krischok, J. A. Schaefer, and V. Kempter
Langmuir, 22 (2006), 7120

8. ***Electronic properties of*** C_{60}***/InP(001) heterostructures***
G. Cherkashinin, S. Krischok, M. Himmerlich, O. Ambacher, and J. A. Schaefer
J. Phys.: Condens. Matter, 18 (2006), 9841

9. ***Impact of Device Technology Processes on the Surface Properties and Biocompatibility of Group III Nitride Based Sensors***
I. Cimalla, F.Will, K. Tonisch, M. Niebelschütz,V. Cimalla, V. Lebedev, G. Kittler, M. Himmerlich, S. Krischok, J. A. Schaefer, M. Gebinoga, A. Schober, T. Friedrich, and O. Ambacher
Materialwissenschaft und Werkstofftechnik, 37 (2006), 919

10. ***Effect of dislocations on electrical and electron transport properties of InN thin films. Part I. Strain relief and formation of a dislocation network***
V. Lebedev, V. Cimalla, J. Pezoldt, M. Himmerlich, S. Krischok, J. A. Schaefer, O. Ambacher, F. M. Morales, J. G. Lozano, and D. González
J. Appl. Phys., 100 (2006), 094902

11. ***A comparative study on the electronic structure of the 1-Ethyl-3-methylimidazolium bis(trifluoromethylsulfonyl)amide RT-ionic liquid by electron spectroscopy and first principles calculations***
S. Krischok, R. Öttking, W. J. D. Beenken, M. Himmerlich, P. Lorenz, O. Höfft, S. Bahr, V. Kempter, and J. A. Schaefer
Z. Phys. Chem., 220 (2006), 1407

12. ***Correlation between structural and electrical properties of InN thin films prepared by molecular beam epitaxy***
V. Lebedev, F. M. Morales, V. Cimalla, J. G. Lozano, D. González, M. Himmerlich, S. Krischok, J. A. Schaefer, and O. Ambacher
Superlattices Microstruct., 40 (2006), 289

13. ***Temperature dependent electronic and vibrational structure of the 1-Ethyl-3-methylimidazolium bis(trifluoromethylsulfonyl)amide room-temperature ionic liquid surface: a study with XPS, UPS, MIES and HREELS***
S. Krischok, M. Eremtchenko, M. Himmerlich, P. Lorenz, J. Uhlig, A. Neumann, R. Öttking, W. J. D. Beenken, O. Höfft, S. Bahr, V. Kempter, and J. A. Schaefer
J. Phys. Chem. B, 111 (2007), 4801

14. ***AlGaN/GaN biosensor - effect of device processing steps on the surface properties and biocompatibility***
    I. Cimalla, F. Will, K. Tonisch, M. Niebelschütz, V. Cimalla, V. Lebedev, G. Kittler, M. Himmerlich, S. Krischok, J. A. Schaefer, M. Gebinoga, A. Schober, T. Friedrich, and O. Ambacher
    Sens. Actuators B, 123 (2007), 740

15. ***Electronic properties of organic semiconductor blends: ambipolar mixtures of phthalocyanine and fullerene***
    A. Opitz, M. Bronner, W. Brütting, M. Himmerlich, J. A. Schaefer, and S. Krischok
    Appl. Phys. Lett., 90 (2007), 212112

16. ***Effect of surface oxidation on electron transport in InN thin films***
    V. Lebedev, V. Cimalla, Ch. Y. Wang, G. Ecke, S. Hauguth, M. Ali, M. Himmerlich, S. Krischok, J. A. Schaefer, and O. Ambacher
    J. Appl. Phys., 101 (2007), 123705

17. ***Morphology and Surface Electronic Structure of MBE grown InN***
    M. Himmerlich, S. Krischok, V. Lebedev, O. Ambacher, and J. A. Schaefer
    J. Cryst. Growth, 306 (2007), 6

18. ***Surface composition and electronic properties of indium tin oxide and oxynitride films***
    M. Himmerlich, S. Krischok, M. Koufaki, Ch. Mauder, G. Ecke, V. Cimalla, E. Aperathitis, and J. A. Schaefer
    Surf. Sci., 601 (2007), 4082

19. ***Electron transport properties of indium oxide - indium nitride metal-oxide-semiconductor heterostructures***
    V. Lebedev, Ch. Y. Wang, S. Hauguth, V. Polyakov, F. Schwierz, V. Cimalla, T. Kups, F. M. Morales J. G. Lozano, D. González, M. Himmerlich, J. A. Schaefer, S. Krischok, and O. Ambacher
    phys. stat. sol. (c), 5(2) (2008), 495

20. ***Effects of X-Ray Radiation on the Surface Chemical Composition of Thin Plasma Deposited Fluorocarbon Films***
    M. Himmerlich, V. Yanev, A. Opitz, A. Keppler, J. A. Schaefer, and S. Krischok
    Polym. Degrad. Stab., 93(3) (2008), 700

21. ***Electronic structure of GaN(0001)-2$\times$2 thin films grown by PAMBE***
    R. Gutt, P. Lorenz, K. Tonisch, M. Himmerlich, J. A. Schaefer, and S. Krischok
    phys. stat. sol. (RRL), 2(5) (2008), 212

Danksagung

Zum Gelingen dieser Arbeit haben viele Personen in unterschiedlichster Weise direkt oder indirekt beigetragen. Diesen soll an dieser Stelle mein Dank ausgesprochen sein.

Zuerst möchte ich Prof. Dr. Jürgen A. Schäfer und Priv.-Doz. Dr. Stefan Krischok danken. Sie haben mein Interesse an diesem interessanten Thema geweckt und haben die Arbeit mit ihren verschiedenen Sichtweisen immer gefördert. Stefan Krischok möchte ich darüber hinaus für die freundliche Betreuung der Arbeit danken. Die teilweise intensiven Diskussionen brachten neue Erkenntnisse und Anreize und haben die durchgeführten Untersuchungen in großem Maße befruchtet.

Bedanken möchte ich mich bei allen aktiven und ehemaligen Mitarbeitern der ZMN-TP I Gruppe. Mit der Hilfe von Annette Läffert, Vasil Yanev, Pierre Lorenz, Anja Eisenhardt, Richard Gutt und Angela Keppler hat es viel Spaß gemacht, die kleinen und großen Hürden im Labor und im Büro zu überwinden.

Einen großen Dank möchte ich weiterhin allen jetzigen und ehemaligen Projektpartnern des Instituts für Mikro- und Nanotechnologien aussprechen. Besonders hervorzuheben ist der rege Proben-, Daten und Informationsaustausch mit Dr. Vadim Lebedev, Chunyu Wang und Dr. Volker Cimalla. Interessante Diskussionen ermöglichten den Blickwinkel auf die durchgeführten Untersuchungen zu erweitern.

Außerdem danke ich allen weiteren Mitarbeitern des Fachgebietes Technische Physik I und des Zentrums für Mikro- und Nanotechnologien der TU Ilmenau für die angenehme Arbeitsatmosphäre. Die Gespräche mit Imad Ahmed, Thomas Stauden und Gerd Hartung haben bei wissenschaftlichen und technischen Fragestellungen unterstützend zur Lösungsfindung beigetragen. Für die Mithilfe bei den HREELS Messungen danke ich Katharina Klöckner. Die durch Pascal Schley, Katja Tonisch und Christof Mauder durchgeführten Ellipsometrie-, XRD- bzw. AES-Untersuchungen waren sehr aufschlussreich. Vielen Dank auch an Karin Schiller und Jana Spindler für die Hilfe bei allen verwaltungs- und informationstechnischen Problemen.

Für die Bereitstellung der ITO(N) Proben und eine ausgiebige Diskussion der Ergebnisse möchte ich M. Koufaki und E. Aperathitis auf Kreta meinen herzlichen Dank aussprechen. Gleiches gilt auch für die Diskussion der InN und In_2O_3 Daten sowie die zur Verfügungstellung von InN-Bandstrukturrechnungen durch Herrn F. Fuchs und Prof. F. Bechstedt von der Friedrich-Schiller-Universität Jena.

Zum Schluss möchte ich meiner Familie und allen Freunden für die vielfältige Unterstützung und nötige Ablenkung vom Alltagsgeschäft recht herzlich danken.

Erklärung

Ich versichere, dass ich die vorliegende Arbeit ohne unzulässige Hilfe Dritter und ohne Benutzung anderer als der angegebenen Hilfsmittel angefertigt habe. Die aus anderen Quellen direkt oder indirekt übernommenen Daten und Konzepte sind unter Angabe der Quelle gekennzeichnet. Weitere Personen waren an der inhaltlich-materiellen Erstellung der vorliegenden Arbeit nicht beteiligt. Insbesondere habe ich hierfür nicht die entgeltliche Hilfe von Vermittlungs- bzw. Beratungsdiensten (Promotionsberater oder anderer Personen) in Anspruch genommen. Niemand hat von mir unmittelbar oder mittelbar geldwerte Leistungen für Arbeiten erhalten, die im Zusammenhang mit dem Inhalte der vorgelegten Dissertation stehen. Die Arbeit wurde bisher weder im In- noch im Ausland in gleicher oder ähnlicher Form einer Prüfungsbehörde vorgelegt. Ich bin darauf hingewiesen worden, dass die Unrichtigkeit der vorstehenden Erklärung als Täuschungsversuch angesehen wird und den erfolglosen Abbruch des Promotionsverfahrens zu Folge hat.

Ilmenau, den 26. Juni 2008

Marcel Himmerlich